Universität Hamburg

Simulation of heavy Neutralinos at the International Linear Collider

Diplomarbeit,
vorgelegt von Oliver Wendt
aus Uetersen

Institut für Experimentalphysik
Universität Hamburg

Hamburg,
Februar 2005

Gutachter : Univ. Prof. Dr. R.-D. Heuer
Univ. Prof. Dr. P. Schleper

Abstract

A cut-based analysis of the associated production of a light and a heavy neutralino, $e^+e^- \to \tilde{\chi}_1^0\tilde{\chi}_3^0$, at the International Linear Collider (ILC) is presented. The analysis is performed on a set of simulated events, which consists of all relevant contributions from SM and SUSY processes to final states with up to six leptons. The basis of this study is the Minimal Supersymmetric Standard Model (MSSM) at the benchmark point SPS1a. Although the properties of the heavy neutralinos $\tilde{\chi}_3^0$, $\tilde{\chi}_4^0$ can be determined completely by measurements of the light system $\tilde{\chi}_1^0$, $\tilde{\chi}_2^0$, together with measurements of the charginos, a study of the heavy neutralino system provides a consistency check of the SUSY scenario. The ILC is an e^+e^- collider, which will provide polarised beams. In this thesis the following polarisations $\mathcal{P}_i := (P(e^+)/P(e^-))$, $(i = 1, 2, 3)$ are taken into account: $\mathcal{P}_1 = (0.0/0.0)$, $\mathcal{P}_2 = (0.0/0.8)$ and $\mathcal{P}_3 = (-0.6/0.8)$. The cut-based analysis is performed in the following two decay channels of the $\tilde{\chi}_3^0$, assuming an integrated luminosity of 500 fb^{-1} and a center-of-mass energy of 500 GeV: First $\tilde{\chi}_3^0 \to \tilde{\chi}_1^0 Z^0$, where $Z^0 \to e^\pm e^\mp, \mu^\pm\mu^\mp$. And second $\tilde{\chi}_3^0 \to \tilde{\chi}_2^0 Z^0$, where $\tilde{\chi}_2^0 \to \tilde{l}^\pm l^\mp$ and $Z^0 \to e^\pm e^\mp, \mu^\pm\mu^\mp$. For the first channel it is not possible to determine a significant contribution of the $\tilde{\chi}_3^0$ for any of the studied polarisations. The calculated statistical significances range from 0.26 to 1.22. In the second channel mentioned above, the determined significances range from 3.56 to 10.44 and the statistical errors on the partial cross-section range from 21% to 42%. For the polarisations $\mathcal{P}_2 = (0.0/0.8)$ and $\mathcal{P}_3 = (-0.6/0.8)$ a $5{\cdot}\sigma$-discovery is possible.

Zusammenfassung

In dieser Arbeit wird eine schnitt-basierte Analyse der assoziierten Produktion eines leichten Neutralinos und eines schweren $e^+e^- \to \tilde{\chi}_1^0\tilde{\chi}_3^0$ am International Linear Collider (ILC) vorgestellt. Die Analyse wird mit simulierten Ereignissen durchgeführt und beinhaltet alle relevanten Prozesse aus dem Standard Modell (SM) und aus supersymmetrischen Erweiterungen dessen, die bis zu sechs Leptonen im Endzustand aufweisen. Die Basis der Studie ist das minimale supersymmetrische Standardmodell (MSSM) am Parameterpunkt SPS1a. Obwohl die Eigenschaften der beiden schweren Neutralinos $\tilde{\chi}_3^0$, $\tilde{\chi}_4^0$ bereits durch Messungen des leichten Neutralinosysytems $\tilde{\chi}_1^0$, $\tilde{\chi}_2^0$, zusammen mit Messungen im Charginosektor, berechnet werden können, so ermöglicht die Untersuchung des schweren Neutralinosysytems doch eine Überprüfung der aus dem leichten Neutralinosysyem heraus gewonnenen Daten und damit eine Konsistenzüberprüfung des SUSY Modells. Der ILC ist ein e^+e^- Collider und bietet polarisierte Elektronen- und Positronenstrahlen. In dieser Arbeit werden die folgenden Polarisationen $\mathcal{P}_i := (P(e^+)/P(e^-))$, $(i = 1, 2, 3)$ verwendet: $\mathcal{P}_1 = (0.0/0.0)$, $\mathcal{P}_2 = (0.0/0.8)$ und $\mathcal{P}_3 = (-0.6/0.8)$. Die Analyse wird in den folgenden zwei Zerfallskanälen des $\tilde{\chi}_3^0$ für eine integrierte Luminosität von 500 fb^{-1} und eine Schwerpunktsenergie von 500 GeV durchgeführt: Zunächst für $\tilde{\chi}_3^0 \to \tilde{\chi}_1^0 Z^0$, wobei $Z^0 \to e^\pm e^\mp, \mu^\pm\mu^\mp$, and dann für $\tilde{\chi}_3^0 \to \tilde{\chi}_2^0 Z^0$, wobei $\tilde{\chi}_2^0 \to \tilde{l}^\pm l^\mp$ und $Z^0 \to e^\pm e^\mp, \mu^\pm\mu^\mp$. Im ersten Kanal ist es nicht möglich, einen signifikanten Beitrag vom Zerfall des $\tilde{\chi}_3^0$ in einer der Polarisationen zu finden. Die errechneten statistischen Signifikanzen liegen zwischen 0.26 und 1.22 für die verschiedenen Polarisationen. Im zweiten Kanal variieren die statistischen Signifikanzen zwischen 3.56 und 10.4 und die statistischen Fehler auf die berechneten partiellen Wirkungsquerschnitte liegen zwischen 21% und 42%. Für die Polarisationen $\mathcal{P}_2 = (0.0/0.8)$ und $\mathcal{P}_3 = (-0.6/0.8)$ ist hier eine $5{\cdot}\sigma$-Discovery möglich.

Contents

Chapter 1

Introduction

The Standard Model (SM) of particle physic is a very successful model in describing phenomena, observed during the last 50 years by high-energy physics experiments. It is confirmed in many modern high precision measurements. Moreover, it offers an enormous prediction power, as can be seen from the prediction of the heavy gauge boson Z^0, which was subsequently discovered at CERN with the experiment Gargamelle [1]. On the other hand, there are certain serious shortcomings of the SM. From a conceptual point of view, the "hierarchy problem" together with the "naturalness problem"are the most important shortcomings of the SM. They originate from the quadratic divergent one-loop corrections of the Higgs mass. In Supersymmetric extensions of the SM these problems are solved in a very elegant way by the introduction of bosonic Superpartners for each fermion and fermionic Superpartners for each boson of the SM. Supersymmetry (SUSY) offers more benefits, such as a neutral, weak interacting massive particle (WIMPS), which serves as a candidate for cold dark matter (CDM) and unification of all SM coupling constants at a scale $\Lambda_{GUT} \sim 1 \cdot 10^{16}$GeV. In this thesis a restricted SUSY model is assumed, which only includes the minimal necessary additional particle content. It is known as Minimal Supersymmetric Standard Model (MSSM). The parameter space of this model is divided into several benchmark points, of which the point SPS1a is used in this thesis. It is a typical "minimal super gravity" (mSUGRA) SUSY model. In a SUSY model with these requirements, the supersymmetric partners of the neutral W and B fields in the SM together with the neutral partners of the Higgs bosons mix to the so-called neutralinos $\tilde{\chi}_i^0$ $(i = 1, 2, 3, 4)$. In MSSM at SPS1a the $\tilde{\chi}_1^0$ with a mass of 97.1 GeV is the "lightest supersymmetric particle" (LSP). It is neutral and interacts only weakly and acts therefore as candidate, for CDM in this model. The focus of this thesis is the heavy neutralino system $\tilde{\chi}_3^0$ and $\tilde{\chi}_4^0$, with masses 365.2 GeV for the $\tilde{\chi}_3^0$ and 382.2 GeV for the $\tilde{\chi}_4^0$.

The International Linear Collider (ILC) will be the next electron-positron collider with an aimed center-of-mass energy of 500 GeV and an upgrade option to 1000 GeV. With this collider it will be possible to study signatures of supersymmetric events with very high precision, assuming SUSY is realised in Nature. Unfortunately, with a center-of-mass energy of 500 GeV it is not possible to produce the heavy neutralinos $\tilde{\chi}_3^0$ and $\tilde{\chi}_4^0$ via pair-production. The only possible process to study the properties of the heavy neutralino system is via an associated production with a light neutralino $\tilde{\chi}_1^0$ ($e^+e^- \to \tilde{\chi}_1^0\tilde{\chi}_3^0$ or $e^+e^- \to \tilde{\chi}_1^0\tilde{\chi}_4^0$). The goal of this thesis is, to perform a cut-based analysis of these channels on a set of simulated events, and to find out, if it is possible to detect these heavy neutralinos. The major problem of the analysis of such a production channel is the small cross-section of 7.2 fb for $e^+e^- \to \tilde{\chi}_1^0\tilde{\chi}_3^0$ and 0.9 fb for $e^+e^- \to \tilde{\chi}_1^0\tilde{\chi}_4^0$. Therefore, the suppression of background processes is a main

challenge in this analysis. Moreover, the ILC is able to provide polarised electron and positron beams. This is especially important for SUSY processes such as $e^+e^- \to \tilde{\chi}_1^0\tilde{\chi}_3^0$ and $e^+e^- \to \tilde{\chi}_1^0\tilde{\chi}_4^0$, because the production cross-section is enhanced significantly. Nevertheless, the cross-section of $e^+e^- \to \tilde{\chi}_1^0\tilde{\chi}_4^0$ stays small, and therefore this thesis will focus on the production channel $e^+e^- \to \tilde{\chi}_1^0\tilde{\chi}_3^0$. The $\tilde{\chi}_1^0$ is stable. For the analysis, the signatures of the two following decays of the $\tilde{\chi}_3^0$ are studied:

$$\tilde{\chi}_3^0 \to \tilde{\chi}_1^0 Z^0, \quad Z^0 \to e^\pm e^\mp, \mu^\pm \mu^\mp$$

and

$$\tilde{\chi}_3^0 \to \tilde{\chi}_2^0 Z^0, \quad \tilde{\chi}_2^0 \to \tilde{l}^\pm l^\mp, \quad Z^0 \to e^\pm e^\mp, \mu^\pm \mu^\mp.$$

For the analysis a set of simulated events is used, which consists of all relevant contributions from SM and SUSY processes to final states with up to six leptons. The simulation of the detector is done in a parametrised way with the simulation tool SIMDET4.

After this brief introduction, a description of the theoretical context is given. It starts with an overview of the Standard Model (SM), describes the Higgs mechanism and gives some details about Supersymmetry (SUSY). Here, after the SUSY Lagrangian is built up step by step, more emphasis is set on the Minimal Supersymmetric Standard Model (MSSM), which is the basis of this thesis. Moreover, the neutralino system is described more precisely. The third chapter includes a more detailed description of the International Linear Collider, which will be the next main high energy experiment after the Large Hadron Collider (LHC). Here, next to the description of the machine itself, some conceptional aspects are described, which arises from the theoretical needs of measuring supersymmetric signatures and which directly influence the design of the accelerator and the detector. This is mainly the "Particle Flow Concept", which ensures the reconstruction of every particle individually within the detector. The fourth chapter describes the used simulation tools, gives more information of the two decays of the $\tilde{\chi}_3^0$ studied and describes the simulation of the set of simulated events. The fifth chapter includes the detailed description of the cut-based analysis and presents the results of the selection. Finally, the thesis concludes with a brief summary and an outlook.

Chapter 2

Theoretical Context

This Chapter gives a brief introduction to the basics of modern particle physics. First the Standard Model (SM) is described, which is an extremely successful model based on quantum field theories and the gauge principle. The so-called Higgs mechanism, included in the SM, "generates" the mass of the particles via the interaction with an omnipresent, global Higgs field. After this, a more detailed description of one of today's most popular extensions of the SM, known as Supersymmetry (SUSY), is given. SUSY provides answers to many of the open questions of the SM and is theoretically as well as phenomenologically interesting (see Section 2.1.2). For a more detailed description of the SM see [2, 3], for details on the Higgs mechanism [4] and for SUSY [5, 6, 7, 8, 9]. In all equations mentioned in this chapter the "Einstein summation convention" is used, i.e. summation over identical co- and contra-variant indices is done without writing them explicitly.

2.1 The Standard Model

The Standard Model (SM) is a mathematical description of elementary particles and fields as well as their interactions. It consists of two quantum field theories and is based on the principle of local gauge invariance (see Tab. 2.1). A local gauge transformation in this sense means, that the transformation itself might differ from point to point in space and time; so, more strictly speaking, it may be a function of space and time. This principle is very successful. For example the postulation of invariance of the Lagrangian under local gauge transformations has led to the prediction of a heavy neutral vector boson Z, which was later discovered at CERN with the neutrino bubble chamber experiment Gargamelle [1]. Except gravity, three of the four known interactions are covered by the SM. These are the weak interaction, which for example is responsible for the beta decay, the electro-magnetic interaction, with phenomena such as light or bound states in atoms, and the strong interaction, which is the reason for bound states of quarks in protons or even the nuclear force as a "van-der-Waals like" residual force. Gravity is suppressed by a factor of $\sim 10^{-38}$ compared to the strong interaction. Therefore, for the description of the microscopic world it is irrelevant, that gravity is not covered by the SM. On the other hand, this is a serious problem on the way to the unification of all interactions and so, to a "theory of everything" (TOE). Besides this more aesthetic aspect, there are conditions, where the strength of gravity becomes comparable to the other forces and so an unified description of all four interactions is necessary. This is the case for physics at the Planck Scale:

$$\Lambda_P = M_P = \sqrt{\frac{\hbar c}{\mathrm{G_N}}} \sim 1 \cdot 10^{19}\mathrm{GeV}, \tag{2.1}$$

where G_N is Newton's constant [10]. Many of these TOEs, including quantised gravity, require a new symmetry, that combines bosonic and fermionic states, Supersymmetry fulfills this role (see Section 2.1.2 and 2.2). In the following, a short introduction to the two gauge theories of the SM, Quantum Flavour Dynamics (QFD) and Quantum Chromo Dynamics (QCD), is given. All particles of the SM are listed in Tables 2.2 and 2.3.

	field theory		acts on
weak interactions		Quantum Flavour Dynamics (QFD)	"weak charge"
electro-mag. interactions	Quantum Electro Dynamics (QED)		electric charge
strong interactions	Quantum Chromo Dynamics (QCD)		color charge

Table 2.1: *Quantum Field Theories in the Standard Model*

Quantum Flavour Dynamics (QFD):

Quantum Flavour Dynamics (QFD) describes the electro-weak sector of the SM. This is the unification of weak and electro-magnetic interactions to a new gauge theory with a $SU(2)_L \times U(1)_Y$ gauge group. It is also known as electro-weak unification. A gauge theory based on a group $SU(2)_L \times U(1)_Y$ means, that a SU(2) gauge transformation, acting on the weak isospin I of left-handed SU(2)-doublets is combined with a U(1) gauge theory acting on the hypercharge Y. The connection between (weak) isospin and hypercharge is given by the following relation, where Q_e is the electric charge:

$$Y := 2 \cdot (Q_e - I_3). \tag{2.2}$$

In the following the principles of electro-weak interactions are discussed, using the first generations of leptons as an example (see Tab. 2.2). All other generations can be described in the same way. The quantum fields, which are associated with particles, appear as the left-handed doublet

$$L = \begin{pmatrix} \nu_e \\ e \end{pmatrix}_L \tag{2.3}$$

and the right-handed singlet

$$R = e_R. \tag{2.4}$$

The left- and right-handed representations are gained by applying the projection operator $P_{L/R}$ on the wave functions:

$$L = P_L \Psi, \quad R = P_R \Psi, \quad \Psi = L + R, \tag{2.5}$$

with

$$P_{L/R} := \frac{1}{2}(1 \mp \gamma^5). \tag{2.6}$$

To establish a gauge invariant quantum field theory one has to ensure, that all observables stay the same when applying a gauge transformation. That means the Lagrangian should stay the same, except of the total derivative of a quantity K^μ, which itself may be a function of the fields in the Lagrangian and their derivatives[1]:

$$\mathcal{L} \to \mathcal{L}' = \mathcal{L} + \partial_\mu K^\mu. \tag{2.7}$$

[1]The principle of least action $\delta S = \delta \int \mathcal{L} \mathrm{d}^4x \stackrel{!}{=} 0$ leads to equations of motion, which are not affected by the field K^μ.

	Family					
	1	2	3	Q_{el}	$I_{W,3}$	Y
leptons	$\begin{pmatrix}\nu_e\\ e\end{pmatrix}_L$	$\begin{pmatrix}\nu_\mu\\ \mu\end{pmatrix}_L$	$\begin{pmatrix}\nu_\tau\\ \tau\end{pmatrix}_L$	$\begin{pmatrix}0\\ -1\end{pmatrix}$	$\begin{pmatrix}1/2\\ -1/2\end{pmatrix}$	$\begin{pmatrix}-1\\ -1\end{pmatrix}$
	e_R	μ_R	τ_R	-1	0	-2
quarks	$\begin{pmatrix}u\\ d'\end{pmatrix}_L$	$\begin{pmatrix}c\\ s'\end{pmatrix}_L$	$\begin{pmatrix}t\\ b'\end{pmatrix}_L$	$\begin{pmatrix}2/3\\ -1/3\end{pmatrix}$	$\begin{pmatrix}1/2\\ -1/2\end{pmatrix}$	$\begin{pmatrix}1/3\\ 1/3\end{pmatrix}$
	u_R	c_R	t_R	2/3	0	4/3
	d'_R	s'_R	b'_R	-1/3	0	-2/3

Table 2.2: *Fermion multiplets of the SM. The primes of the down-type quarks indicate that their electro-weak interaction eigenstates d' , s', b' are not equal to their mass eigenstates d, s, b (see Sec. 2.1). The quark mixing is described by the Cabibbo-Kobayashi-Maskawa (CKM) matrix (see Eq. (2.26)). The indices L(R) denote left(right)-handed fermions and the electric charge Q_{el} is given in multiples of the elementary charge e. The symbol $I_{W,3}$ specifies the third component of the weak isospin I and Y describes the hypercharge (see Eq. (2.2))*

A local gauge transformation with operators of the group $\mathrm{SU}(2)_L \times \mathrm{U}(1)_Y$ can be written as

$$L \to L' = e^{ig\alpha^a \frac{\sigma_a}{2}} L, \quad R \to R' = R \tag{2.8}$$

for a $\mathrm{SU}(2)_L$ transformation and

$$L \to L' = e^{ig'\beta\frac{Y}{2}} L, \quad R \to R' = e^{ig'\beta\frac{Y}{2}} R. \tag{2.9}$$

for a $\mathrm{U}(1)_Y$ transformation. σ_a and β are generators of the groups $\mathrm{SU}(2)_L$ and $\mathrm{U}(1)_Y$ respectively, and the σ_a are given by the Pauli-matrices. The functions α^a $(a = 1, 2, 3)$ and β are functions of space and time, hence these gauge transformations are called *local*. The strength of the interaction, which is later associated with this gauge transformation, is given by the couplings g and g'.

The most simple Lagrangian only consists of kinetic terms of the Dirac fields L and R:

$$\mathcal{L} = i\overline{L}\gamma^\mu \partial_\mu L + i\overline{R}\gamma^\mu \partial_\mu R, \tag{2.10}$$

which leads from the principle of least action $\delta S \stackrel{!}{=} 0$ to an equation of motion (Dirac's equation)

$$i\gamma^\mu \partial_\mu \Psi = 0 \tag{2.11}$$

for a massless Dirac field without interactions. The Lagrangian (2.10) is not locally gauge invariant, since a simple $\mathrm{U}(1)_Y$ transformation (2.9) results in

$$\mathcal{L} \to \mathcal{L}' = \mathcal{L} + g'(\overline{L}\gamma^\mu L + \overline{R}\gamma^\mu R)\partial_\mu \beta \neq \mathcal{L}. \tag{2.12}$$

To compensate the additional terms, which destroy the gauge invariance, and to achieve $\mathcal{L} \to \mathcal{L}' = \mathcal{L}$ the three gauge fields W^a_μ $(a = 1, 2, 3)$ for the $\mathrm{SU}(2)_L$ and B_μ the $\mathrm{U}(1)_Y$ transformation are introduced. This is done in analogy to QED, where gauge invariance with respect to a local phase transformation requires the introduction of a photon field A_μ. Hence, the derivative ∂_μ is expanded to the covariant derivative

$$\partial_\mu \to D_\mu = i\left(\partial_\mu + ig\frac{\sigma_a}{2}W^a_\mu + ig'\frac{Y}{2}B_\mu\right). \tag{2.13}$$

interaction	exchange boson	spin	mass
electro-magnetic	γ	1	0
weak	Z^0	1	91.2 GeV
	$W^{\pm}$	1	80.4 GeV
strong	8 gluons (g)	1	0
	Higgs	0	> 114.4 GeV (95% CL)

Table 2.3: *Overview of the mass eigenstates of the SM bosons. Their properties are given in terms of their spin and their mass. The only particle of the SM, which is not yet discovered is the Higgs boson [11]. Its mass is a free parameter of the theory (see Sec. 2.1.1).*

and the transformation behavior of the gauge fields W^a_μ and B_μ is given by

$$W^a_\mu \to W^{a\prime}_\mu = W^a_\mu - \frac{1}{g}\partial_\mu \alpha^a - \varepsilon^a_{bc}\alpha^b W^c_\mu, \tag{2.14}$$

$$B_\mu \to B'_\mu = B_\mu + \frac{1}{g'}\partial_\mu \beta. \tag{2.15}$$

With the definition of the field strength tensors $W^a_{\mu\nu}$ and $B_{\mu\nu}$ for the fields W^a_μ and B_μ

$$W^a_{\mu\nu} := \partial_\mu W^a_\nu - \partial_\nu W^a_\mu - g\varepsilon^a_{bc} W^b_\mu W^c_\nu \tag{2.16}$$

$$B_{\mu\nu} := \partial_\mu B_\nu - \partial_\nu B_\mu \tag{2.17}$$

one finally obtains the QFD Lagrangian

$$\mathcal{L}_{\mathrm{QFD}} = -\frac{1}{4}W^a_{\mu\nu}W^{\mu\nu}_a - \frac{1}{4}B_{\mu\nu}B^{\mu\nu} + i\overline{L}\gamma^\mu D_\mu L + i\overline{R}\gamma^\mu D_\mu R. \tag{2.18}$$

W^3_μ and B_μ carry identical quantum numbers; in particular, they are electrically neutral.

Until now, we have only considered gauge fields, which couple to the neutrino (see Eq. (2.3). This has been experimentally disproved since the neutrino is neutral and, therefore the photon field does not couple to it. This means, the fields W^a_μ and B_μ cannot be identified with the physical fields. This problem is solved by a rotation in the space of the two neutral gauge fields W^3_μ and B_μ by an angle called the electro-weak mixing angle[2] θ_W:

$$\begin{pmatrix} \mathrm{Z}_\mu \\ \mathrm{A}_\mu \end{pmatrix} = \begin{pmatrix} \cos\theta_W & \sin\theta_W \\ -\sin\theta_W & \cos\theta_W \end{pmatrix} \begin{pmatrix} \mathrm{W}^3_\mu \\ \mathrm{B}_\mu \end{pmatrix}, \qquad \cos\theta_W = \frac{g}{\sqrt{g^2+g'^2}}, \tag{2.19}$$

$$\mathrm{W}^+_\mu = \mathrm{W}^1_\mu + i\mathrm{W}^2_\mu, \tag{2.20}$$

$$\mathrm{W}^-_\mu = \mathrm{W}^1_\mu - i\mathrm{W}^2_\mu, \tag{2.21}$$

and hence discloses the composition for the fields A_μ and Z^0_μ:

$$A_\mu = \frac{1}{\sqrt{g^2+g'^2}}(g'W^3_\mu + gB_\mu), \tag{2.22}$$

$$\mathrm{Z}^0_\mu = \frac{1}{\sqrt{g^2+g'^2}}(gW^3_\mu - g'B_\mu). \tag{2.23}$$

[2] Also known as the Weinberg angle.

Another fundamental relation is the connection between the Weinberg angle θ_W, the coupling constants g as well as g' and the elementary charge e

$$e = g' \cos\theta_{\mathrm{W}} = g \sin\theta_{\mathrm{W}}. \tag{2.24}$$

The Lagrangian (2.18), together with the rotation (2.19) to (2.23), leads to the observed physics. It describes the couplings correctly, the self-interactions of the gauge bosons, as well as the kinetic terms of the gauge fields. Next to the success of this closed theory, there is a serious problem: Terms of the form $m_f \overline{\Psi}_L \Psi_R$ and $M^2 \, \mathrm{W}_\mu^a W_a^\mu$ violate the gauge invariance. This means the description of mass in this canonical way[3] is not possible within the QFT, and moreover it is not possible in the SM at all. Therefore, QFD, as it is described above, only contains massless particles, which does not reflect the Nature correctly. The Higgs mechanism, as an extension of the SM, solves this problem by introducing a background field. This is described in Sec. 2.1.1.

Quantum Chromo Dynamics (QCD):

The second, main gauge theory of the SM is Quantum Chromo Dynamics (QCD), which describes the strong interactions (see Table 2.1). It acts on all quarks (see Table 2.2) as the carrier of the strong charge named color. Through the invention of the static quark model [12, 13, 14] one was able to order all observed mesons and baryons into multiplets of so-called quark flavour, assuming that mesons are built of two and baryons of three quarks. For some baryons the predicted total wave function was symmetric, whereas the measured spin was $\frac{1}{2}\hbar$. Moreover, there are baryons such as the Δ^{++}, which consist of three up-quarks in the same state. This seemed to violate Pauli's principle, which is truly fundamental. To preserve it, a new multiplicative part of the wave function, named color wave function, was introduced. This led to a new quantum number color with three states, usually called red, green and blue. The corresponding gauge theory is invariant under rotations in this three dimensional color space. Now one can follow the same way of argumentation as in the case of QFD above. The Lagrangian should be locally gauge invariant under $\mathrm{SU}(3)_c$ transformations:

$$\Psi \rightarrow \Psi' = e^{i g_s \epsilon_i^a \frac{\lambda_a^i}{2}} \Psi. \tag{2.25}$$

The eight λ_a^i are the generators of the group $\mathrm{SU}(3)_c$, i denotes the color-index ($i = 1, 2, \ldots 8$), the ϵ_i^a are functions of space and time and represent the local gauging and g_s is the strong coupling constant. To achieve local gauge invariance one has to introduce eight new gauge fields into the Lagrangian of QCD. This leads to eight exchange bosons named gluons (see Table 2.3).

These two quantum field theories are the main constituents of the SM. Indeed, one important aspect has to be considered. Quarks also take part in weak interactions, and the interaction eigenstates of the down-type quarks d', s', b' (see Table 2.2) in weak interactions are not the same as the mass eigenstates d, s, b. The two representations are connected by the Cabibbo-Kobayashi-Maskawa-Matrix V_{CKM}:

$$\begin{pmatrix} d' \\ s' \\ b' \end{pmatrix} = V_{CKM} \begin{pmatrix} d \\ s \\ b \end{pmatrix} = \begin{pmatrix} V_{ud} & V_{us} & V_{ub} \\ V_{cd} & V_{cs} & V_{cb} \\ V_{td} & V_{ts} & V_{tb} \end{pmatrix} \begin{pmatrix} d \\ s \\ b \end{pmatrix} \tag{2.26}$$

[3] Terms of this kind are similar to mass terms in Dirac's and Klein-Gordon's equation. Therefore, they are titled canonic.

So, the SM consists of the combined $\mathrm{SU(3)}_c \times \mathrm{SU(2)}_L \times \mathrm{U(1)}_Y$ gauge group and its prediction power is enormous. It describes the photon, the charged and the neutral currents with the correct couplings to the fermions. All the couplings have been measured with great precision, and all predictions of the SM are in agreement with these precision measurements. Also all particles of the first three generations of quarks and leptons and all vector bosons have been experimentally discovered. Unfortunately, the SM implies no mass terms. In the model, as it is introduced above, all fermions and all gauge bosons are massless. This is due to the fact that mass terms for the fermions $m_f\,\overline{\Psi}_L\Psi_R$ and the gauge bosons $M^2\,\mathrm{W}^a_\mu W^\mu_a$ are not invariant under $\mathrm{SU(3)}_c \times \mathrm{SU(2)}_L \times \mathrm{U(1)}_Y$ transformations. This means, an adoption of massive particles in such a canonic way would destroy the gauge invariance. On the other hand, we know from experiment, that besides the photon and the gluon all particles of the SM are massive. Therefore, a mechanism has been proposed, which dynamically generates the particle masses, without violating the powerful gauge principle[4]. This mechanism is known as the Higgs Mechanism and is described in the next Section.

2.1.1 The Standard Model Higgs Mechanism

Mass terms of the form $m_f\,\overline{\Psi}_L\Psi_R$ and $M^2\,\mathrm{W}^a_\mu W^\mu_a$ are not gauge invariant within $\mathrm{SU(2)}_L \times \mathrm{U(1)}_Y$ transformations. To solve this problem, mass terms are introduced dynamically. This is done by a background field Φ, known as the Higgs field [15], with a non-zero vacuum expectation value (v.e.v.)[5]. The particle associated with this field is the so-called Higgs boson (see Tab. 2.3). The masses then are described as an interaction of the particles with the Higgs field, when they are traveling through space. For the dynamical generation of mass we have to distinguish between the massive gauge bosons $W^\pm_\mu$ and Z^0_μ on the one hand, and the fermions (see Tab. 2.2) on the other. For the massive gauge bosons one generates mass terms from the kinetic terms $(D_\mu\Phi)^\dagger(D^\mu\Phi)$ of the field Φ, for the fermions Yukawa-like terms $\lambda_\mathrm{f}(\overline{L}\Phi R + \overline{R}\Phi^\dagger L)$ are introduced. Moreover, considering the gauge bosons, we have to ensure that the photon field A_μ stays massless to describe Nature correctly. All of this is done by the following definition of Φ as a complex SU(2) doublet with scalar complex fields ϕ^+ and ϕ^0 and the principle of spontaneous symmetry breaking[6]:

$$\Phi = \begin{pmatrix} \phi^+ \\ \phi^0 \end{pmatrix}. \tag{2.27}$$

To ensure gauge invariance under $\mathrm{SU(2)}_L \times \mathrm{U(1)}_Y$ and a non-vanishing v.e.v. the following potential is chosen $V(\Phi^\dagger\Phi)$:

$$V(\Phi^\dagger\Phi) = \frac{\mu^2}{2}\Phi^\dagger\Phi + \frac{\lambda}{4}(\Phi^\dagger\Phi)^2, \tag{2.28}$$

with $\lambda > 0$ and $\mu^2 < 0$. The Lagrangian then simply is constructed of a kinetic and a potential term

$$\mathcal{L}_\mathrm{Higgs} = (D_\mu\Phi)^\dagger(D^\mu\Phi) - V(\Phi^\dagger\Phi), \tag{2.29}$$

where D_μ is the covariant derivative of the QFD (see Eq. (2.13)). The potential $V(\Phi^\dagger\Phi)$ is shown in Figure 2.1. The minima of the potential lead to ground states following the relation

$$2 \cdot |\Phi_0|^2 = -\frac{\mu^2}{\lambda} =: v^2, \tag{2.30}$$

[4] At least for the corresponding Lagrangians (see Sec. 2.1.1).

[5] A non-zero vacuum expectation value results in a field, which is present in the whole space.

[6] Spontaneous symmetry breaking means, that a system, which obeys a certain symmetry, here $\mathrm{SU(2)}_L \times \mathrm{U(1)}_Y$ symmetry, does not show it in its ground state anymore.

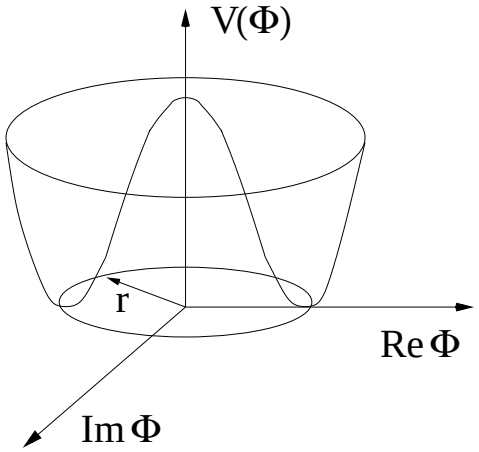

Figure 2.1: *Potential of the Higgs field in the case of a single scalar complex field, where r indicates the radius for the possible minima.*

where v is the v.e.v. of the neutral component of the Higgs field ϕ^0 (see Eq. (2.27)). When the system takes one of the minimum configurations, the $\mathrm{SU}(2)_L \times \mathrm{U}(1)_Y$ symmetry is no longer preserved. This is the spontaneous symmetry breaking, where the $\mathrm{SU}(2)_L \times \mathrm{U}(1)_Y$ symmetry is broken to a $\mathrm{U}(1)_{em}$ symmetry[7]. The Lagrangian (2.29) indeed is still gauge invariant under $\mathrm{SU}(2)_L \times \mathrm{U}(1)_Y$ and all properties connected to that, such as current conservation, are still preserved. The $\mathrm{U}(1)_{em}$ symmetry is the gauge symmetry of QED, which is not identical to $\mathrm{U}(1)_Y$ and should be preserved, to obtain a massless photon[8]. The component ϕ^+ is set to zero, because otherwise a massive photon would occur. Now one can write down the Higgs field for the ground state by taking (2.27), setting ϕ^+ to zero and putting in (2.30)

$$\Phi = \frac{1}{\sqrt{2}} \begin{pmatrix} 0 \\ v \end{pmatrix}. \tag{2.31}$$

The Higgs boson (see Tab. 2.3) appears by expanding the field Φ around its minimum. Now one can use the Higgs field (2.31) and insert it in the Lagrangian (2.29). Together with the Higgs potential (2.28) this leads to mass terms for the gauge bosons (from the $(D_\mu\Phi)^\dagger(D^\mu\Phi)$ term):

$$\frac{g^2v^2}{4} W_\mu^a W_a^\mu, \quad \frac{(g^2+g'^2)v^2}{4} \mathrm{Z}_\mu \mathrm{Z}^\mu, \tag{2.32}$$

with the corresponding predicted masses

$$M_\mathrm{A} = 0, \quad M_{\mathrm{W}^\pm} = \frac{gv}{2}, \quad M_\mathrm{Z} = \frac{\sqrt{g^2+g'^2}v}{2}, \tag{2.33}$$

$$\Rightarrow \cos(\theta_\mathrm{W}) = \frac{g}{\sqrt{g^2+g'^2}} = \frac{M_{\mathrm{W}^\pm}}{M_\mathrm{Z}}. \tag{2.34}$$

There are also terms proportional to $-\lambda v^2 h^2$, which lead to the mass of the Higgs boson itself, via self-interaction.

[7] This is also known as Electro-weak Symmetry Breaking.
[8] This is known as the Goldstone mechanism (see e.g. [2]).

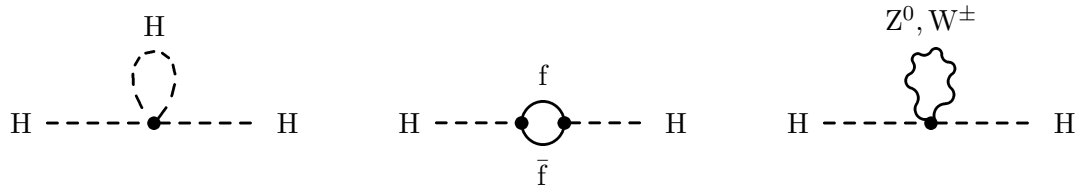

Figure 2.2: *One-loop contributions to the Higgs boson mass arising from (a) Higgs boson loop, (b) fermion loop, (c) gauge boson loop. These quadratic divergencies are not canceled in the SM and lead to unnatural large radiative corrections to the Higgs mass.*

The generation of mass of the fermions is achieved by adding Yukawa-like terms to the Lagrangian. These terms are Lorentz and gauge invariant, as well as renormalisable, and therefore could (and should) be inserted into the Lagrangian. They have the following form:

$$\lambda_{\mathrm{f}}(\overline{L}\Phi R + \overline{R}\Phi^{\dagger}L), \tag{2.35}$$

where the coupling λ_{f} is adjusted proportional to the fermion mass. In this sense they are free parameters of the model, which is a shortcoming of this model (see Sec. 2.1.2 as well).

The SM including the Higgs Mechanism offers a consistent description of the observed phenomena. The Higgs Boson is the only particle of this model which has not been observed yet[9]. Despite all the success of the SM, there are serious fundamental shortcomings, which suggest that the SM is only a low-energy approximation of a more comprehensive model. The most important shortcomings of the SM are mentioned in the next section.

2.1.2 Shortcomings of the Standard Model

Both from the experimental and the theoretical point of view, there are shortcomings of the SM. The most important are mentioned below:

- Unfortunately, the SM suffers from quadratic divergencies to the Higgs mass. The radiative one-loop corrections of the Higgs mass, as shown in Figure 2.2, are all quadratically divergent within the SM [7]. Therefore, it is reasonable to consider the SM as a low-energetic approximation of a more fundamental model. Natural choices for an energy scale, at which the prediction power of the SM ends, are the Planck scale $\Lambda_P \sim 1 \cdot 10^{19}$GeV (see Sec. 2.1) or the GUT scale $\Lambda_{GUT} \sim 1 \cdot 10^{16}$GeV. This means for the Higgs, that the natural scale of the Higgs boson mass is Λ_P, while all other particles have natural mass scales below v. This is the so-called "hierarchy problem", which refers to the extremely large splitting of the weak scale and the natural cut-off scale, e.g. the Planck scale. It cannot be explained within the SM. Moreover, an upper limit on the Higgs mass is given by the preservation of unitarity in WW scattering [5]:

  $$\delta M_H \leq 1\mathrm{TeV}. \tag{2.36}$$

  This requires an extreme "fine-tuning" of the SM parameters to achieve $\frac{M_H}{\Lambda_P} \sim 10^{-16}$. These two aspects are, from a conceptual point of view, the most important shortcomings of the SM. An estimate of the mass correction is given by

  $$\delta M_H^2 \sim \mathcal{O}\left(\frac{\lambda^2}{16\pi^2}\right) \cdot \Lambda^2, \tag{2.37}$$

[9] Mass bounds can be found in Tab. 2.3 and in [11].

where λ describes the fermion/boson trilinear coupling to the scalar Higgs field and Λ is the assumed scale, at which the SM breaks down and new physics appears. For the sake of completeness it should be said that it is possible to get rid of all divergencies by renormalisation. This has to been done very carefully in any order of perturbation theory, because of the needed precision $\frac{M_H}{\Lambda_P} \sim 10^{-16}$ mentioned above, and is therefore quite "unnatural". In Supersymmetric extensions of the SM (see Sec. 2.2) this problem is solved in a very elegant way by the introduction of bosonic Superpartners for each fermion and fermionic Superpartners for each boson, with otherwise same quantum numbers. Whilst sharing the same quantum numbers, but following opposite spin statistics, they contribute to the radiative corrections for each particle with the same value, but with opposite sign and hence suppress the radiative corrections on the Higgs mass. In this sense Supersymmetry connects the fermionic and the bosonic degrees of freedom[10].

- There is a large observed matter/antimatter asymmetry in our universe. Within the SM the only mechanism, which leads to such a asymmetry, is CP-violation. It is describes by the CKM mechanism, but it does not explain the large measured matter/antimatter asymmetry [11]. Therefore, additional sources of CP-violation are needed. Supersymmetric extensions of the SM offer such sources.

- The only candidates for dark matter (DM) within the SM are neutrinos. Their number is known to a high degree of accuracy due the primordial nuclei-synthesis. Moreover, mass limits can be obtained experimentally [11]. This leads to an estimate on the contribution of neutrinos to DM. It is much to small to explain the measured data [16]. Therefore, an enclosing extension to the SM should provide weakly interacting massive particles (WIMPs), which serve as candidates for dark matter[11]. These are included within SUSY models.

- More aesthetic theories, which include the SM, should unify all interactions. Therefore, all coupling constants of the interactions in the SM should reach the same value at a certain energy scale (GUT scale, $M_{GUT} \sim 1 \cdot 10^{16}$GeV). This is not possible within the SM, whereas supersymmetric extensions of the SM allow this unification in some regions of their parameter space (see Fig. 2.3) [11].

- In the SM, it is not possible to include gravity as a quantum field theory, because it is not renormisable. String theories are popular candidates to include gravity in a quantised field theory. Most String theories are supersymmetric on the particle or Poincaré level.

2.2 Basic Ideas of Supersymmetry and the MSSM

As mentioned in Sec. 2.1.2, a connection of fermions and bosons solves the finetuning problem by eliminating the quadratic divergencies on the radiative corrections of the Higgs mass. Including further assumptions, this can also be used to solve the hierarchy problem. The generator Q of this new symmetry translates a bosonic state $|\phi\rangle$ into a fermionic one $|\psi\rangle$ and

[10] Actually, these corrections cancel completely, if $m_{\text{particle}} = m_{\text{super-partner}}$, similar to QED, where the radiative corrections on the photon mass are zero in any order of perturbation theory. This leads directly to the exact U(1) gauge symmetry of QED. Therefore, a finite Higgs mass is a strong hint for an additional symmetry, keeping the corrections on the Higgs mass under control [7].

[11] The neutrino contribution to the DM is often called hot dark matter (HDM), whereas the contribution of the WIMPs is named cold dark matter (CDM).

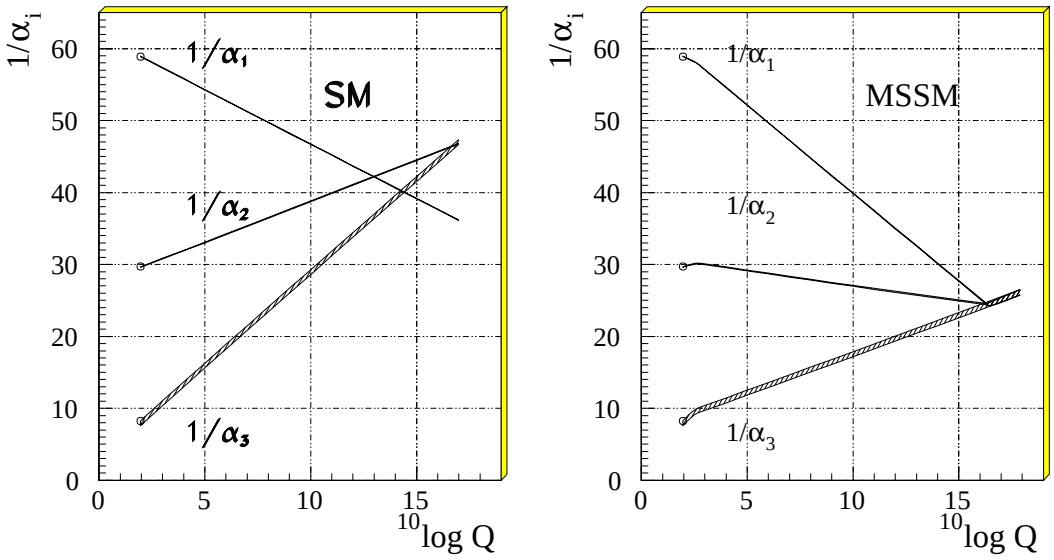

Figure 2.3: *Evolution of the gauge couplings α_i due to radiative corrections as a function of energy Q. The parameters α_i are defined as $\alpha_i = g_i^2/4\pi$ $(i = 1, 2, 3)$, where $i = 1$ represents the coupling "constant" of the $U(1)_Y$ group, $i = 2$ denotes the coupling "constant" of the $SU(2)_L$ group, and $i = 3$ is used for QCD. The theoretical uncertainties in QCD are denoted by the error-band of the function $1/\alpha_3$. It is not possible to unify the three coupling constants α_1, α_2 and α_3 at any scale in the SM, whereas in supersymmetric extensions, in particular in the Minimal Supersymmetric Standard Model (MSSM), this is feasible (see Sec. 2.1.2 and 2.4).*

vice versa. Symbolically this leads to the following equation:

$$Q\,|\psi\rangle = |\phi\rangle, \qquad Q\,|\phi\rangle = |\psi\rangle. \tag{2.38}$$

In this transformation, the spin of the state is changed by a value of $\frac{1}{2}\hbar$ and therefore Q carries itself half integer spin, i.e. it is a fermionic operator. From another point of view, one could say that the hierarchy problem is solved by the introduction of a new, fermionic dimension. In order to emphasize the contrast to the gauge generators mentioned in Sec. 2.1, which are all bosonic, this new symmetry is called Supersymmetry (SUSY). In this study, the minimal extension of the SM, the so-called Minimal Supersymmetric Standard Model (MSSM), is used. In this simple choice only one fermionic generator Q is needed[12]. In the most popular representation the generators Q_α act on two-component spinors[13], which satisfy the following (anti)commutation relations:

$$\{Q_\alpha, Q_\beta\} = \{\bar{Q}_\alpha, \bar{Q}_\beta\} = 0, \quad [Q_\alpha, P^\mu][\bar{Q}_\alpha, P^\mu] = 0, \quad \{Q_\alpha, \bar{Q}_\beta\} = -2\sigma^\mu_{\alpha\beta} P_\mu, \tag{2.39}$$

where $\bar{Q}$ represents the adjoint operator to Q and P_μ is the translation generator, i.e. the momentum operator. The indices $\alpha,\ \beta = 1, 2$ are the indices of the two-dimensional representation of the Poincaré group[14] and $\sigma^\mu_{\alpha\beta}$ is given by the Pauli matrices, $\sigma^\mu = (1, \vec{\sigma})$ and follows the relation:

$$\sigma^\mu_{\alpha\beta} = \begin{cases} \sigma^\mu & \text{for } \alpha = \beta \\ 0 & \text{for } \alpha \neq \beta \end{cases} . \tag{2.40}$$

[12]The definition of Q is not unambiguous. It is possible to use several operators Q^i $(i = 1, 2, \ldots \mathrm{N})$ at the same time. The number of independent operators of a theory is usually denoted by N.

[13]These two-component spinors are named Weyl spinors.

[14]Q_α exists in either $(0, \frac{1}{2})$ or $(\frac{1}{2}, 0)$ representation of the Lorentz group [17].

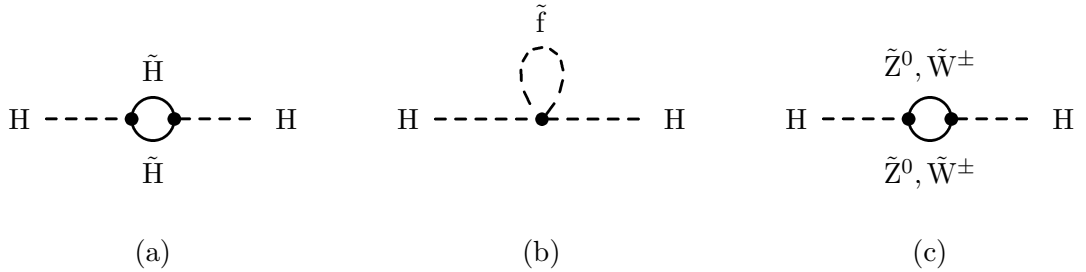

Figure 2.4: *SUSY contributions to the Higgs boson mass. The quadratic divergencies to the Higgs mass introduced by the graphs in Fig. 2.2 are suppressed by (a) Higgsino, (b) sfermion, (c) Wino and Zino contributions.*

It is also possible to use more generators to introduce a SUSY model, but this would lead to non-minimal extension of the SM and is not described here (see e.g. [18, 19]).

The MSSM contains the minimal number of new supersymmetric particles and interactions, where the particles are classified in so-called Supermultiplets. Each of these multiplets consists of a SM particle and its SUSY partner, and therefore of a fermion and a boson, as well as an additional auxiliary vectorfield[15]. All particles of a Supermultiplet have the same quantum numbers of the gauge group, i.e. charge, weak isospin, color, and mass[16]. Here a really serious problem arises. Since, except the Higgs boson, all particles of the SM have been discovered, there should be evidence for the SUSY particles because of their equal quantum numbers and mass. So far, no SUSY particle has been observed. Therefore, SUSY cannot be realised in Nature as an exact symmetry. It must be broken. In order to conserve the proportion of the scales, SUSY breaking is introduced as a soft (symmetry) breaking [7]. For more details, see Sec. 2.4. In broken SUSY, particles of the multiplets do not have the same mass; therefore, the corrections on the Higgs mass are not canceled completely. But at least the quadratic divergencies are eliminated by additional loop contributions of the SUSY particles (see Fig. 2.4).

The corrections to the Higgs mass within a broken SUSY fulfill

$$\delta M_H^2 \sim \mathcal{O}\left(\frac{\lambda^2}{16\pi^2}\right) \cdot |M_b^2 - M_f^2|, \tag{2.41}$$

where $\lambda = \lambda_f = \lambda_b$ is the universal fermion and boson coupling to the scalar field and M_f and M_b are masses of fermion and boson fields, respectively. The cancellation of quadratic divergencies keep the radiative corrections on the masses of scalar fields in the order of the electro-weak scale, provided that:

$$\delta M_H^2 \sim |M_b^2 - M_f^2| \lesssim 1\mathrm{TeV}^2. \tag{2.42}$$

In a N = 1 SUSY the SM particle content can be described by using only two classes of supermultiplets (see Table 2.4). In the chiral multiplet[17] Ψ describes the usual fermionic fields in the SM and Φ its scalar superpartner, i.e. for each lepton and quark there is such a multiplet. To conserve all ("two") degrees of freedom of the fermionic field Ψ, Φ is introduced as a complex scalar field. With this, for each left and right handed fermion of the SM a superpartner is assigned, which is named scalar quark or scalar lepton ("squark" or "slepton"). The second super multiplet contains the SM spin 1 vector bosons and their spin-$\frac{1}{2}$ superpartners.

[15] It does not affect the equations of motion.
[16] mass, generated by the Higgs mechanism
[17] also known as matter or scalar multiplet

	multiplet	spin	
chiral multiplet	$\begin{pmatrix}\Phi\\ \Psi\end{pmatrix}$	$\begin{pmatrix}0\\ \frac{1}{2}\end{pmatrix}$	complex scalar field fermionic field (Weyl fermion)
gauge multiplet	$\begin{pmatrix}A^\mu\\ \lambda\end{pmatrix}$	$\begin{pmatrix}1\\ \frac{1}{2}\end{pmatrix}$	vector field (gauge boson) fermionic field (Weyl fermion)

Table 2.4: Supermultiplets of the MSSM

Therefore, it is named gauge multiplet. These super partners of the SM gauge bosons are named Gluinos, Winos and Binos according to their SM partners; they form the Zino and Photino as counterpart of the Z^0 and γ. In Table 2.5 all particles of the MSSM are listed, where j is the family or generation index. Notice that in contrast to the SM, there are two Higgs doublets. This is necessary to ensure that the superpotential stays analytical and that triangular anomalies cancel out [20].

In the following, the Lagrangian of the MSSM, first for a chiral and second for a gauge multiplet, is constructed. For a more detailed overview see [5], as well as [6, 7, 8, 9]. The most simple Lagrangian of a chiral multiplet is given by

$$\mathcal{L}_{chir} = -\partial^\mu \Phi^* \partial_\mu \Phi - i\Psi^\dagger \bar{\sigma}^\mu \partial_\mu \Psi \tag{2.43}$$

A SUSY transformation changes a boson into a fermion and vice versa. The most elementary possibility for the transformation of a scalar field Φ is

$$\delta\Phi = e\Psi \quad \delta\Phi^* = e^\dagger \Psi^\dagger, \tag{2.44}$$

where e^a $(a = 1, 2)$ is an infinitesimal, anti-commutating, two-component Weyl fermion object, which parameterises the transformation. To ensure that the Lagrangian stays invariant under this transformation, the fields Ψ_α transform like

$$\delta\Psi_\alpha = i(\sigma^\mu \partial_\mu)_\alpha \Phi e^\dagger \quad \delta\Psi^\dagger_\alpha = -i(\sigma^\mu \partial_\mu)_\alpha \Phi^* e. \tag{2.45}$$

This is the so-called Wess-Zumino model, which describes a non-interacting, massless, chiral super multiplet. To close the SUSY algebra (2.39) one has to introduce an auxiliary field F, a complex spin 0 field coupling to the other fields. F does not have its own dynamics and is only connected to the other fields in an algebraic way. Its Lagrangian can be written as

$$\mathcal{L}_{aux} = F^* F. \tag{2.46}$$

The combined Lagrangian expands to

$$\mathcal{L}_{chir} = -\partial^\mu \Phi^* \partial_\mu \Phi - i\Psi^\dagger \bar{\sigma}^\mu \partial_\mu \Psi + F^* F, \tag{2.47}$$

together with the SUSY transformations

$$\begin{aligned} &\delta\Phi = e\Psi, && \delta\Phi^* = e^\dagger \Psi^\dagger, \\ &\delta\Psi_\alpha = i(\sigma^\mu \partial_\mu)_\alpha \Phi e^\dagger + e_\alpha F, && \delta\Psi^\dagger_\alpha = -i(\sigma^\mu \partial_\mu)_\alpha \Phi^* e + e^\dagger_\alpha F^*, \\ &\delta F = ie^\dagger \bar{\sigma}^\mu \partial_\mu \Psi, && \delta F^* = i\partial_\mu \Psi^\dagger \bar{\sigma}^\mu e. \end{aligned} \tag{2.48}$$

The last equation shows, that the auxiliary field just transform into a total derivative. Therefore, it does not have an effect on the "equations of motion", coming from $\delta S = \delta \int \mathcal{L} \mathrm{d}^4x \overset{!}{=} 0$ (see Sec. 2.1). Now one can insert terms, which describe the interactions. They are arranged in a

superfield	boson field	fermion field
gauge multiplets		
G	g	$\tilde{g}$
$W^{1,2}$	$W^{1,2}$	$\tilde{W}^{1,2}$
W^0	W^0	$\tilde{W}^0$
B^0	B^0	$\tilde{B}^0$
chiral multiplets		
$\begin{pmatrix} L_j \\ E_j \end{pmatrix}$	leptons $\left\{ \begin{pmatrix} (\tilde{\nu}_j, \tilde{e}_j^-)_L \\ \tilde{e}_{j,R}^- \end{pmatrix} \right.$	$\begin{pmatrix} (\nu_j, \mathrm{e}_j^-)_L \\ \mathrm{e}_{j,R}^- \end{pmatrix}$
$\begin{pmatrix} Q_j \\ U_j \\ D_j \end{pmatrix}$	quarks $\left\{ \begin{pmatrix} (\tilde{u}_j, \tilde{d}_j)_L \\ \tilde{u}_{j,R} \\ \tilde{d}_{j,R} \end{pmatrix} \right.$	$\begin{pmatrix} (u_j, d_j)_L \\ u_{j,R} \\ d_{j,R} \end{pmatrix}$
$\begin{pmatrix} H_d \\ H_u \end{pmatrix}$	Higgs $\left\{ \begin{pmatrix} (H_d^0, H_d^-) \\ (H_u^+, H_u^0) \end{pmatrix} \right.$	$\begin{pmatrix} (\tilde{H}_d^0, \tilde{H}_d^-) \\ (\tilde{H}_u^+, \tilde{H}_u^0) \end{pmatrix}$

Table 2.5: *The MSSM particle spectrum. Shown are the electro-weak eigenstates. The gauge bosons $W^{1,2}$ combine to the mass eigenstates $W^{\pm}$ and the W^0 and B^0 mix in electro-weak symmetry breaking to Z^0 and γ (see Sec.2.1). Analogously the winos $\tilde{W}^{\pm}$are built and the $\tilde{W}^0$ and binos $\tilde{B}^0$ mix to the zinos $\tilde{\mathrm{Z}}^0$ and photinos $\tilde{\gamma}$. The mass eigenstates of the latter are the charginos and neutralinos (see Sec. 2.5).*

way, that one has Yukawa like couplings between the scalar and fermionic fields, mass terms, but no new fermionic interactions. The most general form of such a Lagrangian is given below

$$\mathcal{L}_{int} = -\frac{1}{2} W^{ij} \Psi_i \Psi_j + W^i F_i + \text{c.c.} \tag{2.49}$$

where "c.c." means complex conjugated and W^{ij} as well as W^i are so-called Superpotentials, which are functions of the boson fields and invariant under SUSY transformations (2.48). Moreover, they only contain bi- and trilinear terms of the scalar fields:

$$W = \frac{1}{2} M^{ij} \Phi_i \Phi_j + \frac{1}{6} y^{ijk} \Phi_i \Phi_j \Phi_k, \tag{2.50}$$

$$W^i = \frac{\partial}{\partial \Phi_i} W = \frac{1}{2} M^{ij} \Phi_j + \frac{1}{6} y^{ijk} \Phi_j \Phi_k, \tag{2.51}$$

$$W^{ij} = \frac{\partial^2}{\partial \Phi_i \partial \Phi_j} W = \frac{1}{2} M^{ij} + \frac{1}{6} y^{ijk} \Phi_k, \tag{2.52}$$

where M^{ij} is a symmetric mass matrix of the fermion fields and y^{ijk} describes the the Yukawa coupling between two fermion fields and one scalar. The first term of (2.49) then can be written as:

$$-\frac{1}{2} W^{ij} \Psi_i \Psi_j = -\frac{1}{4} M^{ij} \Psi_i \Psi_j - \frac{1}{12} y^{ijk} \Phi_k \Psi_i \Psi_j. \tag{2.53}$$

The second term of (2.49) includes only terms proportional to the auxiliary field F. This leads together with the Superpotentials (see Eq. (2.50) to (2.52)) to the following expression:

$$W^i F_i = \frac{1}{2} M^{ij} \Phi_j F_i + \frac{1}{6} y^{ijk} \Phi_j \Phi_k F_i. \tag{2.54}$$

The auxiliary field F_i can be eliminated, because the terms $F_i F^{i*} + W^i F_i + W_i^* F^{i*}$ of the Lagrangian, where $F_i F^{i*}$ is part of $\mathcal{L}_{chir}$ (see Eq. (2.47) and $W^i F_i + W_i^* F^{i*}$ derives from (2.49), result via $\delta S \stackrel{!}{=} 0$ in the equations of motion shown below:

$$F_i = -W_i^*, \quad F^{i*} = -W^i. \tag{2.55}$$

If this is inserted in Eq. (2.54), the auxiliary field F is canceled out:

$$W^i W_i^* = \frac{1}{2} M^{ij} \Phi_j W_i^* + \frac{1}{6} y^{ijk} \Phi_j \Phi_k W_i^*. \tag{2.56}$$

Since $W^i W_i^*$ is a scalar one can write the second term of Eq. (2.49) as a scalar Potential $V(\Phi, \Phi^*)$ by using Eq. (2.50) to (2.52))

$$\begin{aligned} V(\Phi, \Phi^*) &:= W^i W_i^* \\ &= M_{ij}^2 \Phi^{i*} \Phi_j + \tfrac{1}{4} y^{ijn} y^*_{kln} \Phi_i \Phi_j \Phi^{k*} \Phi^{l*} \\ &\quad + \tfrac{1}{2} M^{in} y^*_{jkn} \Phi_i \Phi^{j*} \Phi^{k*} \\ &\quad + \tfrac{1}{2} M^{in*} y^{jkn} \Phi^{i*} \Phi_j \Phi_k. \end{aligned} \tag{2.57}$$

The scalar Potential $V(\Phi, \Phi^*)$ contains mass terms with the same mass matrix for the scalars Φ_i as for the fermions Ψ_i (see Eq. (2.53)) as well as interactions of three and four scalars[18] (see Eq. (2.57)). Moreover, the Superpotential describes the scalar and the Yukawa coupling. For a given potential y^{ijk} we obtain couplings of the same strength for particles and sparticles; in the case of the MSSM this is the reason for the canceling of the quadratic divergencies (see Fig. 2.4).

The Lagrangian of the gauge multiplet on the other hand describes the vector bosons and the fermionic gauginos and can be written as

$$\mathcal{L}_{gauge} = -\frac{1}{4} F^a_{\mu\nu} F^{\mu\nu a} - i \lambda^{\dagger a} \bar{\sigma}^\mu D_\mu \lambda^a + \frac{1}{2} D^a D^a, \tag{2.58}$$

where $F^a_{\mu\nu}$ is the usual kinetic term of the gauge fields:

$$F^a_{\mu\nu} = \partial_\mu A^a_\nu - \partial_\nu A^a_\mu - g f^{abc} A^b_\mu A^c_\nu. \tag{2.59}$$

The second term of (2.58) contains the kinetic energy of the gauginos as well as their interactions with the gauge fields due to the covariant derivative

$$D_\mu \lambda^a = \partial_\mu \lambda^a - g f^{abc} A^b_\mu \lambda^c. \tag{2.60}$$

The third term of (2.58) represents again the Lagrangian of an auxiliary field D^a, which is needed to preserve the SUSY algebra (2.39). It transforms as in the case of the fermionic field λ^a and achieves $D^{a*} = D^a$.

Finally, the Lagrangians of the chiral and of the gauge multiplet can be put together in order to design a general Lagrangian for a SUSY theory. To obtain a gauge invariant

[18] cubic and bi-quadratic couplings

Lagrangian the derivatives in the Lagrangian of the chiral doublets need to be replaced by the covariant derivatives:

$$\partial_\mu \Phi \to D_\mu \Phi = \partial_\mu \Phi + igA^a_\mu T^a \Phi, \tag{2.61}$$

$$\partial_\mu \Psi \to D_\mu \Psi = \partial_\mu \Psi + igA^a_\mu T^a \Psi, \tag{2.62}$$

where T^a symbolize the generators of gauge group[19]. The "standard matter" Lagrangian is obtained by combining the vector and chiral fields in a gauge invariant manner, including the covariant derivatives and adding terms of the form:

$$-\sqrt{2}g((\Phi^* T^a \Psi)\lambda^a + \lambda^{a\dagger}(\Psi^\dagger T^a \Phi)), \tag{2.63}$$

$$g(\Phi^* T^a \Phi) D^a. \tag{2.64}$$

The coupling constants g is given by the standard coupling constant of the gauge group. Eq. (2.64) only depends of scalar fields. Therefore, it is inserted together with the term $\frac{1}{2}D^a D^a$ of (2.58) into the scalar potential $V(\Phi, \Phi^*)$ (see Eq. (2.57)):

$$V(\Phi, \Phi^*) = \underbrace{W^{i*} W^i}_{\text{(a)}} + \underbrace{\frac{1}{2} g^2 (\Phi^* T \Phi)^2}_{\text{(b)}}, \tag{2.65}$$

where (a) arises from the F-terms of the chiral Lagrangian and (b) contains the D-terms of the gauge multiplet.

Putting all the pieces together result in a general SUSY-Lagrangian of the form:

$$\begin{aligned} \mathcal{L}_{\text{SUSY}} = \quad & \underbrace{-i\bar{\Psi}\bar{\sigma}^\mu D_\mu \Psi}_{(a)} - \underbrace{D^\mu \Phi^* D_\mu \Phi}_{(b)} - \underbrace{\frac{1}{4} F^a_{\mu\nu} F^{\mu\nu a}}_{(c)} - \underbrace{i\lambda^{\dagger a} \bar{\sigma}^\mu D_\mu \lambda^a}_{(d)} - \\ & \underbrace{\frac{1}{2} W^i W^*_i + \frac{1}{2} g_a^2 (\Phi^* T^a \Phi)^2}_{(e)} - \underbrace{\frac{1}{2}(W^{ij} \Psi_i \Psi_j + W^{ij*} \Psi^{i\dagger} \Psi^{j\dagger})}_{(f)} - \\ & \underbrace{\sqrt{2} g((\Phi^* T^a \Psi)\lambda^a + \lambda^{a\dagger}(\Psi^\dagger T^a \Phi))}_{(g)} + \underbrace{\mathcal{L}_{soft}}_{(h)}. \end{aligned} \tag{2.66}$$

Below the parts of the Lagrangian $\mathcal{L}_{\text{SUSY}}$ are described briefly:

(a) Kinetic term of the fermion fields. It contains the kinetic energy and gauge interactions of the fermion fields as a result of the covariant derivative $D_\mu \Psi = \partial_\mu \Psi + igA^a_\mu T^a \Psi$ (see Eq. (2.62)).

(b) As in (a), but for the scalar fields Φ. Due to $D_\mu \Phi = \partial_\mu \Phi + igA^a_\mu T^a \Phi$ (see Eq. (2.61)) interactions of the scalar fields to the gauge bosons are included.

(c) Kinetic energy and self-interaction of the gauge fields. Field strength tensor is given by Eq. (2.59). This leads to strong and electro-weak vertices as in the SM.

[19] Suppose that the chiral super multiplets transform under the gauge group in a representation with hermitian matrices T^a satisfying $[T^a, T^b] = if^{abc}T^c$, so e.g. if the gauge group is SU(2), then $f^{abc} = \epsilon^{abc}$ and the T^a are $\frac{1}{2}$-times the Pauli matrices for a chiral super multiplet transforming in the fundamental representation

(d) Kinetic term of the gaugino fields. It contains the gaugino gauge boson couplings. Due to the fact that they are fermions, this term has the same form as in (a). For the covariant derivative (2.60) has to be chosen. Among others, this part of the Lagrangian describes the coupling between the Z^0-boson and neutralinos $\tilde{\chi}_1^0\tilde{\chi}_3^0$ in the s-channel, which governs the cross-section for the process studied in this thesis (see Fig. 2.9 (a)).

(e) Scalar potential $V(\Phi, \Phi^*)$ (see Eq. (2.65)). It contains mass terms for all scalars and all scalar interactions. The scalar potential is completely defined by the other interactions[20]. The F-term is given by the Yukawa coupling and the mass terms of the fermions, the D-term is defined by the gauge interactions.

(f) Yukawa couplings and mass terms of the fermions in the superpotential W^{ij}.

(g) Additional gauge invariant SUSY couplings. This part of the Lagrangian characterises the coupling between a gaugino, a scalar and a fermion, for example as it appears in the t-channel of the associated production of $\tilde{\chi}_1^0$ and $\tilde{\chi}_3^0$ (see Fig. 2.9 (b)).

(h) Further term of the Lagrangian, which is responsible for the SUSY breaking. As already mentioned, no super-particles have been observed, although, according to the simple SUSY model described here, they should have the same mass as their super-partner. Therefore, SUSY should be broken to ensure a high mass of the super-particles outside the energy range of today's accelerators[21]. This term is described in more detail in Sec. 2.4.

2.3 R-Parity and the Superpotential of the MSSM

In a minimal supersymmetric extension of the SM, it is reasonable to choose a Superpotential with the smallest number of possible couplings, as long as all observed phenomena are described correctly. Hence, the general form of the Superpotential W (see Eq. (2.50)) turns into:

$$W_{MSSM} = y_u\bar{U}QH_u - y_d\bar{D}QH_d - y_e\bar{E}LH_d + \mu H_uH_d. \tag{2.67}$$

The objects L, E, Q, U, D, H_d and H_u are chiral superfields corresponding to the chiral multiplets in Table 2.5 and y_u, y_d and y_e are the Yukawa coupling constants. Family indices are not mentioned in Eq. (2.67), hence y_u, y_d and y_e are 3×3 matrices, which characterise the masses and the CKM mixing angle of the leptons and quarks[22]. The so-called "μ-term" in Eq. (2.67) is the supersymmetric version of Higgs boson mass in the SM. In the MSSM the Yukawa coupling is, except for the third family, assumed to be quite small. In most cases the production and decay of SUSY particles is dominated by couplings to gauge bosons and gaugino couplings to scalars and fermions (see Sec. 2.5). Gluinos, winos and binos only couple to particles, to which their superpartners are coupling as well. That means, gluinos only couple to quarks and squarks, Winos only to left-handed quarks, squarks, leptons, sleptons and Higgs and the Binos to all particles which carry hypercharge.

[20] as the Higgs mechanism in the SM

[21] The LHC and the ILC are the first machines, which will be able to push forward to the supposed energy regime of these kind of SUSY particles. So, if SUSY is realised in Nature, these two machines will be able to "see" at least parts of the SUSY particle spectrum. For more information on the ILC see Chapter 3. Theoretically, Tevatron should be able to measure supersymmetric signatures, but they suffer from backgrounds and low luminosity [21, 22].

[22] Before doing so, the Higgs bosons need to be expanded around their vacuum expectation values.

The MSSM Superpotential was introduced in Eq. (2.67). A more general, gauge invariant and renormisable Superpotential would also include baryon and lepton number violating terms. Especially, the decay of the proton would be possible[23]. These violating terms can be written as

$$W_{\Delta L=1} = \frac{1}{2}\lambda^{ijk} L_i L_j \bar{E}_k + \lambda'^{ijk} L_i Q_j \bar{D}_k + \mu'^{i} L_i H_u \text{and} \tag{2.68}$$

$$W_{\Delta B=1} = \frac{1}{2}\lambda''^{ijk} \bar{U}_i \bar{D}_j \bar{D}_k. \tag{2.69}$$

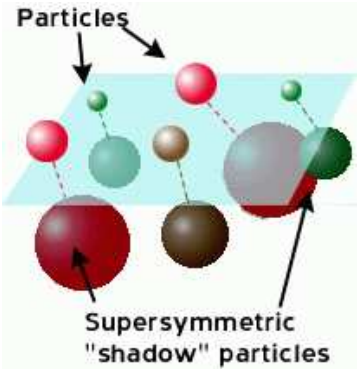

Figure 2.5: *Illustration of the heavy counterparts of the SM particles*

For a proton decay the u- and d-quarks of the proton transform into $\tilde{\text{b}}$ or $\tilde{\text{s}}$ squarks via the term $\frac{1}{2}\lambda''^{ijk}\bar{U}_i\bar{D}_j\bar{D}_k$. They then decay because of $\lambda'^{ijk}L_iQ_j\bar{D}_k$ into a lepton and a quark. In Nature baryon or lepton number violation never has been observed. Therefore, one introduces a additional symmetry called R-parity[24], which prohibits terms like (2.68) and (2.69). R-parity is a multiplicative quantum number and is defined by

$$P_R := (-1)^{3(B-L)+2S}, \tag{2.70}$$

where B is the baryon, L is the lepton number and S is the spin. All SM particles and the Higgs bosons have a R-parity of 1, all sparticles, i.e. squarks, sleptons, gauginos and higgsinos, have a R-parity of -1 (see Tab. 2.7). The consequences of the invariance under this new symmetry or, in other words, of the conservation of R-parity are listed below:

- There is no mixing between particles with $P_R = 1$ and particles with $P_R = -1$. Therefore, SUSY particles can only be produced in pairs, at each vertex an even number of sparticles occurs and heavy SUSY particles decay into lighter ones.
- The lightest sparticle must be stable, because a decay $\tilde{B}(P_R{=}-1) \rightarrow A(P_R{=}1){+}B(P_R{=}1)$ violates R-parity conservation. This particle is called "lightest supersymmetric particle" (LSP). If it is interacting only weakly, it would be a good candidate for cold dark matter (CDM).
- Each sparticle, except of the lightest one, decays into an odd number of LSPs.
- A typical signature of an event, where SUSY particles are involved, would show a large amount of missing energy (Due to the LSPs, which cannot be detected. In the model, which is used in this thesis the LSP is the $\tilde{\chi}_1^0$ (see Sec. 2.5).).

[23] From experiment, the lower limit on the proton life time is given by $\tau_p > 10^{32}$ years [11].
[24] also known as matter parity

The channels, which are studied in this thesis, are of the kind mentioned in the last aspect of the list (see Sec. 2.5 and Fig. 2.10). The missing energy is carried away by the neutralinos $\tilde{\chi}_1^0$, which interact only weakly and, hence, are difficult to detect.

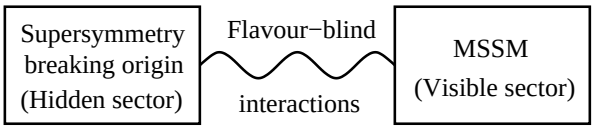

Figure 2.6: *The mediation of SUSY breaking from the hidden sector. Unspecified physics at the GUT scale in a so-called hidden sector leads to SUSY breaking. This breaking is then transferred to the visible sector via a messenger field, which can be a known field like gravity or new physics.*

2.4 SUSY Breaking

Due to the fact that no SUSY particles have been observed yet, SUSY must be broken. The symmetry breaking can be obtained in a similar way as the electro-weak sector in the SM. Therefore, the masses of the sparticles are much higher than their SM counterparts and cannot be detected in today's experiments. This is illustrated in Fig 2.5. Additionally one has to ensure, that the suppression of the loop contributions to the Higgs mass is sustained, no other quadratic divergencies appear (see Sec. 2.1.1 and Fig. 2.2 as well as Fig. 2.4) and the theory stays renormisable. Hence, a soft SUSY breaking term $\mathcal{L}_{soft}$ is introduced in the Lagrangian (2.66). In the MSSM it is parametrised in the following form:

$$\begin{aligned}\mathcal{L}_{soft} = \; & \tfrac{1}{2}(M_3\tilde{g}\tilde{g} + M_2\tilde{W}\tilde{W} + M_1\tilde{B}\tilde{B} + \text{c.c.}) + \\ & \tfrac{1}{6}(a_u\tilde{U}QH_u - a_d\tilde{D}QH_d - a_e\tilde{E}LH_d) - \\ & m_Q^2 Q^\dagger Q - m_L^2 L^\dagger L - m_U^2 \bar{U}\bar{U}^\dagger - m_D^2 \bar{D}\bar{D}^\dagger - m_E^2 \bar{E}\bar{E}^\dagger - \\ & m_{H_u}^2 H_u^* H_u - m_{H_d}^2 H_d^* H_d - (bH_uH_d + \text{c.c.})\end{aligned} \tag{2.71}$$

Again the objects L, E, Q, U, D, H_d and H_u are chiral superfields corresponding to the chiral multiplets in Table 2.5 and the $\tilde{g}$, $\tilde{W}$, $\tilde{B}$ denote the gauge multiplets, "c.c." means complex conjugated. The M_i $(i = 1, 2, 3)$ are the gluino, wino and bino mass terms, the a_j $(j = u, d, e)$ are complex 3×3 matrices in family space, and the m_k $(k = Q, L, U, D, e)$ as well as the m_l $(l = H_u, H_d)$ are hermitian 3×3 matrices in family space. Due to the symmetry breaking 105 new parameters are introduced. Therefore, an unrestricted MSSM depends on $105 + 19$ masses, phases, and mixing angles[25]. The number of parameters can be reduced furthermore by including experimental results from CP violation measurements. Notice, that the fields given here, do not correspond to the mass eigenstates. The mass eigenstates can be obtained by an additional transformation (see Sec. 2.5 for the neutralino case). Additionally we can assume, that the squark- and the slepton mass matrices m_l $(l = Q, U, D, L, E)$ are "flavour-blind", i.e. the mass matrices only have diagonal entries, and they have the same value. Moreover, it is assumed that the matrices a_j $(j = u, d, e)$ are proportional to the corresponding Yukawa matrices. With this restrictions the number of free parameters is reduced to 14. In

[25] 19 is the number of free parameters in the SM.

this configuration, the model is able to describe the unification of the three coupling constants at a scale of $\Lambda_{GUT} \sim 1 \cdot 10^{16}$GeV, as it is shown in Fig. 2.3. As already mentioned, the SUSY breaking terms are supposed to be "flavour-blind". This suggests, that the reason for the SUSY breaking originates from a so-called "hidden sector" at high scales (see Fig. 2.6). That means SUSY breaking takes place in the hidden sector and the particles in this sector only have a very small coupling to the particles in the visible sector. If this would not be the case, we would observe the breaking of some "low scale" symmetries, SUSY particles with masses smaller than SM particles and additional particle content of the SM [5]. The visible sector contains all the SM particles and their superpartners and there is only a flavour-blind coupling between these sectors, which is responsible for the symmetry breaking. At the moment, there are two popular models with different candidates form the messenger fields. First the gauge mediated SUSY breaking (GMSB), where the SUSY breaking terms are caused by electroweak and strong gauge interactions. And second a gravity mediated SUSY breaking model, also known as "minimal super gravity" (mSUGRA), which is used as basis in this thesis. In mSUGRA, it is assumed that the SUSY breaking terms are transmitted by gravity.

parameter	description	SPS1a
m_0	scalar mass at mass unification scale Λ_{GUT}	100 GeV
$m_{\frac{1}{2}}$	gaugino mass at mass unification scale Λ_{GUT}	250 GeV
m_A	mass of the CP-odd Higgs boson	-100 GeV
$\tan\beta$	ratio of the vacuum expectation values of the Higgs bosons H_u and H_d, ($\tan\beta := \frac{<H_u>}{<H_d>}$)	10
sign(μ)	sign of the Higgs mass parameter (see Eq. (2.67))	$\mu > 0$

Table 2.6: *Set of parameters used in the mSUGRA MSSM and the values of these parameters at the benchmark point SPS1a, which is used in this study. To vary the parameter $m_{\frac{1}{2}}$ around the benchmark point, there are also slopes for the other parameters defined [23].*

Usually the number of additional free parameters is reduced to five by further assumptions, like mass and gauge unification at Λ_{GUT} scale. These parameters are listed in Tab. 2.6. To cover the five-dimensional parameter space of the mSUGRA MSSM, it has been divided into several, feasible benchmark points [23], which are compatible with cosmological measurements [24, 25][26]. In this thesis the scenario SPS1a is used, which is a typical mSUGRA point with an intermediate value of $\tan\beta$ (see Tab. 2.6 and Sec. 2.5). In this environment, the lightest neutralino $\tilde{\chi}_1^0$ is the LSP and acts as the candidate for CDM (see Sec. 2.5).

2.5 Heavy Neutralinos and Investigated Channels

Due to SUSY breaking, the interaction and the mass eigenstates are no longer identical. Therefore, the neutral winos and binos, $\tilde{W}^0$ and $\tilde{B}^0$, together with the neutral Higgsinos $\tilde{H}_d^0$, $\tilde{H}_u^0$ (see Tab. 2.5) mix to the so-called neutralinos $\tilde{\chi}_i^0$ ($i = 1, 2, 3, 4$). The four neutralinos are the mass eigenstates of $(\tilde{W}^0, \tilde{B}^0, \tilde{H}_d^0, \tilde{H}_u^0)$ according to their mass matrices derived from the full Lagrangian (see Eq. 2.66 together with Eq. 2.71). The full mass matrix in the basis of the

[26] Including the latest measurements leads to the modified benchmark point SPS1a′. However, the particle spectrum is not changed.

super fields (see Tab. 2.5) is given by:

$$M_{\tilde{\chi}^0} = \begin{pmatrix} M_1 & 0 & -M_Z c_\beta s_W & M_Z s_\beta s_W \\ 0 & M_2 & M_Z c_\beta c_W & -M_Z s_\beta c_W \\ -M_Z c_\beta s_W & M_Z c_\beta c_W & 0 & -\mu \\ M_Z s_\beta s_W & -M_Z s_\beta c_W & -\mu & 0 \end{pmatrix}, \tag{2.72}$$

where the following conventions are used: $c_\beta := \cos\beta$, $s_\beta := \sin\beta$, $c_W := \cos\theta_W$, $s_W := \sin\theta_W$; θ_W symbolises the electro-weak mixing angle. The parameters M_1 and M_2 denote the mass terms of the bino and wino in $\mathcal{L}_{soft}$ (see Eq. 2.71) and μ is the Higgsino mass term. The terms proportional to M_Z describe the Higgs-Higgsino-gaugino coupling and $\tan\beta$ is the ratio of the two v.e.v of the two Higgs fields. The matrix $M_{\tilde{\chi}^0}$ can be diagonalised by applying a unitary transformation, so that all elements on the diagonal are positive real numbers. These are the physical masses of the neutralinos $\tilde{\chi}_i^0$ $(i = 1, 2, 3, 4)$. The charged Higgsinos and winos, $(\tilde{H}_d^-, \tilde{H}_u^+)$ and $\tilde{W}^+, \tilde{W}^-$, mix in an analogous way into two mass eigenstates for each charge named Charginos $\tilde{\chi}_{1/2}^\pm$ [26]. In Tab. 2.7 all particles of the MSSM in their mass eigenstates are illustrated. The basis for this simulation and analysis is the benchmark point

particle	mass eigenstates	spin	P_R
Higgs bosons	h^0, H^0, A^0, H^+, H^-	0	1
squarks	$\tilde{u}_L^i$, $\tilde{u}_R^i$, $\tilde{d}_L^i$, $\tilde{d}_R^i$	0	-1
sleptons	$\tilde{e}_L^i$, $\tilde{e}_R^i$, $\tilde{\nu}_{eL}^i$	0	-1
neutralinos	$\tilde{\chi}_1^0$, $\tilde{\chi}_2^0$, $\tilde{\chi}_3^0$, $\tilde{\chi}_4^0$	$\frac{1}{2}$	-1
charginos	$\tilde{\chi}_1^\pm$, $\tilde{\chi}_2^\pm$	$\frac{1}{2}$	-1
gluino	$\tilde{g}$	$\frac{1}{2}$	-1

Table 2.7: *Particles of the MSSM in their mass eigenstates, where i is the family index $i = 1, 2, 3$. The column P_R shows the R-parity for the corresponding particles.*

SPS1a (see Tab. 2.6). Its particle spectrum is given in Fig. 2.7. Additionally, the masses for the neutralinos are shown in Tab. 2.9.

In Fig. 2.8 the cross-sections of all possible neutralino production channels as a function of the center-of-mass energy $\sqrt{s}$ are illustrated. The international linear collider (ILC) is designed to work in an energy range of 90 GeV to 500 GeV (see Chapter 3), with a projected upgrade to 1000 GeV. Table 2.8 shows the cross-sections for the neutralino production channels for a center-of-mass-energy of 500 GeV, which is the energy used in this study.

production of	$\tilde{\chi}_1^0\tilde{\chi}_1^0$	$\tilde{\chi}_1^0\tilde{\chi}_2^0$	$\tilde{\chi}_1^0\tilde{\chi}_3^0$	$\tilde{\chi}_1^0\tilde{\chi}_4^0$	$\tilde{\chi}_2^0\tilde{\chi}_2^0$
σ_{tot} in fb	280.29	63.62	7.22	0.90	60.90

Table 2.8: *Total neutralino production cross-sections for kinematically accessible channels at the ILC. Values are calculated for a center-of-mass-energy of 500 GeV and non-polarised electron and positron beams.*

Due to the small cross-section in this energy range, an access to the heavy neutralino $(\tilde{\chi}_3^0, \tilde{\chi}_4^0)$-system via pair production is not possible with an adequate rate, even at high energies. Hence, the only possible way to gain some information about this heavy neutralino system is through the "associated production" of a heavy neutralino together with the lightest one, i.e. a $(\tilde{\chi}_1^0\tilde{\chi}_3^0)$- or a $(\tilde{\chi}_1^0\tilde{\chi}_4^0)$-production. The main focus of this thesis lies on the $(\tilde{\chi}_1^0\tilde{\chi}_3^0)$-production channel, because the unpolarised cross-section for $(\tilde{\chi}_1^0\tilde{\chi}_4^0)$-production is by a factor

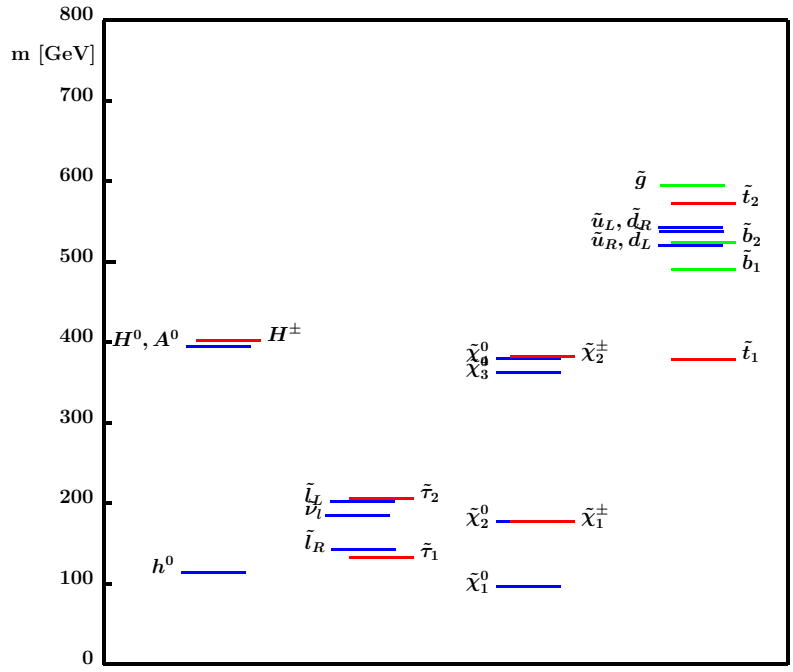

Figure 2.7: *SUSY particle spectrum for the benchmark point SPS1a [23].*

particle	$\tilde{\chi}_1^0$	$\tilde{\chi}_2^0$	$\tilde{\chi}_3^0$	$\tilde{\chi}_4^0$
mass in GeV	97.06	182.99	365.19	382.16

Table 2.9: *Neutralino masses for the benchmark point SPS1a [28]. The values are generated by SPheno, version 2.2 [29, 30].*

eight smaller than the $(\tilde{\chi}_1^0\tilde{\chi}_3^0)$-production (see Tab. 2.8). Moreover, a cross-section of 7.22 fb for the $(\tilde{\chi}_1^0\tilde{\chi}_3^0)$-production is quite small compared to the expected backgrounds (see Chapter 4). The Feynman graphs (s- and t-channel) of the $(\tilde{\chi}_1^0\tilde{\chi}_3^0)$-production are shown in Fig. 2.9. For the analysis, the signature of the $\tilde{\chi}_3^0$-decay is used. The main decay channels are mentioned in Tab. 2.10, whereas the corresponding Feynman graphs are shown in Fig. 2.10 and 2.11.

	BR	decay width
$\tilde{\chi}_3^0 \rightarrow \tilde{\chi}_1^\pm W^\mp$	59.5%	1.2 GeV
$\rightarrow \tilde{\chi}_2^0 Z^0$	21.0%	0.4 GeV
$\rightarrow \tilde{\chi}_1^0 Z^0$	11.3%	0.2 GeV

Table 2.10: *Main decays of the neutralino $\tilde{\chi}_3^0$ for SPS1a together with their branching ratios (BR) and decay widths. All other decays have a BR of 2% or less. Therefore, they are not listed here.*

Even though the decay $\tilde{\chi}_3^0 \rightarrow \tilde{\chi}_1^\pm W^\mp$ has the largest cross-section (see Tab. 2.10), it is not used in this analysis. The reason for this, is the missing mass constraint in this channel due to the neutrinos. In the two other channels there is such a constraint due to a possible cut on the Z^0 mass. The first goal of this thesis is to analyse whether it is possible to see a significant excess from the signal over the background in the two studied decay channels of the $\tilde{\chi}_3^0$

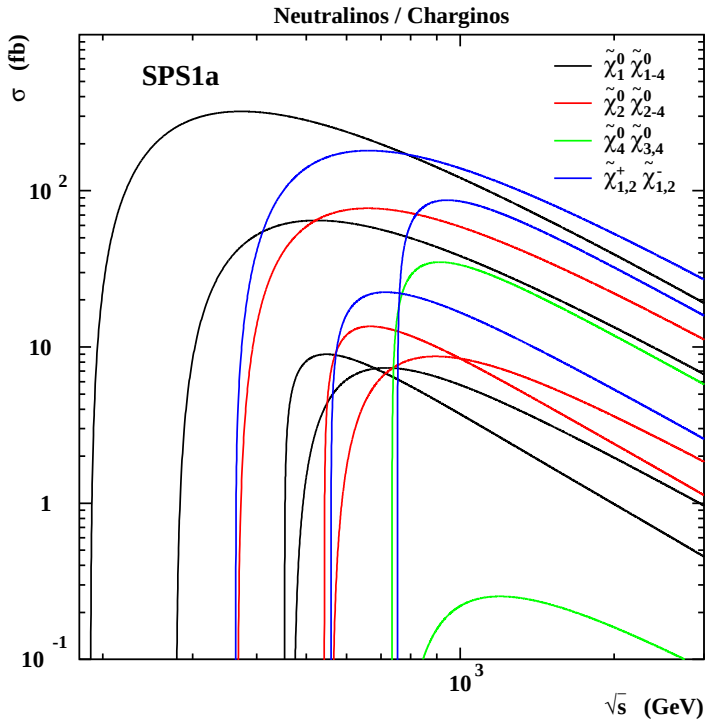

Figure 2.8: *Cross-section of all possible neutralino and chargino production channels as a function of the center-of-mass-energy $\sqrt{s}$ for non polarised electron and positron beams in e^+e^--collisions [27]. All other production channels, which are kinematically allowed, have a cross-section of less than 0.1 fb in the given energy range.*

decay (see Fig. 2.10). This analysis is done in a "cut-based" way (see Chapter 5). Secondly, it would be desirable to extract more properties of the heavy neutralino $\tilde{\chi}_3^0$, such as its mass in this associated production mode. This then also leads to a kind of consistency check of the SUSY sector, if the masses of the lighter neutralinos are already determined in previous measurements. In the MSSM it is possible to derive the masses of the heavy neutralinos from the masses of the two light ones [31]. Due to an independent measurement of the heavy masses

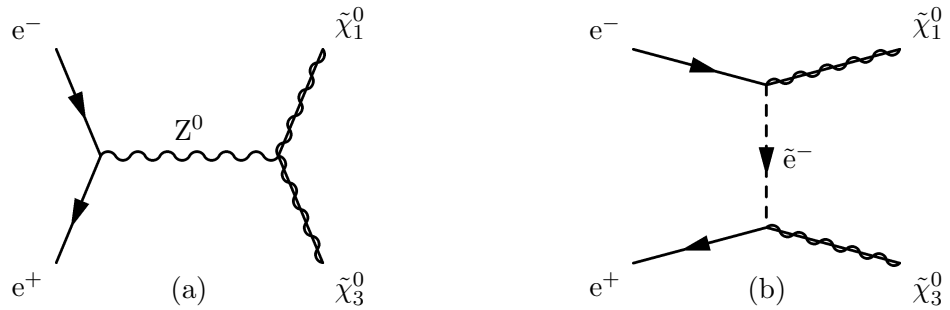

Figure 2.9: *Associated production of a heavy neutralino $\tilde{\chi}_3^0$ together with a light neutralino $\tilde{\chi}_1^0$. There are two graphs contributing to this process: (a) s-channel and (b) t-channel production. The neutralino $\tilde{\chi}_4^0$ is produced in the same way but in a lot smaller cross-section; hence, its graphs are overlayed (see Sec. 2.5 and Tab. 2.8).*

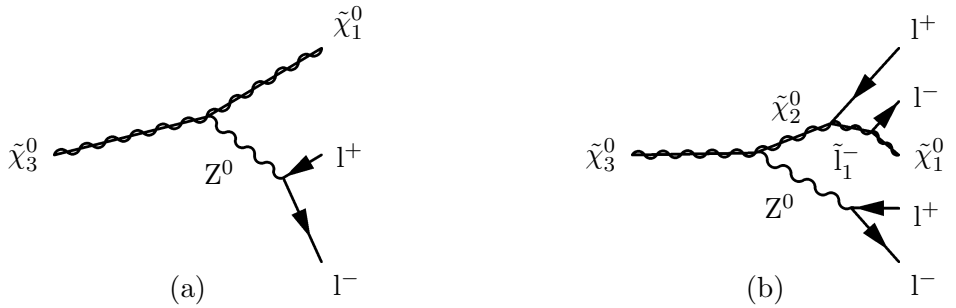

Figure 2.10: *Studied decays of $\tilde{\chi}_3^0$. For the Z^0-decay in both channels (a) and (b) only $e^{\mp}e^{\pm}$ and $\mu^{\mp}\mu^{\pm}$ final states are taken into account. In the second channel (b) all lepton flavours for the $\tilde{\chi}_2^0$-decay are considered. Due to the MSSM at SPS1a the main contribution comes from $\tilde{\chi}_2^0$-decays into $\tau^{\mp}\tau^{\pm}$ "pairs" (see Sec. 2.5 and Sec. 4.2 as well as Fig. 4.2, 4.3 and 4.4).*

production of	P(e^+)	P(e^-)	σ_{tot} in fb
$\tilde{\chi}_1^0\tilde{\chi}_2^0$	R	R	0.00
	R	L	232.12
	L	R	22.37
	L	L	0.00
$\tilde{\chi}_1^0\tilde{\chi}_3^0$	R	R	0.00
	R	L	0.23
	L	R	28.67
	L	L	0.00
$\tilde{\chi}_1^0\tilde{\chi}_4^0$	R	R	0.00
	R	L	0.78
	L	R	2.81
	L	L	0.00
$\tilde{\chi}_2^0\tilde{\chi}_2^0$	R	R	0.00
	R	L	243.53
	L	R	0.08
	L	L	0.00

Table 2.11: *Cross-section of the different neutralino production channels in dependency of the polarisation of the electrons and positrons. R and L denote right- and left-polarised electrons and positrons. The cross-section for the studied associated production $\tilde{\chi}_1^0\tilde{\chi}_3^0$ increases from 7.22 fb for unpolarised beams (see Tab. 2.8) to 28.67 fb for pure L-polarisation of the e^+ and pure R-polarisation of the e^-. The pure polarisation cannot be achieved technically. Therefore this maximum cannot be reached (see Sec. 3.1). A more detailed description of the polarisation can be found in Sec. 4.2.*

in this channel, it would be possible to check the consistency of the whole SUSY sector of the constraint MSSM and to hint at the realised SUSY parameter region in Nature [32, 33, 34].

Moreover, the ILC (see Chapter 3) is able to provide (spin) polarised electron and positron beams. This is essentially important for most SUSY processes. Tab. 2.11 shows the production cross-sections of the neutralinos at the ILC for a center-of-mass energy of 500 GeV in dependency of the polarisation of the electrons or positrons. All the neutralino production channels are strongly dependent on the polarisation of the incident electron beams. In the studied channel $e^+e^- \to \tilde{\chi}_1^0\tilde{\chi}_3^0$, the cross-section raises up from 7.22 fb for unpolarised beams (see Tab. 2.8)

to 28.67 fb for L-polarisation of the e^+ and R-polarisation of the e^-. Several important background processes, such as Z-pair production, are strongly dependent on the polarisation as well (see Chapter 4). Therefore, the analysis is performed for three different benchmark polarisations. They are described in Sec. 4.2. In the next chapter a more detailed description of the ILC itself is given, i.e. all the hardware components of the accelerator as well as the detector are described briefly.

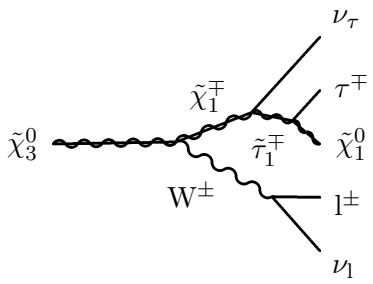

Figure 2.11: *Main decay channel of the $\tilde{\chi}_3^0$ in the MSSM at SPS1a (see Tab. 2.10). It is not taken into account in this study because of the missing mass constraint. The final state does not show leptons, which are originating from a Z^0 decay as in the studied channels (see Fig. 2.10). Therefore, a suppression of background processes seems not to be possible (see Sec. 2.5). Nevertheless these decays are included in the analysis as background processes (see Sec. 4.2).*

Chapter 3

The International Linear Collider

Most of the modern collider experiments are designed either as proton-(anti)proton or electron-positron colliders[1]. In the following, the main features of both types of machines are briefly described. The complementary character of the two concepts is shown.

Proton-(Anti)Proton Collider:

Due to the large mass of the proton compared to an electron, a higher center-of-mass energy can be reached with analogous accelerator technology. Therefore, a high discovery potential for heavy new particles is given[2]. On the other hand, these machines suffer from high background rates due to the nature of QCD interactions. Moreover, the accessible precision is smaller, because the initial state of the quarks and gluons in the proton is not exactly determined. An example for an existing machine is the Tevatron at Fermilab [37]. The next hadron collider will be the Large Hadron Collider (LHC), which is currently being built at CERN [38].

Electron-Positron Collider:

Electron-positron colliders act, in some sense, as counterparts to the proton machines. At this point it is necessary to distinguish between storage-rings and linear accelerators. The storage-rings reach smaller center-of-mass energies due to energy loss by synchrotron radiation. The energy loss per circulation ΔE, is given by

$$\Delta E \simeq const. \cdot (\frac{E_0}{m_0 c^2})^4 \cdot \frac{1}{R}, \tag{3.1}$$

where E_0 is the particle energy, m_0 its mass, c the speed of light and R the radius of the accelerator. The energy loss is scaling with the fourth power of the desired energy. Therefore, it is not efficient to build a circular electron-positron collider above a certain center-of-mass energy, and hence, the discovery potential is limited. Linear accelerators do not suffer from energy loss due to synchrotron radiation as mentioned above, but they are limited by more technical reasons. Unlike in a circular accelerator, the "accelerating devices", i.e. microwave cavities, in a linear collider are only passed once by the particle bunches. Therefore, it is necessary to equip a linear accelerator along the whole acceleration path with such cavities. In order to reduce the length and therefore the costs of such a accelerator, high acceleration gradients, are needed, which is a serious technical challenge. These disadvantages are slightly

[1] One exception is the "Hadron Elektron Ring Anlage" (HERA) located at DESY in Hamburg, where the collision of protons and electrons is studied.

[2] e.g. the discovery of the top quark at Tevatron [35, 36]

compensated by the fact that the repetition rate can be high and that the bunch size at the IP can be reduced to a very small value. Thus, high luminosities can be reached. The International Linear Collider (ILC) (see Sec. 3.1, 3.2 and Tab. 3.1) is an example of such an accelerator.

Lepton colliders offer important benefits. They provide, due to their "point-like" particles, clear initial states and offer a much cleaner experimental environment due to the missing QCD background. Therefore, a complete kinematic reconstruction of many events is possible. The desired measurement precision is of the order of a percent, which is a challenge for theory as well. Examples of lepton colliders are: LEP at CERN [39], as a former cyclic electron accelerator, and the Stanford Linear Accelerator (SLC) at SLAC [40]. The next linear lepton collider will be the ILC, which is in its project planning phase. The proposed features of the ILC are the basis for the simulations used in this thesis (see Sec. 3.3 and Chapter 4).

The ILC is designed to be an e^+e^- collider with center-of-mass energy range of 90 GeV to 500 GeV. The layout also includes an upgrade option to 1000 GeV. The main goals of the ILC are the following:

- Perform high precision measurements of the Higgs sector, i.e. the SM Higgs sector as well as an extended SUSY Higgs sector and therefore investigation of the complete structure of the electro-weak symmetry breaking mechanism.

- Supersymmetry is a promising extension of the Standard Model (see Chapter 2) and many of the particles, which are predicted in different models, are accessible with the ILC (at least the lighter constituents of the particle spectrum (see Fig. 2.7)). Therefore, another goal is to carry out precise measurements in the SUSY sector, if SUSY is realised in Nature.

- The production of $t\bar{t}$-pairs from the production threshold to several 10 GeV beyond is possible within the proposed energy range. This allows the measurement of the t-mass within a accuracy of approximately 100 MeV. The top-quark mass is an important SM parameter and its precise knowledge is important for many models beyond the SM (BSM).

- The ILC offers the potential for discoveries in those regions of the model parameter space, which the LHC cannot access.

- Last but not least, highly accurate experiments on the coupling constants of the interactions in the SM are planned, which allows comprehensive tests of the SM.

The ILC and the LHC are complementary experiments. By combining the performance of both machines it is possible to reconstruct the main parts of the SUSY Lagrangian (see Sec. 2.2). Moreover, due to the precise measurements in the electro-weak, Higgs and SUSY sector, it is possible to set constraints on new physics at the GUT or Planck scales. All these ambitious goals require a highly developed machine with an efficient, high-performance accelerator and a powerful detector. The simulation and analysis, which is described in this thesis, is based on the TESLA project (Tera Electronvolt Superconducting Linear Accelerator) [41]. In the summer 2004 the International Technology Recommendation Panel of ICFA (International Committee for Future Accelerators) recommended a superconducting accelerating technology for the ILC [42].

The TESLA machine configuration is built like a typical linear collider, i.e. there are two Linear Accelerators (Linacs) aligned face to face with a length of 15 km each. In between the Linacs an interaction region is located, where the detector will be located (see figure 3.1). A

second interaction region with a second detector can be additionally equipped. The length of the whole system is planned to be 33 km with an desired center-of-mass energy range of 90 GeV to 500 GeV, upgradeable to 1000 GeV. In the following Sections the main features of the accelerator and the detector are described.

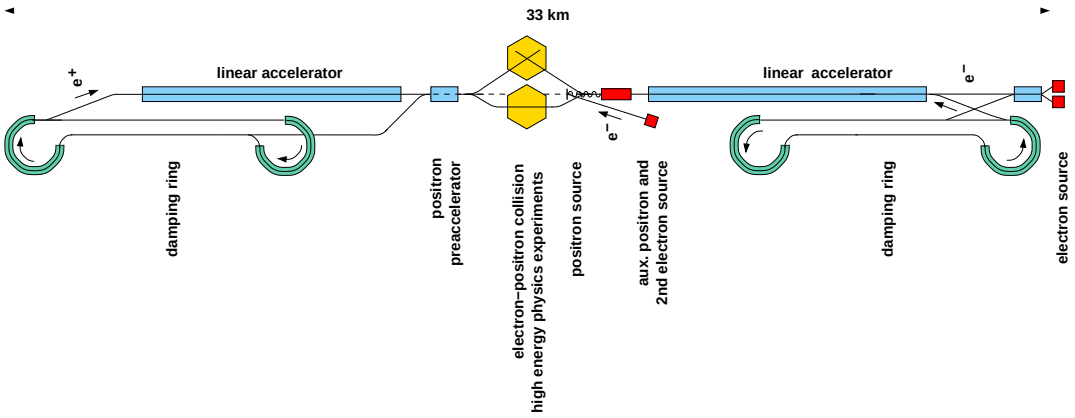

Figure 3.1: *Sketch of the TESLA accelerator [41]*

3.1 The Accelerator

Figure 3.1 shows a sketch of the TESLA accelerator. A laser driven electron source provides a beam of polarised and pre-accelerated electrons with an energy of 5 GeV. The electrons then enter a damping ring to reduce their emittance. This is done by alternating translatorical acceleration and emission of synchrotron radiation due to curved sections. The synchrotron radiation is emitted isotropically, whereas the acceleration is clearly directed. These two processes lead to an enrichment of electrons with a momentum parallel to the accelerator axis and therefore to a reduction of the emittance. After that, the electrons are accelerated in the Linac towards the interaction point up to their final energy. In front of the interaction point a so called Wiggler, which is an array of alternating magnetic fields, is passed. This leads to an emission of synchrotron radiation parallel to the beam axis, that is used to produce e^+e^--pairs in a thin target. Now the positrons are extracted, passed through the second damping ring and are accelerated in the second Linac, in an analogous way like the electrons. Finally, the positrons are delivered to the interaction region. In Table 3.1 a short overview of the main collider parameters is given. Due to the high luminosity (see Tab. 3.1) the beams are extremely collimated and carry large electrical charge in each bunch. The electrons of one bunch radiate against the the coherent field of the other bunch[3]. This leads to beam-beam interactions and an energy loss of the beam particles. For the simulation of events this effect has to be taken into account. Some important benefits of the TESLA layout are as follows: First, the center-of-mass energy is tunable, which allows cross-section measurements close to the production threshold of particles (threshold scans). Second, the layout offers polarised beams, which is important to disentangle various states and to suppress backgrounds. This is in particular important for the production of SUSY particles (see Sec. 4.2). Technically, it is not possible to provide 100% right- or left-polarised electrons and positrons as it is mentioned in Tab. 2.11. The goal it to enhance the polarisation for the electron and positron beam as

[3]also known as “beam strahlung”.

E_{CM}	500	800	GeV
bunch separation	337	176	ns
acceleration gradient	23.8	35	MeV/m
repetition rate	5	4	Hz
RF frequency	1.3	1.3	GHz
σ_x	554	392	nm
σ_y	5	2.8	nm
σ_z	300	300	μm
N_e per bunch at IP	$2.0 \cdot 10^{10}$	$1.4 \cdot 10^{10}$	1
luminosity	$3.5 \cdot 10^{34}$	$5.3 \cdot 10^{34}$	$\mathrm{cm}^{-2}\mathrm{s}^{-1}$

Table 3.1: *Some basic collider parameters of TESLA for a desired center-of-mass energy E_{CM} of 500 and 800 GeV (see [41] and [43]), where σ_i $(i = x, y, z)$ symbolises the size of a particle bunch in x-, y- and z direction. The typical number of electrons per bunch at the interaction point (IP) is given by N_e.*

much as possible. The typical benchmark polarisations, which are used in this thesis are given in Sec. 4.2. Technically, it is more difficult to produce polarised positrons. In the layout of the ILC a maximum polarisation of 0.8 for the electron beam is aimed at and -0.6 for the positrons. For both beams both directions of polarisations are possible. This is indicated by the sign of the polarisation, e.g. P = 0.8 means the beam consists of 90% right-handed and 10% left-handed particles and P = −0.6 denotes 80% left-handed particles and 20% right-handed. The calculation of these numbers is shown in Sec. 4.2. The polarisation is important for most of the SUSY processes. Especially for the studied processes in this thesis, it is interesting, because the signal is enhanced and some background processes are suppressed for particular choices of the polarisation (see Sec. 2.5 and 4.2). Another feature of the ILC is the e^-e^--, $e\gamma$- and the $\gamma\gamma$-option. This allows for complementary and redundant measurements (cross-checks). A more detailed overview is given in [41]. In the next part of this chapter a more detailed description of the detector is given.

3.2 The Detector

To achieve the goals described at the beginning of this chapter, a powerful, high precision detector is needed, which must exceed most detectors of today in performance. The TESLA detector follows the layout of a typical collider detector. This means, close to the interaction region tracking detectors are located. In the case of the TESLA detector the tracking system consists of a Vertex Detector, surrounded by a Silicon Intermediate Tracker (SIT) and Forward Tracking Disks (FTD). These devices are enclosed by the Time Projection Chamber (TPC), as the main tracking device. Beyond the TPC, the calorimetric system is mounted. Ideally, it covers the whole solid angle around the interaction point (IP) and it consists of the electro-magnetic calorimeter (ECAL) and the Hadronic Calorimeter (HCAL). Adjacent follows the coil and the yoke, where the yoke itself is instrumented for tracking muons. Next to the vertex detector and the FTDs under small polar angles, Low Angle Taggers (LAT) are mounted. They are instrumented with calorimeters to measure the luminosity. A global overview of the detector is given in Fig. 3.2. In Fig. 3.3 a more precise sketch is given.
[4] The ILC provides a clean experimental environment and extreme measurement precision. Hence, it will be possible to focus on the reconstruction of individual particles. Moreover,

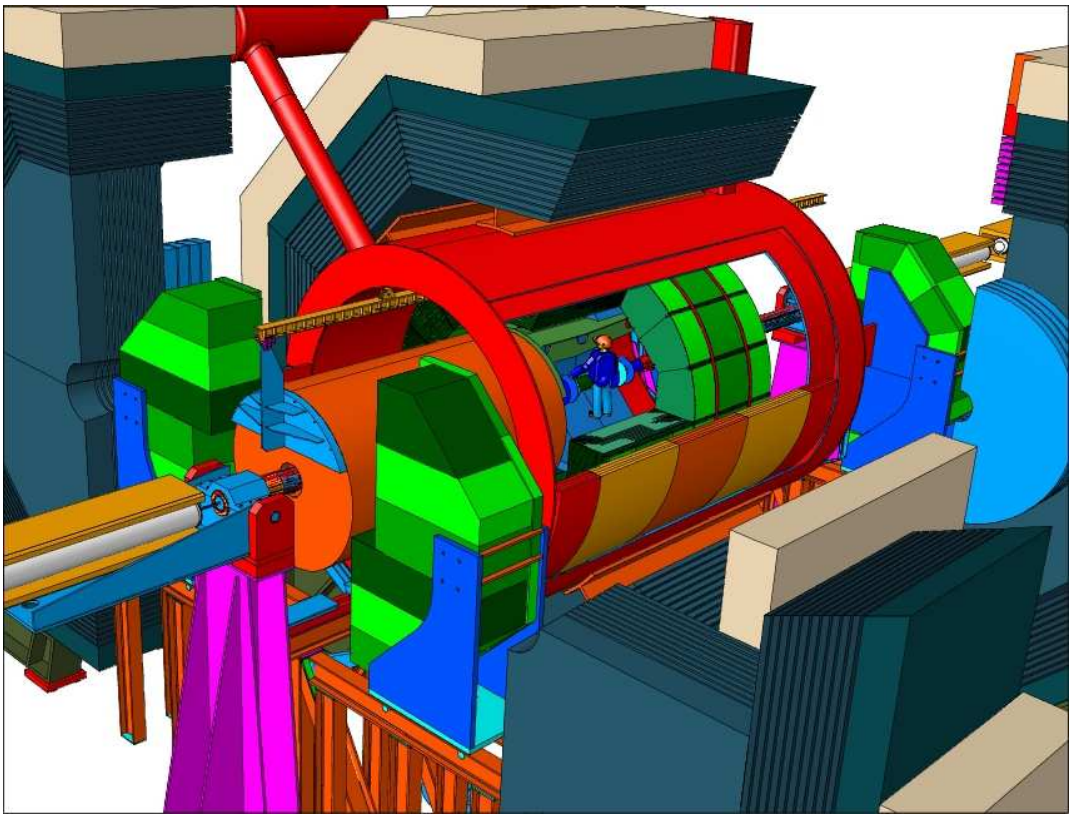

Figure 3.2: *Three dimensional sketch of the TESLA detector. A coil with 8 m length and 6 m inner diameter contains the complete vertexing, tracking and calorimetry. The muon system is installed outside the coil.*

the experiments will look for processes with small cross-sections, as studied in this thesis (see Sec. 2.5 and 4.2). Therefore, a high precision detector as well as an advanced particle reconstruction concept is needed. Such a concept is given by the so-called "Particle Flow Algorithm", which is described in the following paragraph.

Particle Flow Concept

Charged particles and photons carry about 90% of the energy in e^+e^- collisions. Hence, in the Particle Flow Algorithm first the momenta of all charged particles ($\sim 62\%$) is measured by the central tracking system (see Sec. 3.2.1). Charged particles also deposit energy in the electro-magnetic and hadronic calorimeters (see Sec. 3.2.2). Therefore, these calorimeter hits are assigned to the tracks of the charged particles and are subtracted from the remaining calorimeter hits. The remaining calorimeter hits then are combined into neutral objects by applying a clustering algorithm. Among these neutral objects are $\sim 26\%$ photons, which can be detected by the electro-magnetic calorimeter, and neutral hadrons ($\sim 10\%$), which can be measured together by the electro-magnetic and the hadronic calorimeter. Hence, this algorithm provides a reconstruction of single particles. This is especially important for SUSY processes, where a lot of missing energy is expected (see Sec. 2.3 and Fig 4.2 and 4.4). In Fig. 3.4 a comparison between the hadronic energy resolution of a jet of $\Delta E_{jet}/E = 60\%/\sqrt{E}$, which was a typical resolution at LEP, and $\Delta E_{jet}/E = 30\%/\sqrt{E}$, which is the required resolution at the ILC. The energy is in GeV. The increase in separability is apparent. For more

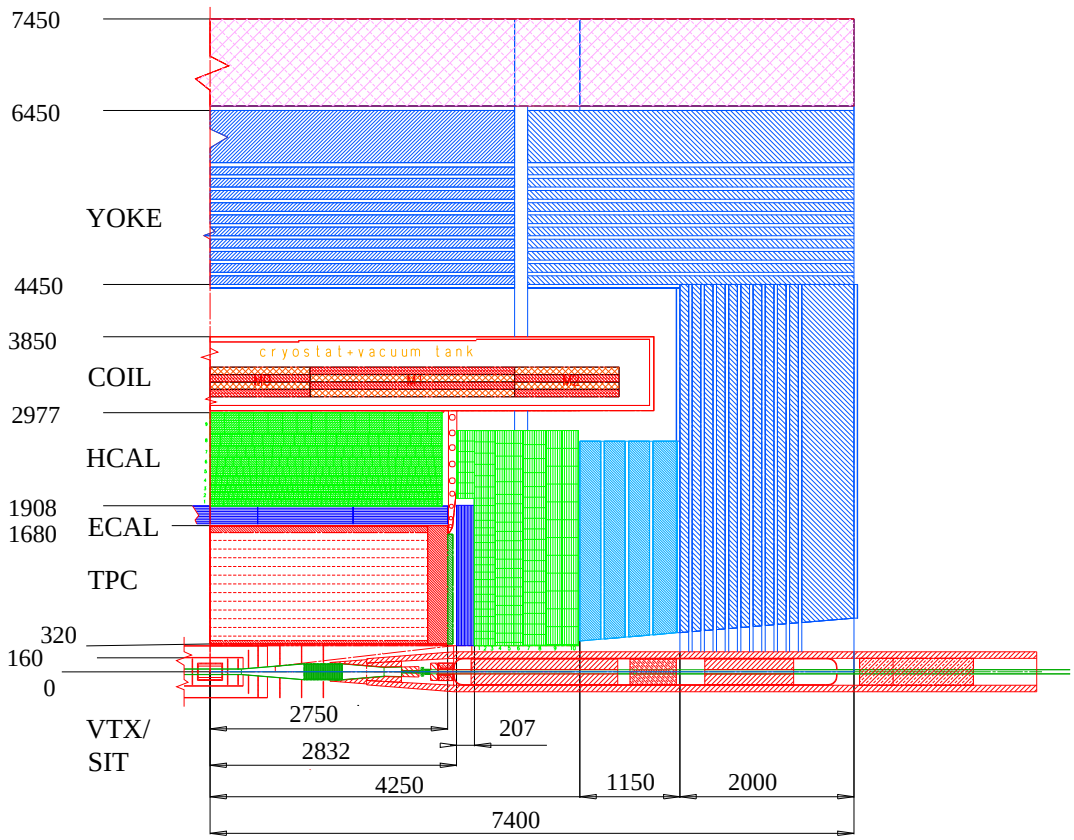

Figure 3.3: *View on an octant section of the TESLA detector, numbers are given in mm. The sub-devices are described in the text more precisely [41].*

information on the Particle Flow Algorithm see [41]. The consequences of the Particle Flow Concept for the technical layout of a detector are: First, a calorimetric system with a extremely high granularity is needed to resolve closely neighboring showers (more important for the electro-magnetic calorimeter than for the hadronic). Moreover, a good time resolution is required to avoid a "pile-up" in the calorimeters. The tracking system should provide high double track resolution, in order to resolve dense jets. Additionally an excellent linkage between tracking system, electro-magnetic and hadronic calorimeter is necessary to assemble the Particle Flow Objects.

These requirements are considered in the layout of the TESLA detector. In the following paragraphs the constituent parts are described more precisely. Further information on the detector sub-systems can be found at [41]. A more detailed overview of the TESLA detector is given in Fig. 3.3.

3.2.1 The Central Tracking System

The Central Tracking System contains the Vertex Detector, SIT, FTDs and the TPC. All these devices are designed to detect the tracks of electrically charged particles. Most important aspects are: Precise measurement of primary and secondary vertex, momentum measurement and determination of the specific energy loss in the TPC. The last aspect offers the chance to establish a hypothesis about the type of the particle. Moreover, there are two Forward Chambers mounted on the faces of the TPC to improve the momentum measurement of

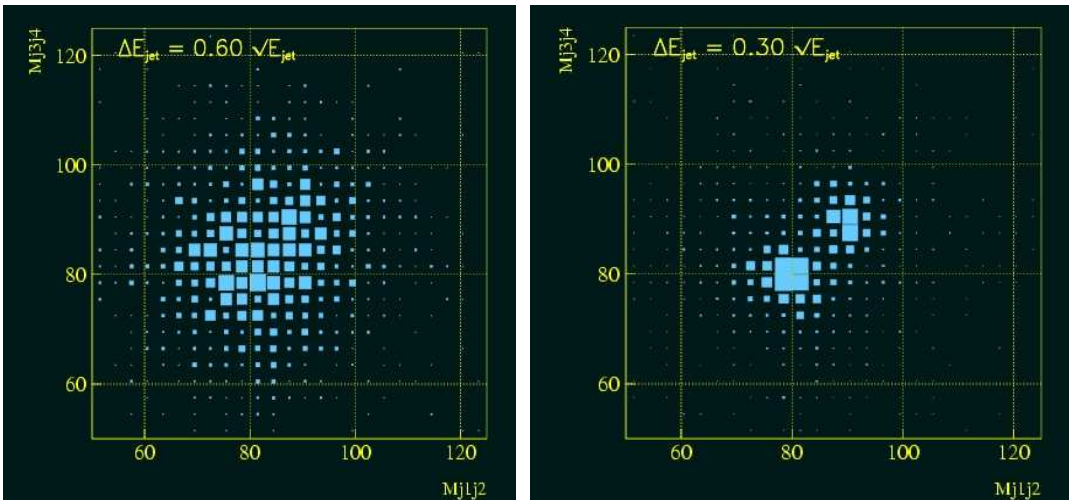

Figure 3.4: *Comparison between the hadronic energy resolution of a jet of* $\Delta E_{jet}/E = 60\%/\sqrt{E}$, *which was a typical jet-energy resolution at LEP, and* $\Delta E_{jet}/E = 30\%/\sqrt{E}$, *which is the aimed resolution at the ILC. The energy is in GeV. The Picture shows as an example the separation of W- and Z-pairs decaying hadronically. On all axis the hadronic di-jet masses are given. The increase in separability is apparent [44].*

particles with very low polar angle. In the following Sections the Central Tracking System is described, starting with the inner parts and ending with the TPC:

The Vertex Detector

The device, which is mounted closest to the interaction point (IP) is the Vertex Detector. It is designed to detect secondary vertices in long decay chains or in the decay of heavy quarks (e.g. b- and c-quarks) or tau-leptons. It is build up as an Silicon-Pixel detector with five independent layers and a spatial resolution of 3.5 μm. With this high resolution it is possible to reconstruct the tracks down to the vertex. This improves the performance of the whole tracking and particle identification procedure. The innermost layer is mounted at a radius of 1.55 cm from the beam pipe and the outermost has a radius of 6 cm.

The Forward Tracking Disks (FTD)

In order to increase the momentum resolution for tracks with small polar angles on each side of the Vertex Detector seven silicon disks are mounted perpendicularly to the beam axis. They are sensitive for polar angles down to 7°. The first three disks are designed to be pixel-detectors with a resolution of 5 μm, the other four are strip detectors with a resolution of 25 μm.

The Silicon Intermediate Tracker (SIT)

Between the Vertex Detector and the TPC the Silicon Intermediate Tracker is located. It consists of two cylindrical silicon strip detectors with a resolution of 10 μm, which are mounted at radii of 16 and 30 cm. The SIT increases the momentum resolution of particles with large polar angels as well as the correlation-power of different tracks in TPC and Vertex Detector. Moreover, the reconstruction of secondary vertices of long-lived particles is improved (e.g. K^0_S).

interaction point	δIP	$\sim 5\mu\text{m} \oplus 10\mu\text{m}/\sin^{\frac{3}{2}}\theta$
tracking system	$\frac{\delta p}{p}$	$\sim 10^{-4}$
ECAL	$\frac{\delta E_{em}}{E_{em}}$	$\sim \frac{13\%}{\sqrt{E}}$
HCAL	$\frac{\delta E_{jet}}{E_{jet}}$	$\sim \frac{35\%}{\sqrt{E}}$

Table 3.2: *Desired resolutions for the ILC detector. All numbers refer to the TESLA detector.*

The Time Projection Chamber (TPC)

The main device of the tracking system is the Time Projection Chamber (TPC). The TPC is a cylindrical gas detector with a diameter of 170 cm and a length of 5.4 m filled with Ar-CH_4-CO_2 at atmospheric pressure. Charged particles passing the gas volume, ionise the gas along the length of the track. The electrons from this process are accelerated due to an electric field towards one face of the TPC. There a multiple Gas-Electron-Multiplier-Structure (GEMs) amplify the generated charge and suppress the ion feedback. Finally, the charge is read out via pads located at the barrel face. With a high number of read out cells, it is possible to ensure a high track resolution even for high jet multiplicities. The presence of a solenoid magnetic field in the TPC will cause the particles to follow a helix. By measuring the curvature of the helix, it is possible to determine the momentum of the particle. According to the Particle Flow concept the most important features of the TPC are the following: First one needs an excellent momentum resolution and second a high ability to separate double tracks. More information on the desired resolutions are given in Tab. 3.2. Moreover, the TPC allows particle identification via the specific energy loss due to ionisation. This is described by the Bethe-Bloch-Formula and its extensions. The energy loss of a charged particle due to ionisation is a function of the particle velocity. By measuring the momentum, which is given by the curvature of its ionisation-path in a magnetic field, and measuring the mean energy loss, a prediction with different probabilities for different particle mass hypotheses is possible.

3.2.2 The Calorimeter System

The calorimeter system is used to measure the energy of particles. It is divided into two parts: First the electro-magnetic calorimeter (ECAL), which measures the energy of electro-magnetically interacting particles, such as electrons and photons, and second the hadronic calorimeter (HCAL), which measures the energy of strongly interacting particles. To be more precise it should be said, that the ECAL represents approximately one nuclear interaction length and therefore it is probable that hadrons already deposit some energy in the ECAL. Because of this, the whole calorimetric system is used to measure the energy of hadrons. Moreover, it is important to cover the whole solid angle around the interaction point with sensitive material as well as to dispel all interfering material. Hence, the whole calorimetric system is designed to fit within the coil. This increases the angular resolution especially for photons. In Fig. 3.3 a detailed view on the TESLA detector and, in particular, the calorimetric system is given. For further information see [44].

Electro-Magnetic Calorimeter (ECAL)

In the ECAL tungsten is used as absorber material and silicon detectors with a size of $1 \times 1\text{cm}^2$ provide the measurement of the energy. This high granularity ensures a precise determination of the direction of photons, a good separation of electrons and pions due to their spatial shower

evolution and an exact classification of charged and neutral clusters. The ECAL consists of 30 layers of tungsten with a thickness of 1.4 mm each and 10 layers of tungsten with 4.2 mm together with 10 layer of silicon with 1.4 mm. This gives an overall thickness of 184 mm, which is equivalent to a radiation length of $24 \cdot X_0$ and a nuclear interaction length of approximately $1 \cdot \lambda$. Information about the desired resolutions can be found in Tab. 3.2.

Hadronic Calorimeter (HCAL)

Due to the nuclear interaction length of approximately $1 \cdot \lambda$ for the ECAL, the hadrons only lose some of their energy in the ECAL. Therefore, the ECAL is enveloped in another calorimeter, namely the HCAL, which is designed to measure the energy of strong interacting particles. Here 40 layer of stainless steel with a thickness of 2 cm are used as absorber material and just as many layer of 0.5 cm thick scintillators for the detection. The readout is designed via scintillating fibers and Avalanche Photo Diodes (APDs). The overall granularity is aimed to be $5 \times 5\text{cm}^2$. The HCAL is designed as a sampling calorimeter. End-caps located next to the faces of the Central Tracking System increase the acceptance of the whole Calorimetric System down to polar angles of 4°. The end-caps are proposed to have nuclear interaction length of $10 \cdot \lambda$, because the medium deposition of energy increases with smaller polar angles. The whole calorimeter system is designed to provide a nuclear interaction length of at least $4.8 \cdot \lambda$ in any direction. For more information on the desired resolutions see Tab. 3.2.

Coil and Muon detector

The inner detector, consisting of central tracking and calorimetric system, is surrounded by a superconducting coil, which generates a solenoid magnetic field of 4 T. The outer side of its Yoke furthermore is furnished with muon detectors. It would be possible to enhance the hermeticity of the Calorimetric System, if a high segmentation for the muon detector is used. In this case extensive showers could be detected outside the coil.

3.2.3 The Low Angle Tracker (LAT) and Luminosity Calorimeter

These two devices are not part of the tracking system, although they are mounted at the center of the detector. In order to reach the desired luminosity of $3.5 \cdot 10^{34}\ \ cm^{-2}s^{-1}$ for a center-of-mass energy of 500 GeV the dense bunches of electrons and positrons need to be focused strongly. Hence, Beamstrahlung is not negligible anymore (see Sec. 3.1). To reduce these high energetic photons and secondary particles the mask is introduced, which is built of tungsten and carbon to provide an effective shielding. Besides this the Low Angle Tracker (LAT) and the Luminosity Calorimeter are implemented. The LAT ensures the detection of particles with polar angles from 23.5 mrad to 83.0 mrad and the Luminosity Calorimeter measures the luminosity of the e^+e^- interaction.

3.3 Detector Simulation at the ILC

The simulation of e^+e^- interactions at the ILC is done in two steps: First, an event generator is used to produce the four momenta of desired interactions in e^+e^--collisions (see Chapter 4). That means, such a generator provides the four momenta of all final state particles in e^+e^--collisions in a statistical way, weighted according to their production cross-sections. In this thesis the Monte Carlo event generator PYTHIA, version 6.3, is used [45, 46]. Second, the interactions of the particles with the detector are simulated. For this, there are again two general methods of simulation. The first, more complex way, is to build an exact computer

model of the detector. That means all geometric aspects, dimensions and properties of the detector material are taken into account. The path of a particle through the detector then is calculated in steps. That means, the initial energy and momentum of the particle calculated, provided by the event generator, is used to determine the interaction of the particle with the detector material at a certain (entry) point of the detector. As a consequence of the interaction the energy and the momentum of the particle are changed. The particle then travels a certain distance freely through the detector, before the next interaction is calculated. The length of the free path is calculated according the radiation length X_0 and the nuclear interaction length λ of the particle in the certain material. So at the end, this procedure is a kind of finite element method. At each point of the calculation bremsstrahlung, ionisation, decays of exited atoms, decays of the particles, as well as all relevant nuclear interactions are taken into account.

Additionally, there are software tools, which are able to simulate the response of the electronics of the detector system, the timing dependencies and the particle reconstruction. A simulation performed in such a way offers a high accurate model of the detector with realistic uncertainties on momentum and energy, as well as on electronics and particle reconstruction methods. On the other hand, it needs a lot of computation time, especially, if precise predictions are needed. For the TESLA detector these kind of simulations already have been done and further development is going on. The tool, which is used for the TESLA detector is BRAHMS [47]. It is based on the software package GEANT3 [48], a program which describes the passage of elementary particles through matter.

The second basic way to model a detector is to build a so-called "parametrised simulation". Therefore, it is necessary to know the response of the detector, when a particle is passing it. That means, knowing all the uncertainties of measured variables, the resolutions and the noise caused by the detector itself or electronics etc. All this data is obtained by a full simulation as mentioned above. With this knowledge, it is possible to obtain a relation between the four momenta produced by the event generator and the full output of the desired detector. This is the so-called "parametrised simulation", which is used in this thesis in the form of the software package SIMDET4 [49, 50]. The main advantage of such a method is the speed of the calculation compared to the full simulation mentioned above. Moreover, several reconstruction algorithms can be performed on this output data, so that one can access result files with already "particle like" entries. In this thesis the particle flow algorithm is performed at this stage. For more information about the particle flow concept see Sec. 3.2. Hence, in the output file there are already particle flow objects with corresponding energies and momenta available. Additionally, a second algorithm is applied. It is used to identify leptons within the particle flow objects [27]. A more detailed description of the whole simulation procedure is given in the next Chapter.

Chapter 4

Simulation of Signal and Background Events

In this chapter the simulation of signal and background events is described in a more detailed way. For the background a whole set of simulated events is used. This set consists of SM and SUSY processes, which show a similar final state compared to the signal process, i.e. mainly all possible leptonic final states with up to six leptons, in order to include misidentifications in the final states. In the next two sections, a more detailed description of the simulation tools and particle reconstruction algorithms is given, and second, the two studied signal channels (see Fig. 2.10) as well as the background processes are described (see Sec. 4.2).

4.1 Simulation Tools

In Fig. 4.1 a schematic overview of the simulation tools and their relations is illustrated.The simulation is divided in two basic parts. The first part is the simulation of events, which are caused by e^+e^--collisions. This is done by the Monte Carlo event generator PYTHIA, version 6.3 [45, 46]. It needs several input parameters such as the desired interactions, decays and final states, center-of-mass energy of the e^+e^--collisions and the number of events to be calculated. With this information PYTHIA generates the four momenta of the particles created in this collision in a statistical way. The statistical generation of events is weighted with the appropriate cross-sections and branching ratios (BR). The specific SUSY model studied in this thesis is the MSSM at SPS1a (see Sec. 2.4). The SUSY mass spectra, branching ratios and couplings are derived by SPheno [29, 30], a SUSY spectrum generator. In this thesis SPheno version 2.2 is used. The sparticle masses, cross-sections, and BRs calculated by SPheno, serve as an input for PYTHIA. The connection between PYTHIA and SPheno is given by the SUSY Les Houches Accord [51], which is an universal set of conventions to interface SUSY spectrum calculators, decay packages and event generators. One exception is made for MSSM Higgs processes. Their spectra are calculated by FeynHiggs, version 2.1 [52], which also offers a SUSY Les Houches Accord interface and which provides more accurate calculations of the Higgs sector than SPheno.

All the four momenta calculated by these tools are then fed into SIMDET4, the second part of the simulation chain, which determines the response of the ILC detector in a parametrised way (see Sec. 3.3) [49, 50]. The basis for this parametrised simulation is the technical design described in [41] and the full detector simulation done with BRAHMS (see Sec. 3.3). SIMDET4 applies a Gaussian smearing to the momenta of charged particles and to the impact parameters with resolutions obtained from the full simulation. The calorimeter

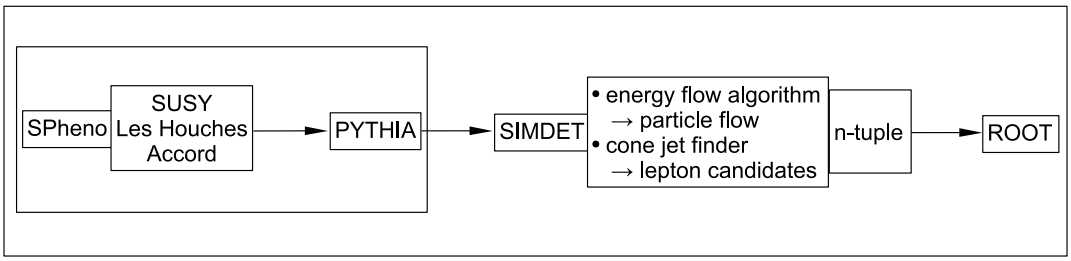

Figure 4.1: *Schematic overview of the chain of used simulation tools.*

response is also calculated by using a parametrisation of results from the full simulation. Pattern recognition is emulated by means of cross reference tables between generated particles and detector response. In Tab. 4.1 the detector parameters used for the simulation are shown.

SIMDET4 offers an algorithm, which connects tracks and clusters of deposited energy in the calorimeter system to so-called "energy flow objects"[1]. It is based on the algorithm already introduced in SIMDET3 [53] and it works in the same way as the particle flow algorithm mentioned in Sec. 3.3. The energy flow objects represent the output of reconstructed particles of SIMDET4. Due to the fact that in the studied channels (see. Fig. 2.10) only leptonic final states are taken into account, a second algorithm is used, which sorts out "lepton-like" objects on the basis of the energy flow objects. The found objects then are named "lepton candidates". The basis for this algorithm is a cone-jet-finder [54, 55, 56, 57]. The starting point for this jet finding algorithm is the direction of a arbitrarily chosen energy flow object, which exceeds an energy of 0.5 GeV. Its direction is then interpreted as a initial jet axis, around which a cone with a fixed opening angle (half width) is set at $R = 0.2$ rad (11°). The momenta of all particles lying in this cone are added vectorially and the result defines a new cone axis. This procedure is iterated until a stable jet is found, which then is named "proto-jet". The whole procedure is repeated until the maximum number of jets in an event is determined. Due to the construction of the proto-jet it is possible, that several proto-jets overlap, and thus particles belong to different jets. The next step therefore is to find a unambiguous relation between proto-jets and particles. Depending on the fraction of the entire energy of a proto-jet and on the angular distance to a proto-jet, a particle is either related to the proto-jet with the higher energy or with the smaller angular distance. This is repeated for all proto-jets and hence, all particles are related to a unique jet. At the end a cut on the entire energy of the proto-jets is performed at 0.7 GeV. Proto-jets with too small energy are discarded and the remaining are accepted as reconstructed jets. If there is no tracks in such a jet, this jet is determined to be a neutral jet. Jets with tracks but with a net charge of zero are assigned to be a charged jet.

Subsequently, the search for lepton candidates is performed. Originally, this lepton candidate algorithm has been developed to find tau leptons [27, 58], but also electrons and muons are selected with high efficiency ($\sim 80\%$) (see Tab. 4.3). The selection of lepton candidates is performed in two steps. First several cuts are applied on the found jets, which can be found in Tab. 4.2. With the cut on the charge all neutral jets are rejected. Due to the fact, that for leptons isolated cones are needed, a second, so-called isolation cone is placed around the cones,

[1] In a real detector a particle would generate a signal in many cells of the Calorimetric System. These cells are treated as clusters in SIMDET4.

Vertex detector: CCD (1.5 cm beam pipe)	
acceptance $\cos(\theta)$	0.96
Tracker	
mag. field	4.00 Tesla
total length of TPC	5.00 m
inner radius of TPC	0.36 m
outer radius of TPC	1.62 m
p_t^{min}	0.10 GeV
overall acceptance $\cos(\theta)$	0.992546
TPC acceptance $\cos(\theta)$	0.978148
ECAL	
min. deposited energy	0.20 GeV
acceptance $\cos(\theta)$	0.996549
HCAL	
min. deposited energy	0.50 GeV
average energy deposited by muons	3.80 GeV
acceptance $\cos(\theta)$	0.996549
LAT	
min. energy of particle	5.00 GeV
min acceptance $\cos(\theta_{min})$	0.999622
max acceptance $\cos(\theta_{max})$	0.996549
angular resolution parameter θ	0.040
angular resolution parameter ϕ	0.262
Low angle calorimeter	
min acceptance $\cos(\theta_{min})$	0.999989
max acceptance $\cos(\theta_{max})$	0.999622
muon parameter	
min energy for isolated muons	5.00 GeV

Table 4.1: *Detector parameters used for the simulation (see Chapter 3 as well).*

in which no further track is allowed. Entries of neutral energy within this cone are allowed. Otherwise the algorithm would reject leptons radiating a photon when they pass the tracking system. All jets, which pass these criteria are addressed to be tau lepton candidates. The candidates are then sorted due to their number of tracks. Candidates with three tracks are determined to be 3-prong tau candidates. Candidates with one track are denoted as electron candidates, if they show a track and a full energy deposit in the ECAL, or as muon candidates, if they behave like a minimum ionizing particle (MIP), i.e. they show a track and sparse energy in the ECAL. The remaining one track candidates are identified as 1-prong hadronic taus. Tab. 4.3 shows the overall efficiencies for these selections. This is the concept of the lepton candidate algorithm, which was found to work best for the kind of processes studied in this thesis. The whole analysis (see Chapter 5) is based on the lepton candidates provided by this algorithm.

For all simulated channels beam-strahlung as well as initial state radiation (ISR) is taken into account. Beam-strahlung is implemented due to the CIRCE software package [59, 60] in version 1.2. The output data is stored in the "ntuple-format", which contains all relevant information, from lepton-candidate four-momenta down to tracker and calorimeter data as

cut on	
multiplicity	$n_{jet} = 1$ or $n_{jet} = 3$
charge	$q_{jet} = \pm e$
invariant mass	$m_{jet}^{inv} < 2\text{GeV}$
pseudo-rapidity	$\|\eta\| < 2$ $(\sim 15^\circ)$
and no further tracks in a 15° isolation cone	

Table 4.2: *Cuts performed on cone-jets to select lepton candidates.*

overall efficiency	
electrons	$\sim$80%
muons	$\sim$80%
1-prong taus	$\sim$87%
3-prong taus	$\sim$72%

Table 4.3: *Overall efficiencies for the selection of the different types of lepton candidates [58].*

well as generator information [61]. As already mentioned, for the analysis only the data of the lepton candidates is used. The cut-based analysis itself is performed by ROOT, an object-oriented data analysis framework [62]. The data, stored in the ntuple files is simply converted into a ROOT compatible file format, without losing information.

4.2 Simulation of Events

In this Section, the two studied channels are described in more detail together with the set of leptonic background processes. The basic conditions for all simulated events are shown in Tab. 4.4. An integrated luminosity of 500 fb^{-1} corresponds to a time of taking data of about 1

MSSM benchmark point:	**SPS1a**
center-of-mass energy:	**500 GeV**
integrated luminosity:	**500 fb^{-1}**
polarisation $\mathcal{P}_i$:	**0.0/0.0**
	0.0/0.8 and
	-0.6/0.8
ISR:	**taken into account**
beamstrahlung:	**taken into account**

Table 4.4: *Basic conditions for the simulation and analysis of events. The convention for the polarisation is given by:* $\mathcal{P}_i := (\mathrm{P}(e^+)/\mathrm{P}(e^-))$, *(*$i = 1, 2, 3$*).*

– 2 years. For the center-of-mass energy, 500 GeV is assumed. In Tab. 2.11 the cross-sections of the neutralino sector are given in relation to 100% polarisation of the particles, i.e. these numbers reflect the interaction of an e^+ and an e^- beam with 100% right- or left-handed polarisation. Technically, it is not possible to provide a beam with such 100% right- or left-handed particles (see Sec. 3.1). Therefore, the polarisation P is introduced, which is a property

of a whole ensemble of particles, e.g. a particle beam. It is defined in the following way:

$$\mathrm{P} := \mathrm{R} - \mathrm{L} \quad \text{and} \quad 1 = \mathrm{R} + \mathrm{L}, \tag{4.1}$$

where R and L denote the fraction of right- and left-handed particles in the ensemble. This means, it is possible to write:

$$\mathrm{P} = \frac{\mathrm{R} - \mathrm{L}}{\mathrm{R} + \mathrm{L}}. \tag{4.2}$$

From simple arithmetics, the following equations for R and L can be found:

$$\mathrm{R} = \frac{1 + \mathrm{P}}{2} \quad \text{and} \quad \mathrm{L} = \frac{1 - \mathrm{P}}{2}. \tag{4.3}$$

In Tab 4.6 the commonly used polarisation values are displayed.

The polarsation can be independently chosen for electrons and positrons. This means, for

P	R	L
1.000	1.000	0.000
0.800	0.900	0.100
0.600	0.800	0.200
0.000	0.500	0.500
-0.600	0.200	0.800
-0.800	0.100	0.900
-1.000	0.000	1.000

Table 4.5: *Commonly used polarisation values.*

a collider experiment with a beam[2] of electrons and positrons two polarisations, R- and L-fractions have to be taken into account. For the calculations the following conventions are used:

$$\mathrm{P}_1 := \mathrm{P}(\mathrm{e}^+), \quad \mathrm{P}_2 := \mathrm{P}(\mathrm{e}^-), \tag{4.4}$$

$$\mathrm{R}_1 := \mathrm{R}(\mathrm{e}^+), \quad \mathrm{R}_2 := \mathrm{R}(\mathrm{e}^-), \tag{4.5}$$

$$\mathrm{L}_1 := \mathrm{L}(\mathrm{e}^+), \quad \mathrm{L}_2 := \mathrm{L}(\mathrm{e}^-). \tag{4.6}$$

The production cross-section as a function of the two polarisations can be written as the composition of all possible combinations of the two beam polarisations:

$$\sigma_{\mathrm{tot}}^{\mathrm{pol}} \;=\; \mathrm{R}_1 \cdot \mathrm{R}_2 \cdot \sigma_{\mathrm{RR}} \;+\; \mathrm{R}_1 \cdot \mathrm{L}_2 \cdot \sigma_{\mathrm{RL}} \;+\; \mathrm{L}_1 \cdot \mathrm{R}_2 \cdot \sigma_{\mathrm{LR}} \;+\; \mathrm{L}_1 \cdot \mathrm{L}_2 \cdot \sigma_{\mathrm{LL}}. \tag{4.7}$$

The cross-sections σ_i, with $i = \mathrm{RR}, \mathrm{RL}, \mathrm{LR}, \mathrm{LL}$, are the basis cross-sections, as mentioned in Tab.2.11, 4.10 and 4.11. Together with Eq. (4.3) the total polarised cross-section can be derived from:

$$\begin{aligned} \sigma_{\mathrm{tot}}^{\mathrm{pol}} \;=\; & (\tfrac{1+\mathrm{P}_1}{2}) \cdot (\tfrac{1+\mathrm{P}_2}{2}) \cdot \sigma_{\mathrm{RR}} \;+ \\ & (\tfrac{1+\mathrm{P}_1}{2}) \cdot (\tfrac{1-\mathrm{P}_2}{2}) \cdot \sigma_{\mathrm{RL}} \;+ \\ & (\tfrac{1-\mathrm{P}_1}{2}) \cdot (\tfrac{1+\mathrm{P}_2}{2}) \cdot \sigma_{\mathrm{LR}} \;+ \\ & (\tfrac{1-\mathrm{P}_1}{2}) \cdot (\tfrac{1-\mathrm{P}_2}{2}) \cdot \sigma_{\mathrm{LL}} \;. \end{aligned} \tag{4.8}$$

[2] In this case each beam is an ensemble of electrons or positrons.

In this thesis, three polarisation combinations are used, which are listed in Tab 4.6. The most desirable combination for the signal is $P_1 = -0.6$ and $P_2 = 0.8$. This means, that the signal cross-section is enhanced and most background cross-sections are suppressed in this case (see Tab. 4.10 and 4.11 as well as Chapter 5). In both described signal channels, an associated

	P_1	P_2
$\mathcal{P}_1$	0.0	0.0
$\mathcal{P}_2$	0.0	0.8
$\mathcal{P}_3$	-0.6	0.8

Table 4.6: *Polarisation combinations used in this thesis. The definition of* P_1 *and* P_2 *can be found in Eq. (4.5).*

production of the heavy neutralino $\tilde{\chi}_3^0$ together with a $\tilde{\chi}_1^0$ is studied, i.e. $e^+e^- \rightarrow \tilde{\chi}_1^0\tilde{\chi}_3^0$ (see Sec. 2.5). The $\tilde{\chi}_1^0$ is the LSP in the chosen parameter set of this model and, due to R-parity conservation, it is stable. For the $\tilde{\chi}_3^0$ two different decays via a Z boson are studied, which are described in the following two Subsections. The dominant decay of the $\tilde{\chi}_3^0$ is to a W boson, although this is not considered further, because it seems not possible to keep the background processes under control[3] (see Sec. 2.5 and Tab. 2.10). The generation of signal events is done for all final states ($e^+e^- \rightarrow \tilde{\chi}_1^0\tilde{\chi}_3^0 \rightarrow$ all). Apart from the studied channels, the decays of the $\tilde{\chi}_3^0$ are treated as background processes. The $\tilde{\chi}_1^0$ is stable. The properties of the two studied decay chains are presented in the Tables 4.7 and 4.8. Finally, the whole set of simulated Monte Carlo background is described in the last Section of this Chapter.

4.2.1 The Channel $\tilde{\chi}_3^0 \rightarrow \tilde{\chi}_1^0 Z^0$

In this channel the $\tilde{\chi}_3^0$ decays into a $\tilde{\chi}_1^0$ an a Z^0 boson. For the Z^0 only a decay into electrons and muons is taken into account (see Fig. 2.10 (a) and Tab. 4.7). This offers a very clean final state, where it is possible to reconstruct the four momentum of the Z^0. Although, it should be noted, that due to the small BR of $\sim 6.7\%$, only a relatively low statistic is available[4]. Allowing hadronic decays of the Z^0 does not solve this problem, because many additional hadronic backgrounds would need to be taken into account. By assuming a fixed center-of-mass energy of 500 GeV, knowing the mass of the $\tilde{\chi}_1^0$, e.g. due to a previous measurement at the ILC, and implying four momentum conservation, it is possible to reconstruct the process completely. Therefore, it would be possible to determine the mass of the $\tilde{\chi}_3^0$ by the kinematical limits of the energy distribution of the final state leptons. For a more detailed description of this method see [41]. Moreover, in the cut-based analysis it is possible to perform a cut on the invariant mass of the two-lepton system, i.e. the Z^0 mass, to suppress backgrounds. On the other hand, the overall cross-section $\sigma \cdot BR_1 \cdot BR_2$ is rather small for this specific channel (see Tab. 4.7).

The main problem in this channel, is the fight against backgrounds, due to the small cross-sections. In Fig. 4.2 an event display of this process is given. The two electrons, leaving their energy in the ECAL, are clearly visible, as well as the missing energy due to the two $\tilde{\chi}_1^0$. This leads to a large number of SM and SUSY background processes with a similar final state topology, e.g. double Z or double W production in SM and slepton pair production in SUSY processes (see Sec. 4.2.3 and Chapter 5).

[3] due to the missing invariant mass cut (see Chapter 5)

[4] The Z^0 has a branching ratio (BR) of $\sim$3.36% for decays into electrons or muons each [11].

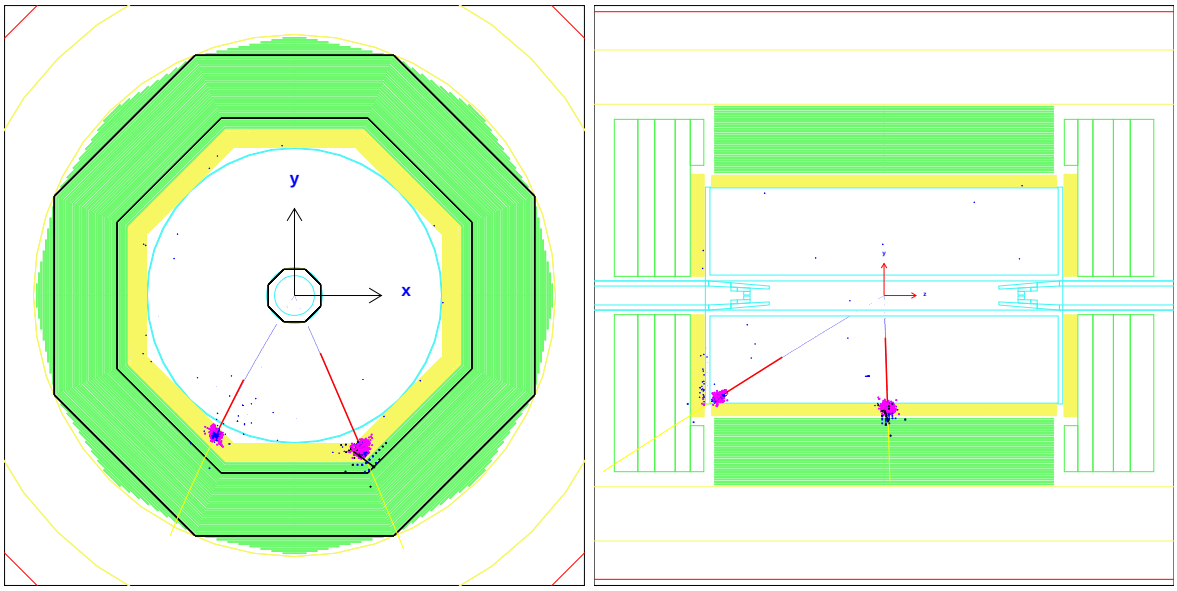

Figure 4.2: *Event display of the process* $\tilde{\chi}_3^0 \rightarrow \tilde{\chi}_1^0 Z^0$*, where the* Z^0 *decays into two electrons. The figure on the left hand side shows the xy-projection, the figure on the right hand side the yz-projection of the event in the detector. The reconstructed tracks of the electrons (blue lines) in the TPC are clearly visible. The red lines indicate the direction of the reconstructed momentum of the electrons entering the calorimeter. The deposited energy in the calorimeter is shown by magenta- (ECAL) and blue-colored boxes (HCAL). The vector addition of the momenta of the two electrons does not cancel out. The reason for this is the missing energy due to the two* $\tilde{\chi}_1^0$*, which are not detected. For more information about the detector see Fig 3.3. The event display is created with BRAHMS [47].*

$e^+e^- \rightarrow \tilde{\chi}_1^0\tilde{\chi}_3^0$						
P		σ_{tot}	BR_1	BR_2	$\sigma_{\text{tot}} \cdot BR_1 \cdot BR_2$	N_{exp}
e^+	e^-	in fb	$\tilde{\chi}_3^0 \rightarrow \tilde{\chi}_1^0 Z^0$	$Z^0 \rightarrow e^\pm e^\mp$, $\mu^\pm\mu^\mp$	in ab	
0.0	0.0	7.22	11.27%	6.73%	54.8	∼27
0.0	0.8	12.91	11.27%	6.73%	97.9	∼49
-0.6	0.8	20.64	11.27%	6.73%	155.9	∼78

Table 4.7: *Cross-sections and BRs for the channel* $\tilde{\chi}_3^0 \rightarrow \tilde{\chi}_1^0 Z^0$ *(see Tab. 2.8 as well). The* $\tilde{\chi}_1^0$ *is the LSP in the chosen parameter set of this model and due to R-parity conservation it is stable. The number of expected events* N_{exp} *is simply calculated by* $N_{exp} = \sigma_{\text{tot}} \cdot BR_1 \cdot BR_2 \cdot L$*. The center-of-mass energy is set to 500 GeV and the luminosity* L *is assumed to be 500* fb^{-1}*.*

4.2.2 The Channel $\tilde{\chi}_3^0 \rightarrow \tilde{\chi}_2^0 Z^0$

This channel is a little more complicated. It shows a longer decay chain due to the decay of the $\tilde{\chi}_2^0$ (see Fig. 2.10 (b) and Tab. 4.8). In the final state again two stable $\tilde{\chi}_1^0$ appear, which are the reason for missing energy. Due to the longer decay chain and therefore more vertices, it is even more difficult to measure the mass of the $\tilde{\chi}_3^0$. On the other hand, there are not so many background processes, because in the case of the SM, four lepton final states are less common (see Sec. 4.2.3 and Chapter 5). Moreover, SUSY backgrounds can be suppressed more

easily and the partial cross-section is larger (see Tab. 4.8). Finally, the number of expected

$e^+e^- \to \tilde{\chi}_1^0\tilde{\chi}_3^0$							
P		σ_{tot}	BR_1	BR_2	BR_3	$\sigma_{\text{tot}} \cdot BR_n$	N_{exp}
e^+	e^-	in fb	$\tilde{\chi}_3^0 \to \tilde{\chi}_2^0 Z^0$	$\tilde{\chi}_2^0 \to \tilde{l}_1^{\pm} l^{\mp}$	$Z^0 \to e^{\pm}e^{\mp}$, $\mu^{\pm}\mu^{\mp}$	in ab	
0.0	0.0	7.22	20.99%	99.56	6.73%	101.5	∼51
0.0	0.8	12.91	20.99%	99.56	6.73%	181.6	∼91
-0.6	0.8	20.64	20.99%	99.56	6.73%	290.3	∼145

Table 4.8: *Cross-sections and BRs for the channel $\tilde{\chi}_3^0 \to \tilde{\chi}_2^0 Z^0$ (see Tab. 2.8 as well). The $\tilde{\chi}_1^0$ is the LSP in the chosen parameter set of this model and due to R-parity conservation it is stable. The number of expected events N_{exp} is again simply calculated by $N_{exp} = \sigma_{\text{tot}} \cdot BR_n$, where BR_n is defined by $BR_n := BR_1 \cdot BR_2 \cdot BR_3$. The center-of-mass energy is set to 500 GeV and the luminosity L is assumed to be 500 fb^{-1}. The slepton $\tilde{l}_1^{\pm}$ decays into its corresponding lepton and a $\tilde{\chi}_1^0$ with 100% BR.*

events in this channel is approximately twice as large as in the channel $\tilde{\chi}_3^0 \to \tilde{\chi}_1^0 Z^0$. The main branch of the sleptonic decay of $\tilde{\chi}_2^0 \to \tilde{l}_1^{\pm} l^{\mp}$ is $\tilde{\chi}_2^0 \to \tilde{\tau}^{\pm}\tau^{\mp}$ with a BR of 85.98 %. Therefore, the cut-based analysis in this channel should allow for the selection of topologies as it is illustrated in Fig. 4.3. Fig. 4.4 shows an event display of this process with a electron pair coming from

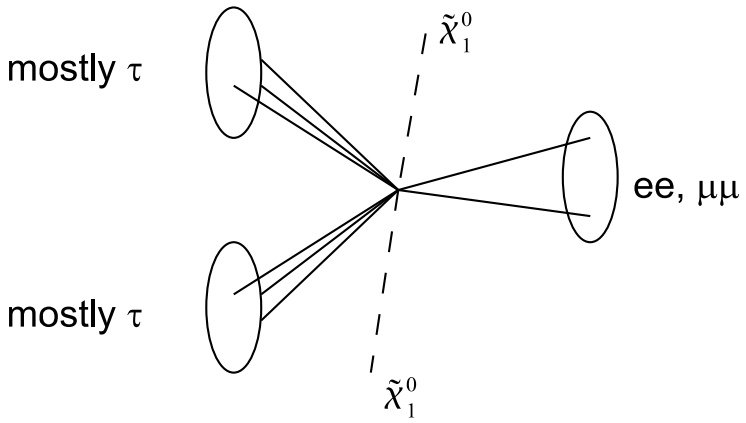

Figure 4.3: *Illustration of the topology in the final state of the channel $\tilde{\chi}_3^0 \to \tilde{\chi}_2^0 Z^0$. It shows four fermions, where two of them are a pair of electrons or muons, which reconstruct a Z^0, and two are taus (∼86 % BR).*

the Z^0 and two taus. In the yz-projection on the right side the missing energy due to the two $\tilde{\chi}_1^0$ is obvious.

4.2.3 The Set of Simulated Events

The set of simulated events consists of all relevant contributions from SM and SUSY processes to final states with up to six lepton candidates. Before the ntuples are created, several pre-cuts are performed on the output data from SIMDET (see Sec. 4.1 and Fig. 4.1). This is a pre-selection, mainly to suppress $\gamma\gamma$-background and to sort out purely hadronic processes.

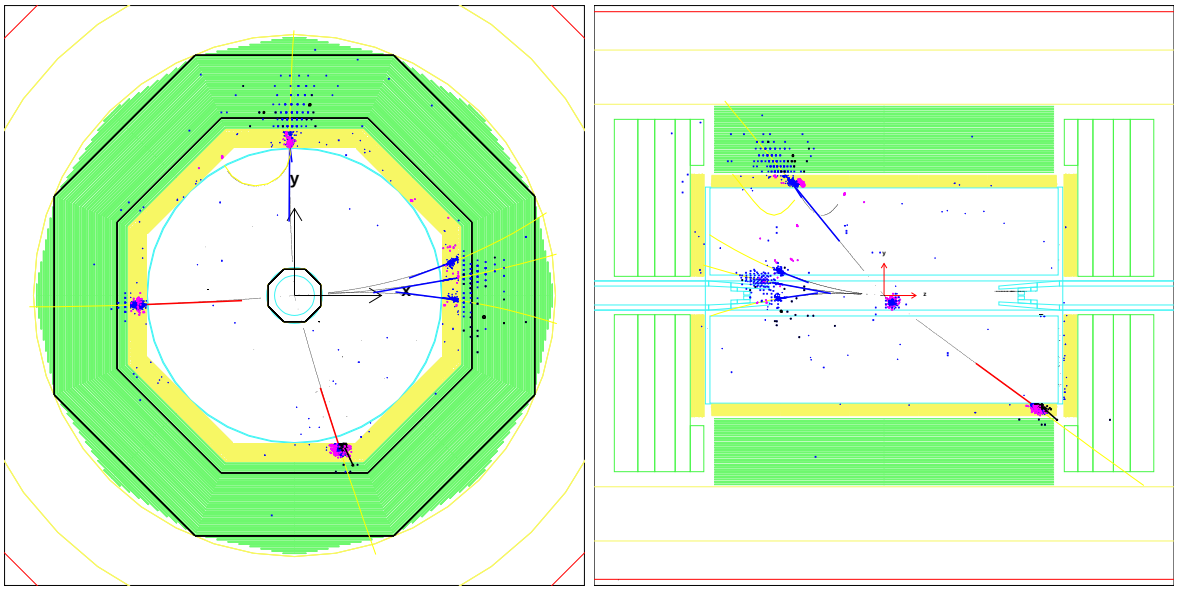

Figure 4.4: *Event display of the process* $\tilde{\chi}_3^0 \rightarrow \tilde{\chi}_2^0 \mathrm{Z}^0$, *where the* Z^0 *decays into two electrons and the* $\tilde{\chi}_2^0$ *decays into two taus (see Fig. 4.3 as well). The figure on the left hand side shows the xy-projection, the figure on the right hand side the yz-projection of the event in the detector. The reconstructed tracks of the particles (black lines) in the TPC are clearly visible. The red and blue lines indicate the direction of the reconstructed momentum of the particles entering the calorimeter. The deposited energy in the calorimeter is shown by magenta- (ECAL) and blue-colored boxes (HCAL). In the yz-projection on the right side the missing energy due to the two* $\tilde{\chi}_1^0$ *is obvious. For more information about the detector see Fig 3.3. The event display is created with BRAHMS [47].*

Notice, that this selection is not associated with the pre-cuts mentioned in Sec. 5.1 and 5.2. The cuts of the pre-selection are listed in Tab. 4.9. The pre-selection consists of five cuts. The first cut only accepts events with two to six lepton candidates. This is done, because neutralinos from the signal processes mainly decay into two or four leptons. In the second cut, an additional charged cone is allowed, which is not classified as a lepton candidate. This

cut on		name
number of lepton candidates	$1 \leq N_{\mathrm{cand}} \leq 6$	(0.1)
at most one additional charged cone	$N_{\mathrm{cand}} + 1 \geq N_{\mathrm{char.cone}}$	(0.2)
energy of lepton candidate	$E_{\mathrm{cand}} > 4.5 \cdot e^{\,0.45 \cdot \eta^2}$ GeV	(0.3)
energy of neutral cones	$E_{\mathrm{neutral}} < 150$ GeV	(0.4)
cut on $\alpha_{r\phi}^{\mathrm{max}}$ in rϕ-plane	$\cos(\alpha_{r\phi}^{\mathrm{max}}) < -0.99$	(0.5)

Table 4.9: *Pre-selection performed during simulation on all data samples. The second cut is done in connection to the number of lepton candidates, i.e. at most one more charged cone compared to the number of lepton candidates is allowed. The cut on the energy of lepton candidate is done as a function of the pseudo-rapidity* η *[58]. The last cut is performed on the maximal angle between two lepton candidates in the* rϕ*-plane. The cut-flow tables for the whole analysis can be found in the appendix (see Tab. A.1 to A.3 and A.4 to A.8 as well).*

ensures, that also events, where one τ-lepton was not identified, pass the pre-selection. The cut on the lepton candidate energy is performed to suppress $\gamma\gamma$-background [58]. Moreover, the neutral energy is restricted to 150 GeV. The last cut ensures that in the rϕ-plane no lepton candidate pair has a "back-to-back" orientation. This pre-selection is done for all simulated data, meaning that from this point an access to the full data set is no longer possible. In Tab. 4.10 and Tab. 4.11 the processes covered by the set of simulated events are listed [27].

Unfortunately, not all processes are generated for all polarisations (R_1R_2, R_1L_2, L_1R_2, and L_1L_2). Moreover, of the polarisations which are simulated, they are produced in varying statistics. Nevertheless, for all polarised processes, at least the statistic of 1500 fb^{-1} is available. This corresponds to a statistic of 6000 fb^{-1} for unpolarised beams, if all four polarisations are taken into account. The processes, which are produced unpolarised, are available in different statistics, but for all processes at least 500 fb^{-1} is available. For the analysis these processes are scaled according their polarised cross-sections. Generally, the processes are normalised to a luminosity of 500 fb^{-1} for the selection presented in the next chapter.

SUSY											
	$e_1^+ e_2^- \rightarrow$	f.s.	σ_{tot} in fb				number of events generated				remarks
			R_1R_2	R_1L_2	L_1R_2	L_1L_2	R_1R_2	R_1L_2	L_1R_2	L_1L_2	
signal	$\tilde{\chi}_1^0\tilde{\chi}_3^0$	all	0.00	0.23	28.67	0.00	0	10k	50k	0	
neutralino BG	$\tilde{\chi}_1^0\tilde{\chi}_2^0$	all	0.00	232.12	22.37	0.00	0	350k	50k	0	
	$\tilde{\chi}_1^0\tilde{\chi}_4^0$	all	0.00	0.78	2.81	0.00	0	10k	10k	0	
	$\tilde{\chi}_2^0\tilde{\chi}_2^0$	all	0.00	243.53	0.08	0.00	0	400k	10k	0	
chargino BG	$\tilde{\chi}_1^+\tilde{\chi}_1^-$	all	0.00	571.88	0.81	0.00	0	1000k	10k	0	
slepton BG	$\tilde{e}_1^+\tilde{e}_1^-$	all	0.00	43.81	1098.16	0.00	0	100k	1800k	0	
	$\tilde{e}_{1/2}^+\tilde{e}_{2/1}^-$	all	314.67	0.00	0.00	314.67	500k	0	0	500k	
	$\tilde{e}_2^+\tilde{e}_2^-$	all	0.00	159.48	12.32	0.00	0	250k	20k	0	
	$\tilde{\mu}_1^+\tilde{\mu}_1^-$	all	0.00	43.86	185.53	0.00	0	100k	300k	0	
	$\tilde{\mu}_2^+\tilde{\mu}_2^-$	all	0.00	60.85	12.32	0.00	0	100k	100k	0	
	$\tilde{\tau}_1^+\tilde{\tau}_1^-$	all	0.00	57.34	191.31	0.00	0	100k	300k	0	
	$\tilde{\tau}_{1/2}^+\tilde{\tau}_{2/1}^-$	all	0.00	5.45	4.05	0.00	0	10k	10k	0	
	$\tilde{\tau}_2^+\tilde{\tau}_2^-$	all	0.00	49.32	12.47	0.00	0	100k	20k	0	
sneutrino BG	$\tilde{\nu}_e\tilde{\nu}_e$	all	406.50				2450k				non pol.
	$\tilde{\nu}_\mu\tilde{\nu}_\mu$	all	12.70				80k				non pol.
	$\tilde{\nu}_\tau\tilde{\nu}_\tau$	all	13.00				80k				non pol.

Table 4.10: *SUSY contribution to two and four lepton final states. All cross-sections for the basis polarisations* R_1R_2, R_1L_2, L_1R_2, *and* L_1L_2 *are listed (see Sec. 4.2). Processes, which are produced non-polarised are listed with their non-polarised cross-section. For the selection these cross-sections are weighted according to their polarised cross-sections. Additionally, the number of generated events is listed. The processes are related to the background categories, which are used in the selection. The SUSY background is composed of chargino, slepton and sneutrino background, whereas the neutralino background is treated separately (see Chapter 5). The abbreviation "f.s." indicates final state [27].*

SM												
	$e_1^+e_2^- \rightarrow$	f.s.	σ_{tot} in fb				number of events generated				remarks
			R_1R_2	R_1L_2	L_1R_2	L_1L_2	R_1R_2	R_1L_2	L_1R_2	L_1L_2	
$\gamma\gamma$ BG	$\gamma\gamma$	ll	$13.77 \cdot 10^6$				105M				non pol.
	$\gamma\gamma$	qq	$5.84 \cdot 10^6$				65M				non pol.
	$\gamma\gamma$	WW	240.10				125k				non pol.
$\gamma Z, hZ$ BG	γZ	ll	3882.00				2100k				non pol.
	γZ	qq	13510.00				7000k				non pol.
	hZ	all	70.00				250k				non pol.
Zee BG	Zee	llee	5921.00				3000k				non pol.
	Zee	$\nu\nu$ee	2453.00				1250k				non pol.
	Zee	qqee	14530.00				7500k				non pol.
$\nu\nu Z$ BG	$\nu\nu Z$	$\nu\nu$ee	0.00	35.54	0.00	0.00	0	20k	0	0	
	$\nu\nu Z$	$\nu\nu\mu\mu$	0.00	35.57	0.00	0.00	0	20k	0	0	
	$\nu\nu Z$	$\nu\nu\tau\tau$	0.00	35.62	0.00	0.00	0	20k	0	0	
Z-pair BG	ZZ	llll	13.72				10k				non pol.
	ZZ	ll$\nu\nu$	33.42				20k				non pol.
	ZZ	qqll	292.40				150k				non pol.
	ZZ	qqqq	314.60				160k				non pol.
W-pair BG	WW	lνlν	0.00	4070.00	16.81	0.00	0	2100k	10k	0	
	WW	qqlν	0.00	16980.00	68.38	0.00	0	4500k	35k	0	
	WW	qqqq	0.00	17900.00	73.59	0.00	0	7000k	37k	0	
	WW/ZZ	eeh	120.95				1200k				non pol.
Weν BG	Weν	lνeν	2049.50				1200k				non pol.
	Weν	qqeν	4266.40				2200k				non pol.

Table 4.11: *SM contribution to two and four lepton final states. For the processes, which are produced polarised, the basis polarisations* R_1R_2, R_1L_2, L_1R_2, *and* L_1L_2 *are listed (see Sec. 4.2). The other Processes are shown with their non-polarised cross-section. For the selection these cross-sections are weighted according to their polarised cross-sections. Additionally, the number of generated events is listed. The processes are related to the background categories, which are used in the selection. The category of SM background contains all the processes listed here (see Chapter 5). The abbreviation "f.s." indicates final state [27].*

Chapter 5

The Selection

In this chapter the search for heavy neutralinos $\tilde{\chi}_3^0$ originating from an associated production together with a $\tilde{\chi}_1^0$ is described. In both channels it is a challenge to find appropriate cut variables to suppress the overwhelming backgrounds with high production rates and similar final states compared to the associated production of a heavy $\tilde{\chi}_3^0$ (see cross-sections in Tab. 4.11 and 4.10). The most delicate backgrounds are slepton pair production in the case of SUSY processes and Z pair production for the SM backgrounds. On the other hand, this production mechanism is the only way to "access" a $\tilde{\chi}_3^0$ at the ILC. The properties of the two studied channels are illustrated in more detail in Sec. 4.2. In both channels an analysis of the simulated data is performed in a cut-based way. In such kind of selections, cuts on several variables are performed, e.g. invariant mass of two leptons in the final state, which exclude a certain range of the variable distribution with the aim of enriching the fraction of signal events compared to all events passing the cut-based selection. To do this in an effective way the chosen distributions should differ as much as possible between signal and background. The selections for the two studied channels are described in the following two sections, where all histograms and numbers are normalised to a integrated luminosity of 500 fb^{-1}. Generally, the histograms are plotted as stacked histograms, i.e. all different distributions are added up. At the end of the chapter a brief interpretation of the results is given.

5.1 Analysis of the Channel $\tilde{\chi}_3^0 \to \tilde{\chi}_1^0 \text{Z}^0$

The final state in this channel consists of two single leptons, which can be reconstructed to a Z boson, and missing energy due to the $\tilde{\chi}_1^0$ (see Fig. 4.2). The generated sample of signal events contains all final states, this means: $\text{e}^+\text{e}^- \to \tilde{\chi}_1^0\tilde{\chi}_3^0 \to$ all. The cut-based analysis of this channel is optimised to select only the events, where the $\tilde{\chi}_3^0 \to \tilde{\chi}_1^0\text{Z}^0$ and the Z decays into electrons or muons. Therefore, the remaining decays of the $\tilde{\chi}_3^0$ are treated as background processes. More information about this channel is given in Sec. 4.2.1. The selection is done for the three polarsation combinations mentioned in Tab. 4.6. All histograms are given for $\text{P}(\text{e}^+) = -0.6$ and $\text{P}(\text{e}^-) = 0.8$. The cut-flow table show the results for all three polarsation combinations.

The cut-based selection of the generated data samples is divided into two parts. First a set of pre-cuts is applied with the goal of suppressing as much background as possible and therefore reducing the amount of data, in order to make it more easy to tune the cuts in the main selection. These pre-cuts are performed after the pre-selection, which is done during the simulation of events (see Sec. 4.2.3).

The Pre-Cuts

The following list describes the pre-cuts, which are performed one after each other on the set of simulated data. The data is sorted into the four categories SM background, SUSY background (except neutralinos), neutralino background and signal. The detailed list of generated processes can be found in Tables 4.11 and 4.10.

(1.1) The first pre-cut is performed on the number of lepton candidates. It is required to have only two lepton candidates in the final state:

$$\mathrm{N_{lcand}} = 2. \tag{5.1}$$

The corresponding histogram is plotted in Fig. 5.1 (a).

(1.2) After this a cut on the sum of charges is applied, which is demanded to be zero. Moreover, there is no net-charge in the initial state and therefore there should not be any in the final state due to the conservation of charge. Reason for a non-zero measured charge in the final state are particles, which cannot be reconstructed. Therefore, the following equation holds:

$$\sum_{i=1}^{2} \mathrm{Q_{lcand}} = 0, \tag{5.2}$$

where the charge of the lepton candidates is given in multiples of the elementary charge (see Fig. 5.1 (b)).

(1.3) The next pre-cut is performed on the number of charged cones, which are found by the "cone-jet-algorithm" (see Sec. 4.1). This number should be equal to the number of lepton candidates, i.e. two, otherwise additional charged cones would occur in the detector, which are not identified by the "lepton candidate algorithm" as leptons (see Sec. 4.1). This would make it more complicated to reconstruct the Z boson. The corresponding distribution is shown in Fig. 5.1 (c)) and the cut condition can be written as:

$$\mathrm{N_{char}^{cone}} = 2. \tag{5.3}$$

(1.4) This pre-cut asks for the number of electrons or muons. More precisely speaking this means, it is required, that the two lepton candidates either are identified as electrons or muons. Hadronic decays of the Z and decays into tau leptons are not taken into account, just to obtain a clean final state. The exact cut-condition is:

$$\mathrm{N_{lcand}^{e}} = 2 \quad \vee \quad \mathrm{N_{lcand}^{\mu}} = 2. \tag{5.4}$$

The two corresponding histograms are given in Fig. 5.2 (d) and (e).

(1.5) The last pre-cut is performed on the invariant mass of the two leptons in the final state. Moreover, only events are accepted, where one lepton and one anti-lepton are present, i.e. $\mathrm{e^{\pm}e^{\mp}}$ or $\mu^{\pm}\mu^{\mp}$. The cut limits are given by a range of ± 5 GeV around the Z mass, which is assumed to be $m_{\mathrm{Z}} = 91.19$ GeV. The limit of 5 GeV roughly corresponds to a distance of $2{\cdot}\Gamma_{\mathrm{Z}}$ around the Z resonance. Therefore, the following equation holds:

$$|m_{\mathrm{inv}}^{\mathrm{e^{\pm}e^{\mp}},\mu^{\pm}\mu^{\mp}} - m_{\mathrm{Z}}| < 5\ GeV. \tag{5.5}$$

This cut is illustrated in Fig. 5.2 (f).

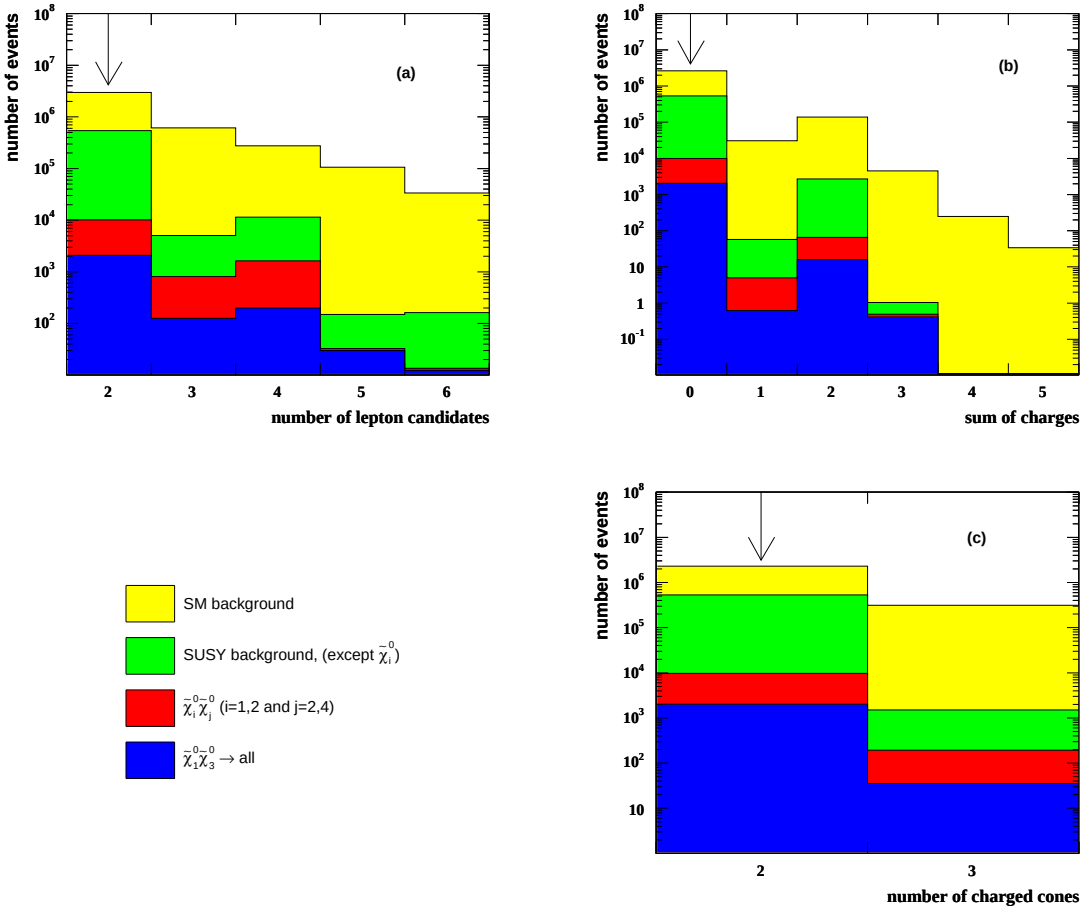

Figure 5.1: *Histograms for the pre-cuts (1.1) to (1.3). These show the distributions for the pre-cut variables for a polarisation of* $P(e^+) = -0.6$ *and* $P(e^-) = 0.8$ *before the cut is applied. The corresponding cut-flow table with the results for the three studied polarisations is given in Tab. 5.2. More detailed cut-flow tables, corresponding to the background categories mentioned in Sec. 4.2.3, can be found in the appendix (see Tab. A.1 to Tab. A.3). All histograms are given for an integrated luminosity of 500* fb^{-1} *and a center-of-mass energy of 500 GeV. The arrows indicate the bins which are accepted.*

All events passing these criteria are accepted and are handed over to the the main selection (see next subsection). The histograms shown in Fig. 5.1 and 5.2, are for the polarisation $P(e^+) = -0.6$, $P(e^-) = 0.8$. It is the best choice for the signal within the technical limits, i.e. the mean ration of signal cross-section to the accumulated background cross-section is increased (see cross-sections in Tab. 4.11 and 4.10). In Tab. 5.2 the whole cut-flow, including the pre-cut-flow, is given.

The Main Cuts

The main selection consists of three single cuts and is performed after the pre-cuts. The following list gives a more detailed description of the cut variables as well as their limits. For each cut distribution the corresponding "$(n-1)$-cut" histogram is plotted. These histograms contain the data, which has passed all other cuts except the observed one. Therefore, they

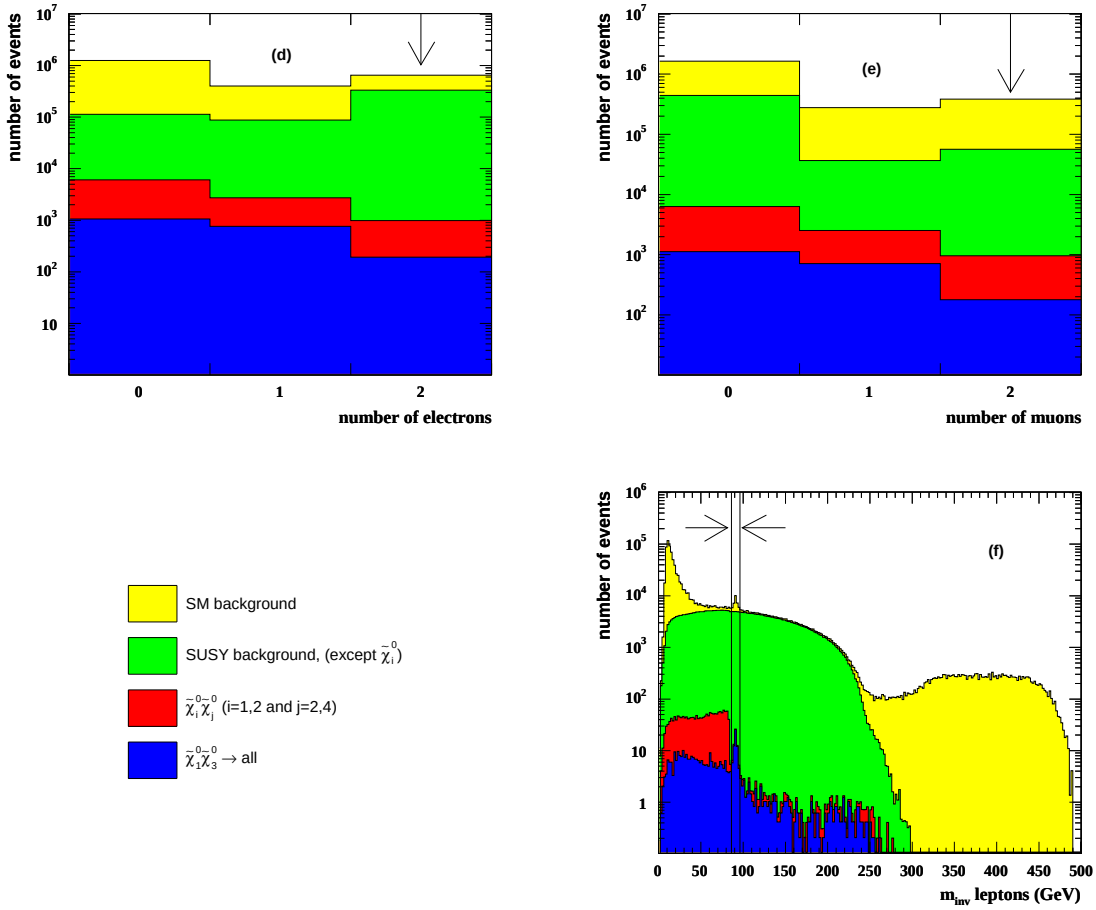

Figure 5.2: *Histograms for the pre-cuts (1.4) and (1.5). These show the distributions for the pre-cut variables for a polarisation of* $\mathrm{P}(\mathrm{e}^+)=-0.6$ *and* $\mathrm{P}(\mathrm{e}^-)=0.8$ *before the cut is applied. The corresponding cut-flow table with the results for the three studied polarisations is given in Tab. 5.2. More detailed cut-flow tables, corresponding to the background categories mentioned in Sec. 4.2.3, can be found in the appendix (see Tab. A.1 to Tab. A.3). All histograms are given for an integrated luminosity of 500* fb^{-1} *and a center-of-mass energy of 500 GeV. The arrows indicate the bins which are accepted.*

show how effective the current cut would be, if it would be applied in addition.

(2.1) The first cut variable is the polar angle θ_Z of the reconstructed Z, i.e. the angle between three-momentum of the Z and the z-axis of the coordinate system, which is the beam axis. Therefore, the Z boson needs to be reconstructed. This is simply done by adding the four-momenta of the two leptons in the final state (four-momentum conservation is assumed). The cut limits are given by:

$$|\cos(\theta_\mathrm{Z})| < 0.7. \tag{5.6}$$

The distribution of this variable is plotted in Fig. 5.3 (a), and Fig. 5.3 (b) shows the corresponding $(\mathrm{n}-1)$-plot.

(2.2) The next cut is performed on the recoil mass of the reconstructed Z. This is a reasonable cut variable, because the Z is recoiling against a relatively heavy $\tilde{\chi}_1^0$ (see Tab. 2.9). The

energy and momentum of the Z is reconstructed by the following relations:

$$E_Z = E_{l_1} + E_{l_2}, \quad \vec{p}_Z = \vec{p}_{l_1} + \vec{p}_{l_2}. \tag{5.7}$$

The recoil mass then can be calculated by:

$$(m^{ll}_{recoil})^2 := (\sqrt{s} - E_Z)^2 - \vec{p}_Z^{\,2}, \tag{5.8}$$

where $\sqrt{s}$ is set to 500 GeV. The cut limits are given by:

$$200\text{GeV} < m^{ll}_{recoil} < 330\text{GeV}. \tag{5.9}$$

The histograms for the recoil mass are shown in Fig. 5.3 (c) and (d).

(2.3) The last cut acts on the normalised energy difference of the two leptons in the final state. This variable is defined as the difference in energy between the negative charged lepton and the positive normalised to the sum of the lepton energy:

$$\Delta E_{leptons} := \frac{E_{l^-} - E_{l^+}}{E_{l^-} + E_{l^+}}. \tag{5.10}$$

The cut limits are given by:

$$|\Delta E_{leptons}| < 0.7. \tag{5.11}$$

Figures 5.3 (e) and (f) illustrate the distributions for this cut variable.

The cut-flow table is presented in Tab. 5.2. For each category of processes in these tables the three polarisations $\mathcal{P}_i := (P(e^+)/P(e^-))$, $(i = 1, 2, 3)$ with $\mathcal{P}_1 = (0.0/0.0)$, $\mathcal{P}_2 = (0.0/0.8)$ and $\mathcal{P}_3 = (-0.6/0.8)$ are listed. All numbers are calculated concerning an integrated luminosity of 500 fb^{-1}. "Event fractions" smaller than 0.1 per 500 fb^{-1} are denoted by ~ 0.0. The table 5.2 offers an overview of the selection with the categories of backgrounds as in the corresponding histograms (see Fig. 5.1, 5.2 and 5.3 and for the definition of the categories Tab. 4.10 and 4.11). More detailed cut-flow tables can be found in the appendix (see Tab. A.1 to Tab. A.3). This allows those backgrounds, which "survive" the cuts to be examined. The main background contribution after the selection originates from selectron and smuon production (see Tab. A.2) and from SM backgrounds containing Z bosons (see Tab. A.3). Even for the most adequate polarisation $\mathcal{P}_3$, the background processes are overwhelming the signal in this channel to the extend, that there is no chance to determine the mass of the $\tilde{\chi}^0_3$ by the kinematic limits of the energy distribution of the final state leptons, assuming a known mass of the $\tilde{\chi}^0_1$ (see Sec. 4.2.1).

The significance of an observed excess of events over the expectation from known background processes is defined as

$$S := \frac{N^{sig}}{\sqrt{\sum_{i=1}^{n} N_i^{BG}}}, \tag{5.12}$$

in limit of large N^{BG}. In this equation N^{sig} indicates the number of signal events and N_i^{BG} the number of background events after the selection. The index of the sum i is running over all backgrounds. Moreover, the efficiency and the purity of the cut-based analysis can be calculated. The purity is defined as the fraction of signal events N^{sig} compared to all events passing the cuts:

$$P := \frac{N^{sig}}{N^{sig} + \sum_{i=1}^{n} N_i^{BG}}. \tag{5.13}$$

The efficiency on the other hand is given by the fraction of signal events passing the selection N^{sig} from the number of originally generated signal events N^{sig}_{gen}:

$$\epsilon := \frac{N^{sig}}{N^{sig}_{gen}}. \tag{5.14}$$

The generation of $e^+_1 e^-_2 \to \tilde{\chi}^0_1 \tilde{\chi}^0_3$ events is done for all final states, i.e. for all decays of the $\tilde{\chi}^0_3$ (see Sec. 4.2.3). For the calculation of the efficiency only the actual number of events of this particular decay is taken into account. All other decays are treated as background processes. The results of the selection for the different polarisations are presented in Tab. 5.1. Together with an efficiency, calculated as given above, it is possible to estimate the partial cross-section σ_{part} of the process $\tilde{\chi}^0_3 \to \tilde{\chi}^0_1 Z^0$, where the Z is decaying either into electron or muons pairs. This is done by use of the following equation:

$$\sigma_{part} = \frac{N^{sig}}{\epsilon \cdot L} = \frac{N^{tot} - N^{BG}}{\epsilon \cdot L}, \tag{5.15}$$

where N^{sig} is the number of selected signal events, N^{tot} is the total number of events after all cuts, N^{BG} is the number background events, ϵ denotes the efficiency and L is the integrated luminosity, which is set to 500 fb^{-1}. The relative statistical error on the partial cross-section is given by:

$$\Delta\sigma_{part} := \frac{\delta\sigma_{part}}{\sigma_{part}} = \frac{\sqrt{N^{tot}}}{N^{sig}}. \tag{5.16}$$

	$\mathcal{P}_1$	$\mathcal{P}_2$	$\mathcal{P}_3$
N^{sig}	10.8	19.4	31.0
N^{BG}	1713.2	811.5	649.1
P	0.6%	2.3%	4.6%
ϵ	40.3%	38.9%	38.8%
S	0.26	0.68	1.22
σ_{part} in ab	53.7	99.5	159.6
$\Delta\sigma_{part}$	383.2%	148.8%	84.2%

Table 5.1: *Results of the presented cut-based analysis of the decay* $\tilde{\chi}^0_3 \to \tilde{\chi}^0_1 Z^0$. *The results are given for the three polarisations* $\mathcal{P}_i := (P(e^+)/P(e^-))$, *(*$i = 1, 2, 3$*) with* $\mathcal{P}_1 = (0.0/0.0)$, $\mathcal{P}_2 = (0.0/0.8)$ *and* $\mathcal{P}_3 = (-0.6/0.8)$. *All numbers are given for an integrated luminosity of 500* fb^{-1} *and a center-of-mass energy of 500 GeV. For the error* $\Delta\sigma_{part}$ *on the partial cross-section* σ_{part} *only statistical errors are taken into account, where* $\Delta\sigma_{part}$ *is defined by:* $\Delta\sigma_{part} := \delta\sigma_{part}/\sigma_{part}$. *For the definition of the variables shown in the table see Sec. 5.1.*

The results for the three different polarisations are listed in Tab. 5.1. For the error on the partial cross-section $\Delta\sigma_{part}$ only statistical errors are taken into account. Although the presented cut-based selection hardly cuts into the signal (signal efficiency of approx. 40%), a tremendous number of background events survive. This leads to a low purity of at most a few percent and a significance of 0.26 for a polarisation $\mathcal{P}_1 = (0.0/0.0)$ and 1.22 for a polarisation $\mathcal{P}_3 = (-0.6/0.8)$. An estimate on the partial cross-section of this process can only be given with a accuracy from approx. 80% to 400%. Therefore, it is not possible to obtain more information about the properties of the $\tilde{\chi}^0_3$ in any of the presented polarisations with the cuts mentioned above. An overview and a brief discussion of the results and errors are presented in Sec. 5.3.

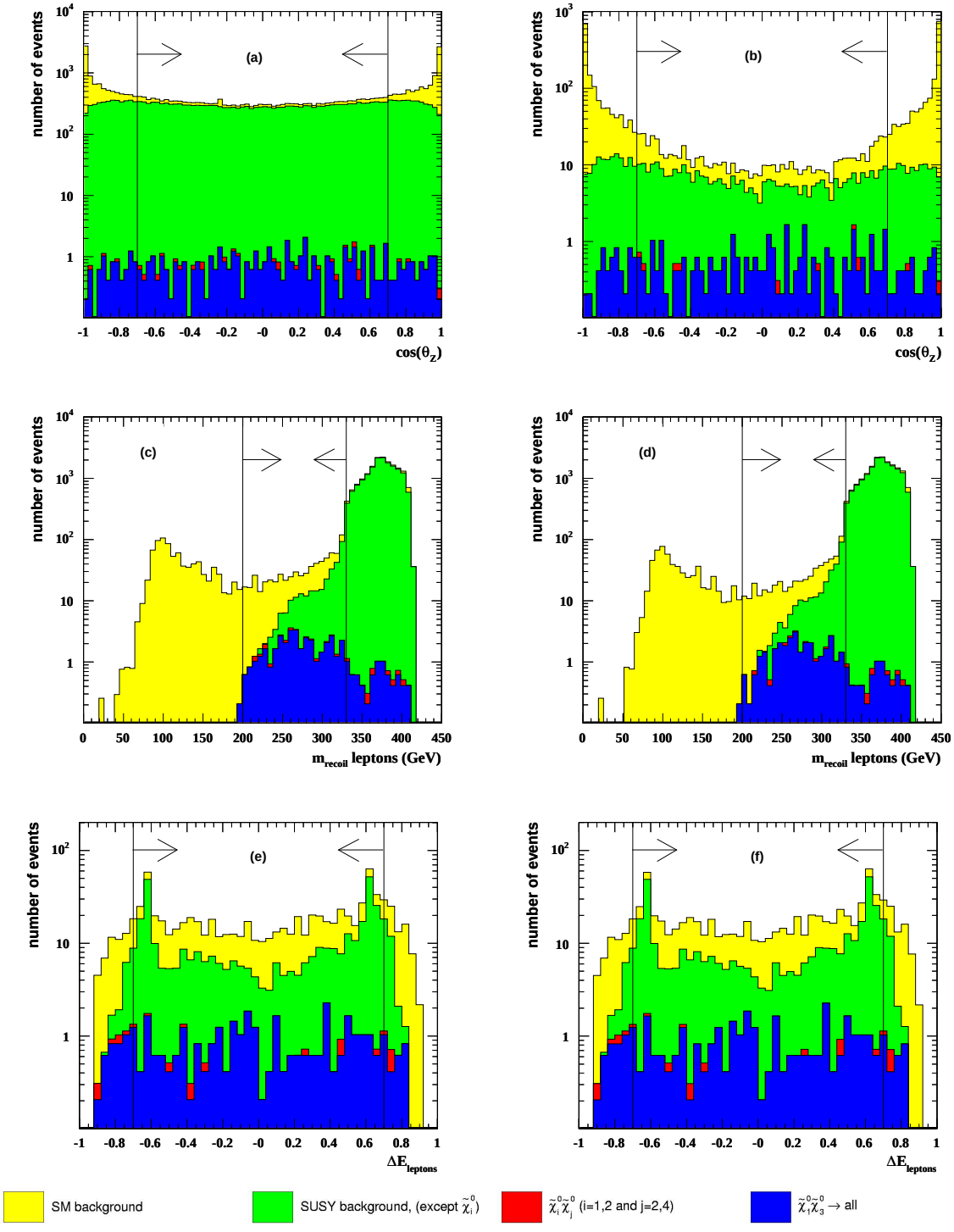

Figure 5.3: *Histograms for the cuts (2.1) to (2.3). On the left hand side ((a), (c) and (e)) the distributions for the pre-cut variables for a polarisation of* $\mathrm{P}(\mathrm{e}^+) = -0.6$ *and* $\mathrm{P}(\mathrm{e}^-) = 0.8$ *are shown, before the cut is applied. On the right hand side ((b), (d) and (f)) the corresponding* $(\mathrm{n}-1)$*-histograms are given. The corresponding cut-flow table with the results for the three studied polarisations is given in Tab. 5.2. More detailed cut-flow tables, corresponding to the background categories mentioned in Sec. 4.2.3, can be found in the appendix (see Tab. A.1 to Tab. A.3). All histograms are given for an integrated luminosity of 500* fb^{-1} *and a center-of-mass energy of 500 GeV. The arrows indicate the bins which are accepted.*

cuts	signal ($\tilde{\chi}_1^0\tilde{\chi}_3^0 \to$ all)			neutralinos			SUSY background			SM background		
	$\mathcal{P}_1$	$\mathcal{P}_2$	$\mathcal{P}_3$	$\mathcal{P}_1$	$\mathcal{P}_2$	$\mathcal{P}_3$	$\mathcal{P}_1$	$\mathcal{P}_2$	$\mathcal{P}_3$	$\mathcal{P}_1$	$\mathcal{P}_2$	$\mathcal{P}_3$
(0.0)	3612.3	6455.7	10322.1	62711.9	17593.8	13856.9	608443.3	820771.6	$\sim 1.2 \cdot 10^6$	$\sim 10 \cdot 10^9$	$\sim 10 \cdot 10^9$	$\sim 10 \cdot 10^9$
(0.5)	858.0	1533.5	2451.9	51938.3	13821.5	10164.2	326063.5	396049.7	545567.5	3558995.2	3321906.0	3439195.5
(1.1)	723.1	1292.2	2066.1	25666.5	8520.9	7981.6	301884.0	376519.0	528636.1	2401300.5	2216268.0	2255878.8
(1.2)	717.1	1281.6	2049.1	25239.5	8423.9	7927.2	300080.2	374350.1	525962.5	2244166.0	2063911.8	2085666.2
(1.3)	704.9	1259.6	2014.0	23399.4	8049.8	7769.3	298265.0	372854.1	524650.5	1935183.6	1766642.8	1772960.4
(1.4)	130.0	232.3	371.4	4703.2	1626.3	1576.1	181475.4	268837.6	388612.9	696296.2	638225.5	642892.8
(1.5)	21.1	37.7	60.3	2.0	2.3	3.5	11216.6	16900.6	24524.8	17325.2	9726.8	11556.1
(2.1)	15.6	27.9	44.6	1.7	1.9	2.8	7703.7	11514.9	16700.2	5885.3	2057.8	1931.2
(2.2)	13.0	23.2	37.2	0.9	1.3	2.0	596.6	503.1	369.8	1537.4	473.2	405.9
(2.3)	10.8	19.4	31.0	0.4	0.7	1.0	532.8	448.8	338.8	1179.9	362.0	309.2

Table 5.2: *Cut-flow table for the analysis of $\tilde{\chi}_3^0 \to \tilde{\chi}_1^0 \mathrm{Z}^0$, corresponding to the pre-cuts and cuts mentioned in (1.1) to (1.5) and (2.1) to (2.3). The lines (0.0) and (0.5) contain the number of events before pre-selection during the simulation of events and after (see Tab. 4.9). The table shows the accumulated numbers for the three categories mentioned in the histograms (see Fig. 5.1, 5.2, and 5.3 and for the definition of the categories Tab. 4.10 and 4.11). More detailed cut-flow tables can be found in the appendix (see Tab. A.1 to Tab. A.3). For each category the three polarisations $\mathcal{P}_i := (\mathrm{P}(\mathrm{e}^+)/\mathrm{P}(\mathrm{e}^-))$, $(i = 1, 2, 3)$ with $\mathcal{P}_1 = (0.0/0.0)$, $\mathcal{P}_2 = (0.0/0.8)$ and $\mathcal{P}_3 = (-0.6/0.8)$ are listed. All numbers are given for an integrated luminosity of 500 fb^{-1} and a center-of-mass energy of 500 GeV.*

5.2 Analysis of the Channel $\tilde{\chi}_3^0 \rightarrow \tilde{\chi}_2^0 Z^0$

The final state in this channel is more complicated compared to the process $\tilde{\chi}_3^0 \rightarrow \tilde{\chi}_1^0 Z^0$, described in the last section. It contains four leptons, where two of them are originating from the Z decay, and two are produced by the decay of the $\tilde{\chi}_2^0$. Moreover, the missing energy is caused by the two $\tilde{\chi}_1^0$, which cannot be detected. The generated sample of signal events contains all final states, this means: $e^+e^- \rightarrow \tilde{\chi}_1^0\tilde{\chi}_3^0 \rightarrow$ all. The cut-based analysis of this channel is optimised to select only the events, where the $\tilde{\chi}_3^0 \rightarrow \tilde{\chi}_2^0 Z^0$ and the Z decays into electrons or muons. Therefore, the remaining decays of the $\tilde{\chi}_3^0$ are treated as background processes. More information about this channel is given in Sec. 4.2.2, and a event display can be found in Fig. 4.4. The selection is done for the three polarsation combinations mentioned in Tab. 4.6. All histograms are given for $P(e^+) = -0.6$ and $P(e^-) = 0.8$. The cut-flow table show the results for all three polarsation combinations.

The selection of the generated data samples is performed in the same way as in Sec. 5.1, i.e. first of all a set of pre-cuts is applied, and after this, the events, which passed the pre-cuts are selected by a sequence of main cuts. These pre-cuts are performed after the pre-selections during the simulation of events are applied (see Sec. 4.2.3).

The Pre-Cuts

The following list shows the set of pre-cuts, which is applied one after each other on the set of simulated data. The data is sorted into four categories SM background, SUSY background, neutralino background and signal. The detailed list of generated processes can be found in Tables 4.11 and 4.10.

(1.1) Again the first pre-cut is performed on the number of lepton candidates, where in this channel it is required to have four lepton candidates in the final state:

$$N_{\text{lcand}} = 4. \tag{5.17}$$

The corresponding histogram is plotted in Fig. 5.4 (a).

(1.2) After that a cut on the sum of charges is applied. Due to the neutral initial state and due to the conservation of charge, the charge in the final state should be zero. Reasons for a non-zero measured charge in the final state are particles, which cannot be detected. Therefore, the following equation holds:

$$\sum_{i=1}^{2} Q_{\text{lcand}} = 0, \tag{5.18}$$

where the charge of the lepton candidates is given in multiples of the elementary charge (see Fig. 5.4 (b)).

(1.3) The next pre-cut is performed on the number of charged cones, which are found by the "cone-jet-algorithm" (see Sec. 4.1). This number should be equal to the number of lepton candidates, i.e. four, because otherwise additional charged cones would occur in the detector, which are not identified by the "lepton candidate algorithm" as leptons (see Sec. 4.1). It would lead to a more complex final state, where it is more difficult to reconstruct the Z from two of the four leptons in the final state. The corresponding distribution is shown in Fig. 5.4 (c)) and the cut condition can be written as:

$$N_{\text{char}}^{\text{cone}} = 4. \tag{5.19}$$

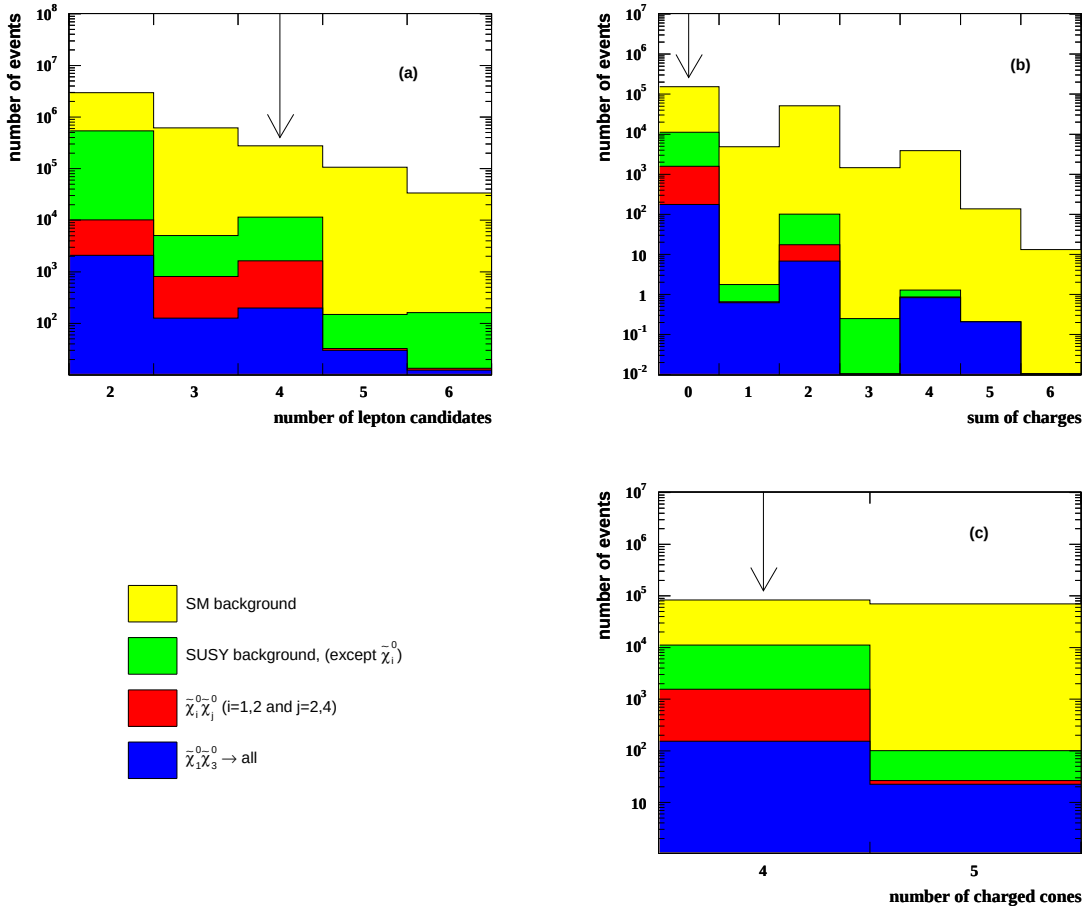

Figure 5.4: *Histograms for the pre-cuts (1.1) to (1.3). These show the distributions for the pre-cut variables for a polarisation of* $\mathrm{P}(\mathrm{e}^+)=-0.6$ *and* $\mathrm{P}(\mathrm{e}^-)=0.8$ *before the cut is applied. The corresponding cut-flow table with the results for the three studied polarisations is given in Tab. 5.4. More detailed cut-flow tables, corresponding to the background categories mentioned in Sec. 4.2.3, can be found in the appendix (see Tab. A.4 to Tab. A.8). All histograms are given for an integrated luminosity of 500* fb^{-1} *and a center-of-mass energy of 500 GeV. The arrows indicate the bins which are accepted.*

(1.4) For a clean reconstruction of the Z boson at least two electrons or two muons are needed. This is ensured by the following cut. Hadronic decays of the Z and decays into tau leptons are not taken into account. The concrete cut-condition is:

$$\mathrm{N}^{\mathrm{e}}_{\mathrm{lcand}} \geq 2 \quad \vee \quad \mathrm{N}^{\mu}_{\mathrm{lcand}} \geq 2. \tag{5.20}$$

The two corresponding histograms are shown in Fig. 5.5 (d) and (e).

(1.5) The last cut is again performed on the invariant mass of two leptons in the final state. Due to the fact that there are four leptons in the final state, the situation is more complex. Therefore, all possible combinations of electron- and muon-pairs in the final state are determined. After this for each pair the invariant mass is calculated and the pair with the smallest energy difference to the Z mass is selected. After this, a cut on the invariant mass of this pair is performed. The cut limits are given by a range of ± 5

GeV around the Z mass, which is assumed to be $m_Z = 91.19$ GeV. The limit of 5 GeV roughly corresponds to a distance of $2{\cdot}\Gamma_Z$ around the Z resonance. If the invariant mass is located in this range, the event is accepted, otherwise it is rejected. The cut condition can be written as:

$$|m_{\mathrm{inv}(1)}^{\mathrm{e}^\pm\mathrm{e}^\mp,\mu^\pm\mu^\mp} - m_Z| < 5\ GeV. \tag{5.21}$$

The distributions for this cut variable are illustrated in Fig. 5.5 (f). Additionally a veto-cut on the invariant mass of the other two leptons is performed. That means, an event is rejected, if the remaining lepton-pair is either an electron- or muon-pair and if its invariant mass is located in a range of 5 GeV around the Z resonance. This cut condition can be written as:

$$86.19\ GeV \geq m_{\mathrm{inv}(2)}^{\mathrm{e}^\pm\mathrm{e}^\mp,\mu^\pm\mu^\mp} \geq 96.19\ GeV, \tag{5.22}$$

where now the four-momenta of two remaining leptons are used. This veto-cut is mainly meant to suppress Z-pair background from processes $ZZ \rightarrow llll$. It does not influence signal much, because the $\tilde{\chi}_3^0$ is mainly decaying into two taus and two $\tilde{\chi}_1^0$ (see Sec. 4.2.2). The histograms of the veto-cut is shown in Fig. 5.5 (g).

After this pre-selection the main selection is performed, which consists of five additional cuts (see next subsection). The histograms for the pre-cuts, given in Figures 5.4 and 5.5, show the polarisation $P(e^+) = -0.6$, $P(e^-) = 0.8$ as an example. It is the optimal choice for the signal within the technical limits, i.e. the mean ration of signal cross-section compared to the accumulated background cross-section is increased (see cross-sections in Tab. 4.11 and 4.10). In Tables A.4 to A.6 the whole cut-flow, including the pre-cut-flow, is given.

The main Cuts

In the main selection five additional cut are applied. The following list gives a more detailed description of the cut variables as well as their limits. For each cut distribution the corresponding "(n − 1)-cut" histogram is plotted (see Sec. 5.1 as well).

(2.1) The first cut variable is the polar angle θ_p of the missing momentum. The missing momentum is given by:

$$\sum_{i=1}^{4} \vec{p}_i + \vec{p}_{\mathrm{miss}} := \vec{0}, \tag{5.23}$$

where the $\vec{p}_i$ $(i = 1, 2, 3)$ are the three-momenta of the leptons found in the final state. The polar angle of $\vec{p}_{\mathrm{miss}}$ is the angle between the beam-axis and $\vec{p}_{\mathrm{miss}}$ itself. The cut limits are given by:

$$|\cos(\theta_{\vec{p}_{\mathrm{miss}}})| < 0.95. \tag{5.24}$$

The distribution of this variable is plotted in Fig. 5.6 (a), and Fig. 5.6 (b) shows the corresponding (n − 1)-plot.

(2.2) The next cut is performed on the energy of the reconstructed Z boson. The energy of the Z is given by the sum of the energy of the two leptons, which are produced by the Z (see pre-cut (1.5)). The cut limits are given by

$$125\ \mathrm{GeV} < E_Z < 175\ \mathrm{GeV} \tag{5.25}$$

and the histograms are shown in Fig. 5.6 (c) and Fig. 5.6 (d). The distributions show a good separation between remaining SUSY and SM background.

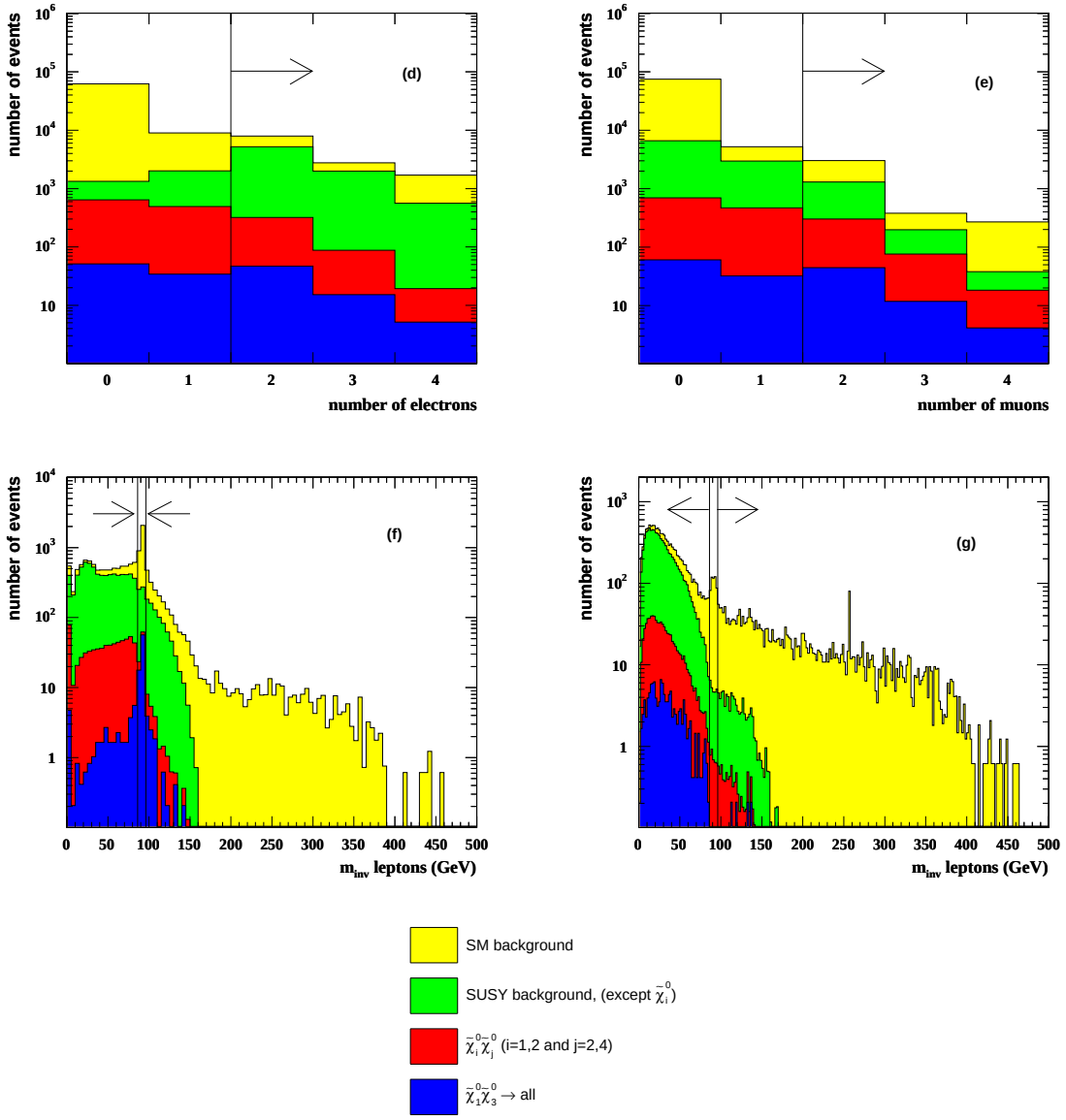

Figure 5.5: *Histograms for the pre-cuts (1.4) and (1.5). These show the distributions for the pre-cut variables for a polarisation of* $P(e^+) = -0.6$ *and* $P(e^-) = 0.8$ *before the cut is applied. The corresponding cut-flow table with the results for the three studied polarisations is given in Tab. 5.4. More detailed cut-flow tables, corresponding to the background categories mentioned in Sec. 4.2.3, can be found in the appendix (see Tab. A.4 to Tab.* **??***). All histograms are given for an integrated luminosity of 500* fb^{-1} *and a center-of-mass energy of 500 GeV. The arrows indicate the bins which are accepted.*

(2.3) For this cut it is necessary to count the number of electrons N_e and muons N_μ in the final state. The cut itself is performed on the variable $\text{Max}(N_e, N_\mu)$, which simply represents the larger of these two numbers. The cut limits are given by the following relation:

$$\text{Max}(N_e, N_\mu) \leq 3. \tag{5.26}$$

(2.4) The fourth cut of the main cut sequence is performed on the invariant mass of the two leptons, which are identified as not originating from the Z decay (see pre-cut (1.5)). The invariant mass of these leptons is shown in Fig. 5.7 (g) and the corresponding (n−1)-plot is given in Fig. 5.7 (h). The cut limit is defined by:

$$m_{\mathrm{inv}(2)} < 80\mathrm{GeV}. \tag{5.27}$$

For the definition of $m_{\mathrm{inv}(2)}$ see pre-cut (1.5).

(2.5) The last cut acts on the normalised energy difference of the two leptons, which are reconstructed to the Z. The definition of this "relative energy difference" $\Delta\mathrm{E}_{\mathrm{leptons}}$ can be found in the description of cut (2.3) in Sec. 5.1. The cut limits are given by:

$$|\Delta\mathrm{E}_{\mathrm{leptons}}| < 0.35. \tag{5.28}$$

Figures 5.7 (i) and (j) show the histograms for this cut variable.

The cut-flow table for this selection is presented in Tab. 5.4. For each category of processes in these tables the three polarisations $\mathcal{P}_i := (\mathrm{P}(\mathrm{e}^+)/\mathrm{P}(\mathrm{e}^-))$, $(i = 1, 2, 3)$ with $\mathcal{P}_1 = (0.0/0.0)$, $\mathcal{P}_2 = (0.0/0.8)$ and $\mathcal{P}_3 = (-0.6/0.8)$ are listed. All numbers are calculated concerning an integrated luminosity of 500 fb^{-1}. "Event fractions" smaller than 0.1 per 500 fb^{-1} are denoted by $\sim$0.0. The table 5.4 offers an overview of the selection with the categories of backgrounds as in the corresponding histograms (see Fig. 5.4, 5.5 and 5.6 as well as 5.7. The definition of these categories can be found in Tab. 4.10 and 4.11). More detailed cut-flow tables are listed in the appendix (see Tab. A.4 to Tab. A.8). This allows those backgrounds, which "survive" the cuts to be examined. The main background contribution after the selection originates from SM processes containing Z bosons (see Tab. A.7 and A.8), mainly $\mathrm{e}^+\mathrm{e}^- \to \mathrm{ZZ}, \gamma\mathrm{Z}, \mathrm{hZ}$. Nevertheless, the suppression of backgrounds is much more effective in this channel, which can be seen from the significance of the selection in this channel.

	$\mathcal{P}_1$	$\mathcal{P}_2$	$\mathcal{P}_3$
$\mathrm{N}^{\mathrm{sig}}$	10.1	18.1	28.9
N^{BG}	8.1	6.1	7.7
P	55.6%	74.9%	79.0%
ϵ	20.7%	20.0%	19.9%
S	3.56	7.35	10.44
σ_{part} in ab	97.7	180.8	290.0
$\Delta\sigma_{\mathrm{part}}$	42.2%	27.2%	20.9%

Table 5.3: *Results of the presented cut-based analysis of the decay* $\tilde{\chi}_3^0 \to \tilde{\chi}_2^0\mathrm{Z}^0$. *The results are given for the three polarisations* $\mathcal{P}_i := (\mathrm{P}(\mathrm{e}^+)/\mathrm{P}(\mathrm{e}^-))$, $(i = 1, 2, 3)$ *with* $\mathcal{P}_1 = (0.0/0.0)$, $\mathcal{P}_2 = (0.0/0.8)$ *and* $\mathcal{P}_3 = (-0.6/0.8)$. *All numbers are given for an integrated luminosity of 500* fb^{-1} *and a center-of-mass energy of 500 GeV. For the error* $\Delta\sigma_{\mathrm{part}}$ *on the partial cross-section* σ_{part} *only statistical errors are taken into account, where* $\Delta\sigma_{\mathrm{part}}$ *is defined by:* $\Delta\sigma_{\mathrm{part}} := \delta\sigma_{\mathrm{part}}/\sigma_{\mathrm{part}}$. *For the definition of the variables shown in the table see Sec. 5.1.*

The definition of significance, purity and efficiency can be found in Sec. 5.1. Together with the efficiency, it is possible to estimate the partial cross-section σ_{part} of the process $\tilde{\chi}_3^0 \to \tilde{\chi}_2^0\mathrm{Z}^0$, where the $\tilde{\chi}_2^0$ is mainly dacaying into two taus and two $\tilde{\chi}_1^0$ and the Z is decaying into electron or muons pairs (see Sec. 4.2.2). The results of the selection for the different polarisations are

presented in Tab. 5.3. For the error on the partial cross-section $\Delta\sigma_{\text{part}}$ only statistical errors are taken into account. The results of the selection in this channel are much better. With the presented cut-based analysis purities of approximately 55% to 80% are achieved. The efficiency reaches approximately 20%. This leads to to significances between 3.6 and 10.4; therefore, a discovery is possible for the two polarisations $\mathcal{P}_2$ and $\mathcal{P}_3$[1]. The determination of the partial cross-section can be done with an accuracy between 20% and 40%. Therefore, all derived quantities are still limited by statistical errors. A brief discussion of the results and errors is presented in Sec. 5.3.

[1] Conventionally, a discovery is claimed if the significance of an excess, S, is larger than 5.

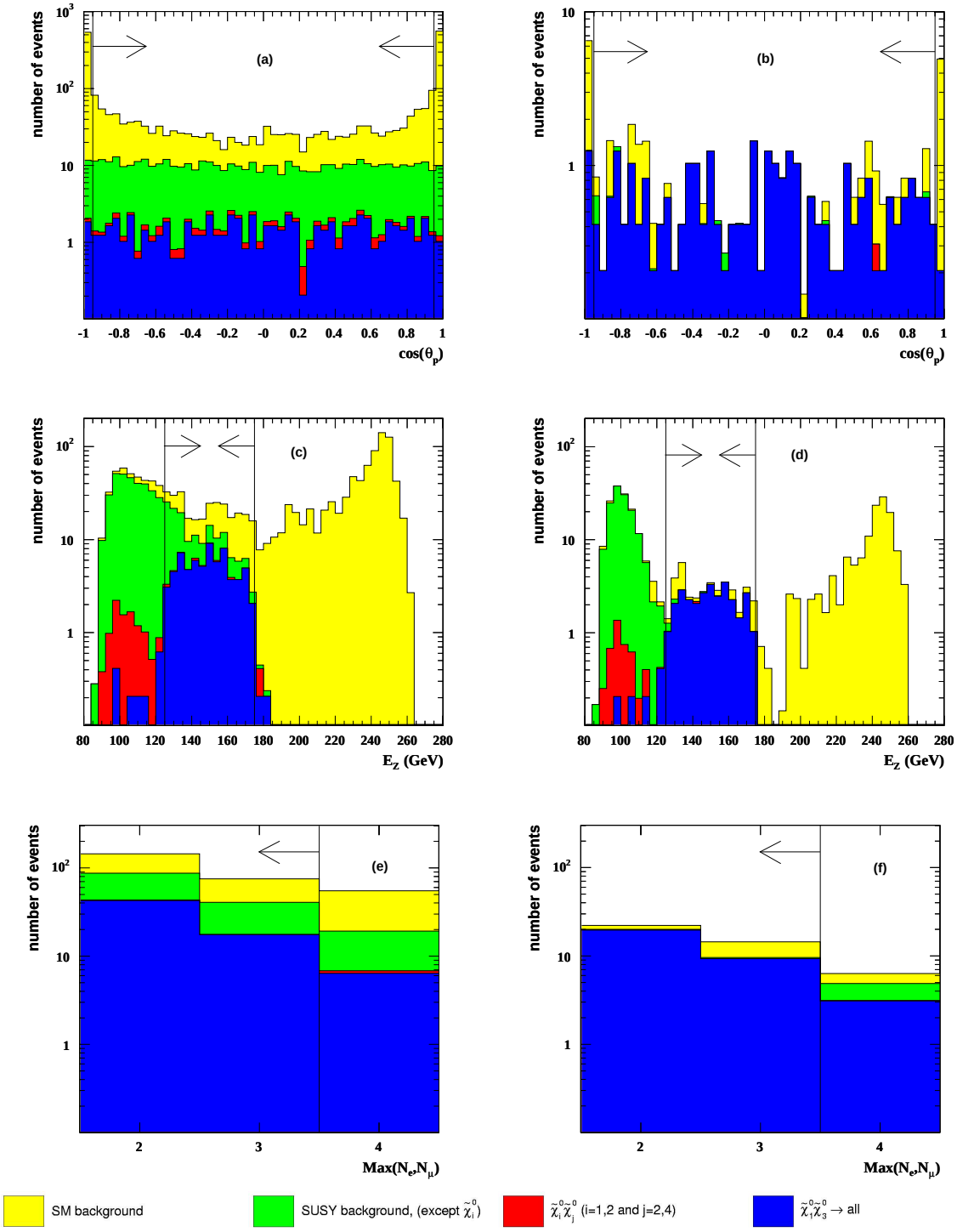

Figure 5.6: *Histograms for the cuts (2.1) to (2.3). On the left hand side ((a), (c) and (e)) the distributions for the pre-cut variables for a polarisation of* $\mathrm{P}(\mathrm{e}^+) = -0.6$ *and* $\mathrm{P}(\mathrm{e}^-) = 0.8$ *are shown, before the cut is applied. On the right hand side ((b), (d) and (f)) the corresponding* $(\mathrm{n}-1)$*-histograms are given. The corresponding cut-flow table with the results for the three studied polarisations is given in Tab. 5.4. More detailed cut-flow tables, corresponding to the background categories mentioned in Sec. 4.2.3, can be found in the appendix (see Tab. A.4 to Tab. A.8). All histograms are given for an integrated luminosity of 500* fb^{-1} *and a center-of-mass energy of 500 GeV. The arrows indicate the bins which are accepted.*

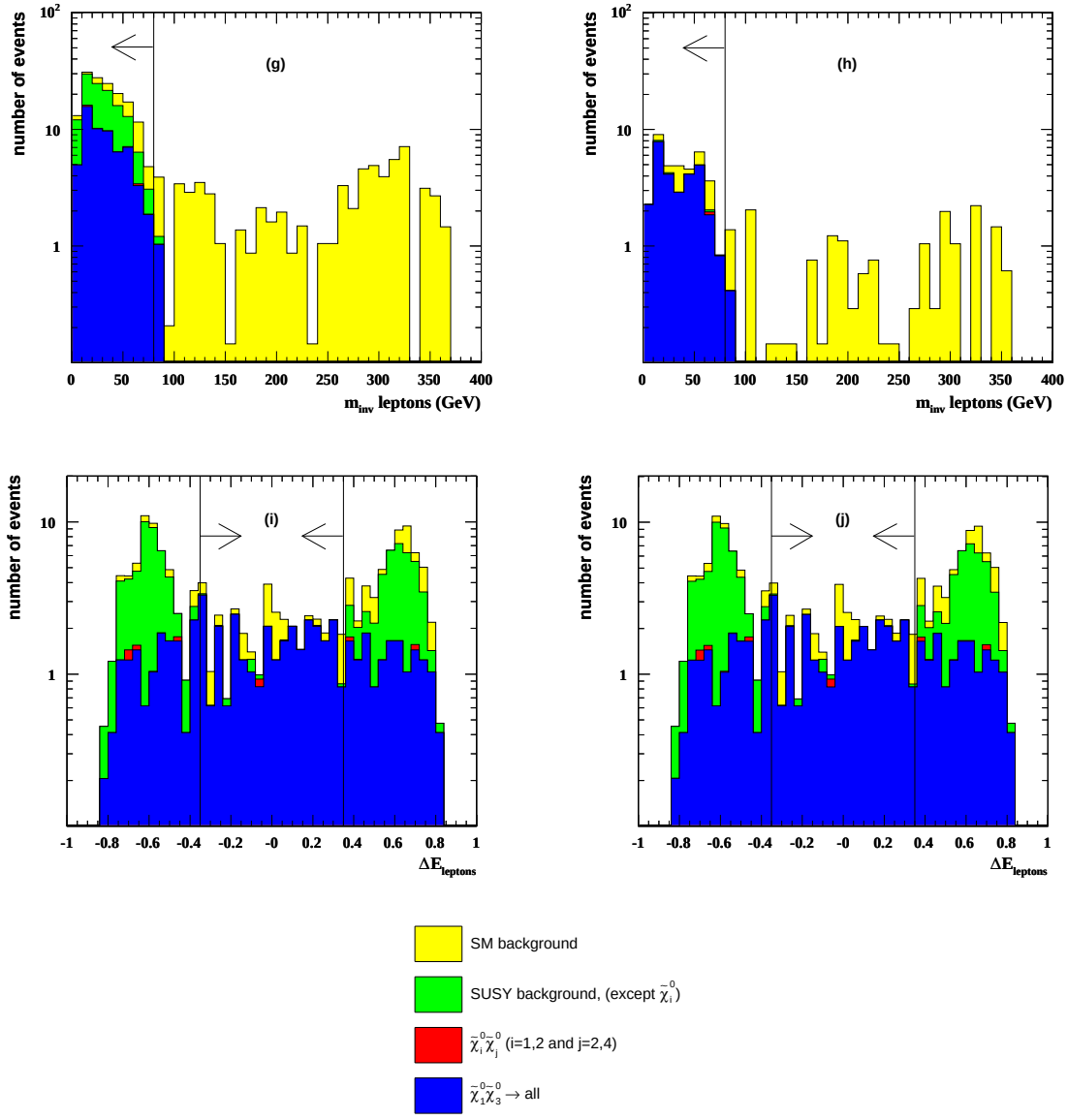

Figure 5.7: *Histograms for the cuts (2.4) to (2.5). On the left hand side ((g) and (i)) the distributions for the pre-cut variables for a polarisation of* $\mathrm{P}(\mathrm{e}^+) = -0.6$ *and* $\mathrm{P}(\mathrm{e}^-) = 0.8$ *are shown, before the cut is applied. On the right hand side ((h) and (j)) the corresponding* $(\mathrm{n}-1)$*-histograms are given. The corresponding cut-flow table with the results for the three studied polarisations is given in Tab. 5.4. More detailed cut-flow tables, corresponding to the background categories mentioned in Sec. 4.2.3, can be found in the appendix (see Tab. A.4 to Tab. A.8). All histograms are given for an integrated luminosity of 500* fb^{-1} *and a center-of-mass energy of 500 GeV. The arrows indicate the bins which are accepted.*

cuts	signal ($\tilde{\chi}_1^0\tilde{\chi}_3^0 \to$ all)			neutralinos			SUSY background			SM background		
	$\mathcal{P}_1$	$\mathcal{P}_2$	$\mathcal{P}_3$	$\mathcal{P}_1$	$\mathcal{P}_2$	$\mathcal{P}_3$	$\mathcal{P}_1$	$\mathcal{P}_2$	$\mathcal{P}_3$	$\mathcal{P}_1$	$\mathcal{P}_2$	$\mathcal{P}_3$
(0.0)	3612.3	6455.7	10322.1	62711.9	17593.8	13856.9	608443.3	820771.6	$\sim 1.2 \cdot 10^6$	$\sim 10 \cdot 10^9$	$\sim 10 \cdot 10^9$	$\sim 10 \cdot 10^9$
(0.5)	858.0	1533.5	2451.9	51938.3	13821.5	10164.2	326063.5	396049.7	545567.5	3558995.2	3321906.0	3439195.5
(1.1)	64.2	114.9	183.7	17405.8	3499.8	1425.0	14974.5	11922.0	9722.5	207809.7	196067.1	203912.0
(1.2)	61.3	109.6	175.3	17287.6	3475.5	1414.4	14806.6	11815.1	9637.0	145713.1	137693.5	142643.3
(1.3)	53.4	95.5	152.8	17256.0	3468.3	1410.5	14640.0	11740.2	9562.8	70294.0	69497.2	72594.8
(1.4)	40.8	73.1	116.8	8048.3	1618.2	658.8	12681.5	10449.5	7913.6	4376.1	3857.6	5467.6
(1.5)	25.8	46.1	73.7	117.3	24.2	10.8	957.3	733.2	425.8	1827.5	1491.5	2116.3
(2.1)	24.5	43.9	70.2	111.6	23.1	10.3	909.6	695.5	404.2	889.2	697.6	980.2
(2.2)	23.2	41.6	66.5	4.4	1.4	1.2	244.0	116.0	79.0	109.0	90.0	127.7
(2.3)	21.0	37.6	60.1	1.8	0.7	0.8	206.0	97.5	66.6	77.4	64.6	91.7
(2.4)	20.6	36.9	59.0	1.8	0.7	0.8	204.7	97.1	66.5	21.4	17.1	23.8
(2.5)	10.1	18.1	28.9	0.2	0.1	0.1	1.4	0.7	0.5	6.4	5.3	7.0

Table 5.4: *Cut-flow table for the analysis of $\tilde{\chi}_3^0 \to \tilde{\chi}_2^0 Z^0$, corresponding to the pre-cuts and cuts mentioned in (1.1) to (1.5) and (2.1) to (2.5). The lines (0.0) and (0.5) contain the number of events before pre-selection during the simulation of events and after (see Tab. 4.9). The table shows the accumulated numbers for the three categories mentioned in the histograms (see Fig. 5.4 and 5.5 as well as 5.6 and 5.7. For the definition of the categories see Tab. 4.10 and 4.11). More detailed cut-flow tables can be found in the appendix (see Tab. A.4 to Tab. A.8). For each category the three polarisations $\mathcal{P}_i := (\mathrm{P}(e^+)/\mathrm{P}(e^-))$, $(i = 1, 2, 3)$ with $\mathcal{P}_1 = (0.0/0.0)$, $\mathcal{P}_2 = (0.0/0.8)$ and $\mathcal{P}_3 = (-0.6/0.8)$ are listed. All numbers are given for an integrated luminosity of 500 fb^{-1} and a center-of-mass energy of 500 GeV.*

5.3 Interpretation of the Results

In Tab. 5.5 an overview of the results presented in Sec. 5.1 and 5.2 is given. The results of the cut-based analysis of channel $\tilde{\chi}_3^0 \to \tilde{\chi}_1^0 Z^0$ show, that it is not possible to obtain more information about the properties of the $\tilde{\chi}_3^0$ in any of the presented polarisations with the cuts mentioned in Sec. 5.1. The reason for this is the overwhelming background due to selectron and smuon production (see Tab. A.2) and due to SM backgrounds containing Z bosons (see Tab. A.3). This then leads to the significances of 0.26 to 1.22 and to errors on the determined partial cross-section of between 84% to 380%. This means it not possible to distinguish signal event from background.

In the second studied channel $\tilde{\chi}_3^0 \to \tilde{\chi}_2^0 Z^0$ the results are much better. For the polarisations $\mathcal{P}_2 = (0.0/0.8)$ and $\mathcal{P}_3 = (-0.6/0.8)$ a $5{\cdot}\sigma$-discovery is possible, assuming a integrated luminosity of 500 fb^{-1} and a center-of-mass energy of 500 GeV. The accuracy on the calculated partial cross-sections are of the order of 20% to 40%. The results are completely determined by statistical errors. The most important systematic errors originate from measurement of the center-of-mass energy and the luminosity, where the error on the luminosity would directly influence the determination of the cross-section (see Sec. 5.1). These errors are negligible compared to the statistical error.

	$\tilde{\chi}_3^0 \to \tilde{\chi}_1^0 Z^0$			$\tilde{\chi}_3^0 \to \tilde{\chi}_2^0 Z^0$		
	$\mathcal{P}_1$	$\mathcal{P}_2$	$\mathcal{P}_3$	$\mathcal{P}_1$	$\mathcal{P}_2$	$\mathcal{P}_3$
N^{sig}	10.8	19.4	31.0	10.1	18.1	28.9
N^{BG}	1713.2	811.5	649.1	8.1	6.1	7.7
S	0.26	0.68	1.22	3.56	7.35	10.44
σ_{part} in ab	53.7	99.5	159.6	97.7	180.8	290.0
$\Delta\sigma_{part}$	383.2%	148.8%	84.2%	42.2%	27.2%	20.9%
σ_{part}^{exp} in ab	54.8	97.9	155.9	101.5	181.6	290.3

Table 5.5: Summary of the results of the selection in the two decays of the $\tilde{\chi}_3^0$ presented in Sec. 5.1 and 5.2. The results are given for the three polarisations $\mathcal{P}_i := (P(e^+)/P(e^-))$, $(i = 1, 2, 3)$ with $\mathcal{P}_1 = (0.0/0.0)$, $\mathcal{P}_2 = (0.0/0.8)$ and $\mathcal{P}_3 = (-0.6/0.8)$. For the error $\Delta\sigma_{part}$ on the partial cross-section σ_{part} only statistical errors are taken into account, where $\Delta\sigma_{part}$ is defined by: $\Delta\sigma_{part} := \delta\sigma_{part}/\sigma_{part}$. The expected partial cross-sections σ_{part}^{exp} are taken from Tab. 4.7 and 4.8. All numbers are given for an integrated luminosity of 500 fb^{-1} and a center-of-mass energy of 500 GeV. For the definition of the variables shown in the table see Sec. 5.1.

The success of a selection as described above, depends on several constraints, which are described briefly in the following: In both channels hard cuts on the background processes are performed. Therefore, it is necessary to have accurate statistical models describing these background processes. For the SM processes in the studied decays, it is important to have an effective algorithm to reconstruct the Z bosons. For this, it is essential to use a powerful algorithm to identify leptons. The "lepton candidate algorithm" used in this thesis is of this kind (see Sec. 4.1). For the set of SUSY processes, it is important to note, that the success of such a selection depends on the MSSM model, which is chosen (here MSSM SPS1a). It is also possible, to perform this selection on MSSM models with similar particle masses and decay channels. On the other hand, the intrinsic behavior of the processes in theses models in respect to the cut variables mentioned in Sec. 5.1 and 5.2 is particularly important. This can be seen from the edge in the spectrum of the di-lepton invariant mass in Fig 5.5 and 5.2. For

masses of about 85 GeV an edge in the distributions for the neutralinos $\tilde{\chi}_i^0\tilde{\chi}_j^0$, ($i = 1, 2$ and $j = 2, 4$) is clearly visibly. If the position of this edge would be higher as a consequence of a different model point, a selection as presented in this thesis would be much more difficult [27].

Chapter 6

Summary and Outlook

In this thesis, a cut-based analysis of the associated production of a light and a heavy neutralino, $e^+e^- \to \tilde{\chi}_1^0\tilde{\chi}_3^0$, at the ILC is presented. The basis of these studies is the Minimal Supersymmetric Standard Model (MSSM) at the benchmark point SPS1a. The properties of the heavy neutralinos $\tilde{\chi}_3^0$, $\tilde{\chi}_4^0$ are determined completely by measurements of the light system $\tilde{\chi}_1^0$, $\tilde{\chi}_2^0$, together with measurements of the charginos. Although the study of the heavy neutralino system provides an important consistency check of the SUSY scenario assuming, if the masses, cross-sections and branching ratios of the light neutralinos sector have already been measured [31].

In this thesis the following polarisations $\mathcal{P}_i := (P(e^+)/P(e^-))$, $(i = 1, 2, 3)$ have been taken into account: $\mathcal{P}_1 = (0.0/0.0)$, $\mathcal{P}_2 = (0.0/0.8)$ and $\mathcal{P}_3 = (-0.6/0.8)$. The analysis has been performed on a set of simulated events, which consists of all relevant contributions from SM and SUSY processes to final states with up to six leptons. The $\tilde{\chi}_1^0$ is the lightest supersymmetric particle (LSP) in the chosen parameter set of this SUSY model and, due to R-parity conservation, it is stable. The $\tilde{\chi}_3^0$ is mainly decaying into a chargino and a W boson or into a neutralino and a Z boson. In this thesis the following two decays have been studied, assuming an integrated luminosity of 500 fb^{-1} and a center-of-mass energy of 500 GeV:: First $\tilde{\chi}_3^0 \to \tilde{\chi}_1^0 Z^0$, where $Z^0 \to e^\pm e^\mp, \mu^\pm\mu^\mp$. And second $\tilde{\chi}_3^0 \to \tilde{\chi}_2^0 Z^0$, where $\tilde{\chi}_2^0 \to \tilde{l}^\pm l^\mp$ and $Z^0 \to e^\pm e^\mp, \mu^\pm\mu^\mp$. For the first channel is not possible to determine a significant contribution of the $\tilde{\chi}_3^0$ for any of the studied polarisations. The calculated statistical significances range from 0.26 to 1.22. In the second channel mentioned above, the determined significances range from 3.56 to 10.44 and the statistical errors on the partial cross-section range from 21% to 42%. For the polarisations $\mathcal{P}_2 = (0.0/0.8)$ and $\mathcal{P}_3 = (-0.6/0.8)$ a $5{\cdot}\sigma$-discovery is possible.

In further studies, a determination of the mass of the $\tilde{\chi}_3^0$ in this channel would be desirable. This could be possible by analysing the kinematical limits of the energy distribution of the final state leptons, but it is more complicated in the second channel compared to the first. The reason for this is relatively long decay chain of the $\tilde{\chi}_3^0$. Moreover, a study of the edges, seen in the distributions of the invariant mass of the final state leptons, as a function of the chosen parameter set is an interesting field. This is important, because an analysis as it is presented in this thesis, is strongly dependent on the position of these edges. More information about this can be found in the study [27].

Appendix A

Detailed Cut-Flow Tables

cuts	signal ($\tilde{\chi}_1^0\tilde{\chi}_3^0 \to$ all)			neutralinos			SUSY background			SM background		
	$\mathcal{P}_1$	$\mathcal{P}_2$	$\mathcal{P}_3$	$\mathcal{P}_1$	$\mathcal{P}_2$	$\mathcal{P}_3$	$\mathcal{P}_1$	$\mathcal{P}_2$	$\mathcal{P}_3$	$\mathcal{P}_1$	$\mathcal{P}_2$	$\mathcal{P}_3$
(0.0)	3612.3	6455.7	10322.1	62711.9	17593.8	13856.9	608443.3	820771.6	$\sim 1.2 \cdot 10^6$	$\sim 10 \cdot 10^9$	$\sim 10 \cdot 10^9$	$\sim 10 \cdot 10^9$
(0.5)	858.0	1533.5	2451.9	51938.3	13821.5	10164.2	326063.5	396049.7	545567.5	3558995.2	3321906.0	3439195.5
(1.1)	723.1	1292.2	2066.1	25666.5	8520.9	7981.6	301884.0	376519.0	528636.1	2401300.5	2216268.0	2255878.8
(1.2)	717.1	1281.6	2049.1	25239.5	8423.9	7927.2	300080.2	374350.1	525962.5	2244166.0	2063911.8	2085666.2
(1.3)	704.9	1259.6	2014.0	23399.4	8049.8	7769.3	298265.0	372854.1	524650.5	1935183.6	1766642.8	1772960.4
(1.4)	130.0	232.3	371.4	4703.2	1626.3	1576.1	181475.4	268837.6	388612.9	696296.2	638225.5	642892.8
(1.5)	21.1	37.7	60.3	2.0	2.3	3.5	11216.6	16900.6	24524.8	17325.2	9726.8	11556.1
(2.1)	15.6	27.9	44.6	1.7	1.9	2.8	7703.7	11514.9	16700.2	5885.3	2057.8	1931.2
(2.2)	13.0	23.2	37.2	0.9	1.3	2.0	596.6	503.1	369.8	1537.4	473.2	405.9
(2.3)	10.8	19.4	31.0	0.4	0.7	1.0	532.8	448.8	338.8	1179.9	362.0	309.2

cuts	signal $\tilde{\chi}_1^0\tilde{\chi}_3^0 \to$ all			neutralinos $\tilde{\chi}_1^0\tilde{\chi}_2^0 \to$ all			$\tilde{\chi}_1^0\tilde{\chi}_4^0 \to$ all			$\tilde{\chi}_2^0\tilde{\chi}_2^0 \to$ all		
	$\mathcal{P}_1$	$\mathcal{P}_2$	$\mathcal{P}_3$	$\mathcal{P}_1$	$\mathcal{P}_2$	$\mathcal{P}_3$	$\mathcal{P}_1$	$\mathcal{P}_2$	$\mathcal{P}_3$	$\mathcal{P}_1$	$\mathcal{P}_2$	$\mathcal{P}_3$
(0.0)	3612.3	6455.7	10322.1	31811.4	10836.1	10374.1	448.6	650.9	1018.0	30451.9	6106.8	2464.9
(0.5)	858.0	1533.5	2451.9	23315.5	7954.2	7624.7	101.6	147.8	231.3	28521.2	5719.4	2308.3
(1.1)	723.1	1292.2	2066.1	23218.9	7923.0	7596.1	85.4	124.1	194.1	2362.2	473.8	191.3
(1.2)	717.1	1281.6	2049.1	23137.3	7896.0	7571.0	84.9	123.4	193.0	2017.4	404.6	163.3
(1.3)	704.9	1259.6	2014.0	23113.1	7888.1	7563.7	83.2	120.9	189.1	203.2	40.8	16.5
(1.4)	130.0	232.3	371.4	4647.5	1587.9	1523.9	21.7	31.6	49.4	34.0	6.8	2.8
(1.5)	21.1	37.7	60.3	0.5	0.2	0.2	1.4	2.1	3.3	0.1	~ 0.0	~ 0.0
(2.1)	15.6	27.9	44.6	0.5	0.2	0.2	1.1	1.7	2.6	0.1	~ 0.0	~ 0.0
(2.2)	13.0	23.2	37.2	~ 0.0	~ 0.0	~ 0.0	0.9	1.3	2.0	~ 0.0	~ 0.0	~ 0.0
(2.3)	10.8	19.4	31.0	~ 0.0	~ 0.0	~ 0.0	0.4	0.7	1.0	~ 0.0	~ 0.0	~ 0.0

Table A.1: *Cut-flow tables for the analysis of $\tilde{\chi}_3^0 \to \tilde{\chi}_1^0 Z^0$, corresponding to the pre-cuts and cuts mentioned in (1.1) to (1.5) and (2.1) to (2.3). The lines (0.0) and (0.5) contain the number of events before pre-selection during the simulation of events and after (see Tab. 4.9). The upper table shows the accumulated numbers for the three categories mentioned in the histograms (see Fig. 5.1, 5.2, and 5.3. For the definition of the categories see Tab. 4.10 and 4.11). The lower table displays the category of neutralinos in a more detailed way. For each category the three polarisations $\mathcal{P}_i := (P(e^+)/P(e^-))$, $(i = 1, 2, 3)$ with $\mathcal{P}_1 = (0.0/0.0)$, $\mathcal{P}_2 = (0.0/0.8)$ and $\mathcal{P}_3 = (-0.6/0.8)$ are listed. A more detailed description of the SUSY and SM background is given in Tab. A.2 and. A.3. All numbers are given for an integrated luminosity of 500 fb^{-1} and a center-of-mass energy of 500 GeV.*

cuts	charginos $\tilde{\chi}_1^+\tilde{\chi}_1^- \to$ all			selectrons $\tilde{e}_1^+\tilde{e}_1^-, \tilde{e}_{1/2}^+\tilde{e}_{2/1}^-, \tilde{e}_2^+\tilde{e}_2^- \to$ all			smuons $\tilde{\mu}_1^+\tilde{\mu}_1^-, \tilde{\mu}_2^+\tilde{\mu}_2^- \to$ all			staus $\tilde{\tau}_1^+\tilde{\tau}_1^-, \tilde{\tau}_{1/2}^+\tilde{\tau}_{2/1}^-, \tilde{\tau}_2^+\tilde{\tau}_2^- \to$ all		
	$\mathcal{P}_1$	$\mathcal{P}_2$	$\mathcal{P}_3$	$\mathcal{P}_1$	$\mathcal{P}_2$	$\mathcal{P}_3$	$\mathcal{P}_1$	$\mathcal{P}_2$	$\mathcal{P}_3$	$\mathcal{P}_1$	$\mathcal{P}_2$	$\mathcal{P}_3$
(0.0)	71585.9	14478.4	6009.0	242892.1	333611.5	442714.6	37819.2	47133.0	72271.7	39999.2	49565.8	75940.5
(0.5)	46321.2	9366.9	3885.3	190909.7	261355.2	346343.6	29617.4	36328.1	55577.5	27548.6	33749.4	51623.4
(1.1)	45954.3	9293.0	3855.0	173452.6	247428.4	337404.3	27421.1	35610.9	54915.4	25431.8	32494.6	49999.0
(1.2)	45798.2	9261.5	3842.1	172225.1	245821.7	335558.8	27257.2	35435.3	54652.2	25290.5	32338.8	49764.3
(1.3)	45702.2	9242.1	3834.0	171022.7	244862.7	335020.9	27119.1	35399.4	54626.8	25109.6	32197.5	49566.0
(1.4)	2774.7	561.0	232.5	147933.0	223752.0	318769.7	24097.9	33546.2	52199.4	1485.2	1886.6	2900.6
(1.5)	25.1	5.0	2.0	9566.8	14619.1	20977.6	1596.4	2241.8	3492.2	28.1	34.4	52.6
(2.1)	18.2	3.7	1.5	6450.2	9779.9	14002.5	1212.1	1703.5	2653.8	23.1	27.6	42.1
(2.2)	0.1	~ 0.0	~ 0.0	537.3	474.9	336.4	59.0	28.2	33.4	0.1	~ 0.0	~ 0.0
(2.3)	0.1	~ 0.0	~ 0.0	476.9	421.7	306.5	55.7	27.1	32.3	0.1	~ 0.0	~ 0.0

cuts	sneutrinos $\tilde{\nu}_e\tilde{\nu}_e$,$\tilde{\nu}_\mu\tilde{\nu}_\mu$,$\tilde{\nu}_\tau\tilde{\nu}_\tau \to$ all		
	$\mathcal{P}_1$	$\mathcal{P}_2$	$\mathcal{P}_3$
(0.0)	216147.0	375983.0	599611.5
(0.5)	31666.6	55250.2	88137.7
(1.1)	29624.2	51692.0	82462.5
(1.2)	29509.3	51492.9	82145.0
(1.3)	29311.4	51152.5	81602.8
(1.4)	5184.6	9091.8	14510.7
(1.5)	0.2	0.3	0.5
(2.1)	0.1	0.1	0.2
(2.2)	~ 0.0	~ 0.0	~ 0.0
(2.3)	~ 0.0	~ 0.0	~ 0.0

Table A.2: *Cut-flow tables for the SUSY backgrounds of* $\tilde{\chi}_3^0 \to \tilde{\chi}_1^0 Z^0$*, corresponding to the pre-cuts and cuts mentioned in (1.1) to (1.5) and (2.1) to (2.3). The lines (0.0) and (0.5) contain the number of events before pre-selection during the simulation of events and after (see Tab. 4.9). For each category the three polarisations* $\mathcal{P}_i := (\mathrm{P}(e^+)/\mathrm{P}(e^-))$*,* $(i = 1, 2, 3)$ *with* $\mathcal{P}_1 = (0.0/0.0)$*,* $\mathcal{P}_2 = (0.0/0.8)$ *and* $\mathcal{P}_3 = (-0.6/0.8)$ *are listed. All numbers are given for an integrated luminosity of 500* fb^{-1} *and a center-of-mass energy of 500 GeV.*

cuts	$\gamma\gamma$ background $\gamma\gamma \to$ ll,qq,WW			γZ,hZ background γZ $\to$ ll,qq and hZ $\to$ all			Zee background Zee $\to$ llee,$\nu\nu$ee,qqee			$\nu\nu$Z background $\nu\nu$Z $\to \nu\nu$ee,$\nu\nu\mu\mu$,$\nu\nu\tau\tau$		
	$\mathcal{P}_1$	$\mathcal{P}_2$	$\mathcal{P}_3$	$\mathcal{P}_1$	$\mathcal{P}_2$	$\mathcal{P}_3$	$\mathcal{P}_1$	$\mathcal{P}_2$	$\mathcal{P}_3$	$\mathcal{P}_1$	$\mathcal{P}_2$	$\mathcal{P}_3$
(0.0)	$\sim 10 \cdot 10^9$	$\sim 10 \cdot 10^9$	$\sim 10 \cdot 10^9$	$\sim 9 \cdot 10^6$	$\sim 9 \cdot 10^6$	$\sim 13 \cdot 10^6$	$\sim 11 \cdot 10^6$	$\sim 11 \cdot 10^6$	$\sim 17 \cdot 10^6$	13341.1	2668.2	1067.3
(0.5)	2875453.8	2875453.8	2875453.8	82316.8	82316.8	121828.9	249389.2	249389.2	369094.8	9922.1	1984.4	793.8
(1.1)	1998197.6	1998197.6	1998197.6	45905.0	45905.0	67939.4	94456.3	94456.3	139795.2	9876.7	1975.3	790.1
(1.2)	1889411.8	1889411.8	1889411.8	41393.7	41393.7	61262.7	58709.5	58709.5	86890.0	9828.7	1965.7	786.3
(1.3)	1640762.8	1640762.8	1640762.8	34279.8	34279.8	50734.1	26126.6	26126.6	38667.3	9827.4	1965.5	786.2
(1.4)	589036.2	589036.2	589036.2	20968.8	20968.8	31033.7	5446.2	5446.2	8060.4	6986.4	1397.3	558.9
(1.5)	1291.7	1291.7	1291.7	3407.3	3407.3	5042.7	909.3	909.3	1345.8	6612.5	1322.5	529.0
(2.1)	131.8	131.8	131.8	220.2	220.2	325.9	13.8	13.8	20.4	3685.5	737.1	294.8
(2.2)	1.0	1.0	1.0	77.3	77.3	114.4	1.0	1.0	1.5	1080.7	216.1	86.5
(2.3)	~ 0.0	~ 0.0	~ 0.0	62.5	62.5	92.5	1.0	1.0	1.5	907.6	181.5	72.6

cuts	Z-pair background ZZ $\to$ llll,ll$\nu\nu$,qqll,qqqq			W-pair background WW $\to$ lνlν,qqlν,qqqq,eeh			Weν background We$\nu \to$ lνeν,qqeν		
	$\mathcal{P}_1$	$\mathcal{P}_2$	$\mathcal{P}_3$	$\mathcal{P}_1$	$\mathcal{P}_2$	$\mathcal{P}_3$	$\mathcal{P}_1$	$\mathcal{P}_2$	$\mathcal{P}_3$
(0.0)	327070.0	217574.8	292445.9	4949072.5	$\sim 1.1 \cdot 10^6$	620828.8	3157950.0	1894770.0	947385.0
(0.5)	16385.0	10899.7	14650.5	256793.2	60621.3	36753.0	68735.3	41241.2	20620.6
(1.1)	10297.1	6849.9	9207.0	211098.9	50002.9	30508.6	31468.8	18881.3	9440.6
(1.2)	10009.8	6658.8	8950.2	207027.6	49101.5	30030.1	27784.8	16670.9	8335.4
(1.3)	8568.9	5700.2	7661.8	197703.6	47059.2	28973.9	17914.4	10748.6	5374.3
(1.4)	5955.8	3961.9	5325.3	61102.7	13334.9	6838.2	6800.1	4080.0	2040.0
(1.5)	3443.6	2290.8	3079.1	1310.7	295.2	162.8	350.1	210.1	105.0
(2.1)	1186.1	789.0	1060.5	611.2	143.9	86.7	36.7	22.0	11.0
(2.2)	196.3	130.6	175.6	167.5	39.0	23.0	13.7	8.2	4.1
(2.3)	149.6	99.5	133.7	47.3	10.4	5.4	12.0	7.2	3.6

Table A.3: *Cut-flow tables for the SM backgrounds of $\tilde{\chi}_3^0 \to \tilde{\chi}_1^0 Z^0$, corresponding to the pre-cuts and cuts mentioned in (1.1) to (1.5) and (2.1) to (2.3). The lines (0.0) and (0.5) contain the number of events before pre-selection during the simulation of events and after (see Tab. 4.9). For each category the three polarisations $\mathcal{P}_i := (P(e^+)/P(e^-))$, $(i = 1, 2, 3)$ with $\mathcal{P}_1 = (0.0/0.0)$, $\mathcal{P}_2 = (0.0/0.8)$ and $\mathcal{P}_3 = (-0.6/0.8)$ are listed. All numbers are given for an integrated luminosity of 500 fb^{-1} and a center-of-mass energy of 500 GeV.*

cuts	signal ($\tilde{\chi}_1^0\tilde{\chi}_3^0 \to$ all)			neutralinos			SUSY background			SM background		
	$\mathcal{P}_1$	$\mathcal{P}_2$	$\mathcal{P}_3$	$\mathcal{P}_1$	$\mathcal{P}_2$	$\mathcal{P}_3$	$\mathcal{P}_1$	$\mathcal{P}_2$	$\mathcal{P}_3$	$\mathcal{P}_1$	$\mathcal{P}_2$	$\mathcal{P}_3$
(0.0)	3612.3	6455.7	10322.1	62711.9	17593.8	13856.9	608443.3	820771.6	$\sim 1.2 \cdot 10^6$	$\sim 10 \cdot 10^9$	$\sim 10 \cdot 10^9$	$\sim 10 \cdot 10^9$
(0.5)	858.0	1533.5	2451.9	51938.3	13821.5	10164.2	326063.5	396049.7	545567.5	3558995.2	3321906.0	3439195.5
(1.1)	64.2	114.9	183.7	17405.8	3499.8	1425.0	14974.5	11922.0	9722.5	207809.7	196067.1	203912.0
(1.2)	61.3	109.6	175.3	17287.6	3475.5	1414.4	14806.6	11815.1	9637.0	145713.1	137693.5	142643.3
(1.3)	53.4	95.5	152.8	17256.0	3468.3	1410.5	14640.0	11740.2	9562.8	70294.0	69497.2	72594.8
(1.4)	40.8	73.1	116.8	8048.3	1618.2	658.8	12681.5	10449.5	7913.6	4376.1	3857.6	5467.6
(1.5)	25.8	46.1	73.7	117.3	24.2	10.8	957.3	733.2	425.8	1827.5	1491.5	2116.3
(2.1)	24.5	43.9	70.2	111.6	23.1	10.3	909.6	695.5	404.2	889.2	697.6	980.2
(2.2)	23.2	41.6	66.5	4.4	1.4	1.2	244.0	116.0	79.0	109.0	90.0	127.7
(2.3)	21.0	37.6	60.1	1.8	0.7	0.8	206.0	97.5	66.6	77.4	64.6	91.7
(2.4)	20.6	36.9	59.0	1.8	0.7	0.8	204.7	97.1	66.5	21.4	17.1	23.8
(2.5)	10.1	18.1	28.9	0.2	0.1	0.1	1.4	0.7	0.5	6.4	5.3	7.0

Table A.4: *Cut-flow table for the analysis of $\tilde{\chi}_3^0 \to \tilde{\chi}_2^0 \mathrm{Z}^0$, corresponding to the pre-cuts and cuts mentioned in (1.1) to (1.5) and (2.1) to (2.5). The lines (0.0) and (0.5) contain the number of events before pre-selection during the simulation of events and after (see Tab. 4.9). The table shows the accumulated numbers for the three categories mentioned in the histograms (see Fig. 5.4 and 5.5 as well as 5.6 and 5.7. For the definition of the categories see Tab. 4.10 and 4.11). For each category the three polarisations $\mathcal{P}_i := (\mathrm{P}(\mathrm{e}^+)/\mathrm{P}(\mathrm{e}^-))$, $(i = 1, 2, 3)$ with $\mathcal{P}_1 = (0.0/0.0)$, $\mathcal{P}_2 = (0.0/0.8)$ and $\mathcal{P}_3 = (-0.6/0.8)$ are listed. A more detailed description of the SUSY backgrounds is given in Tab. A.5 and A.5. The SM background can be found in Tab. A.7 and A.8. All numbers are given for an integrated luminosity of 500 fb^{-1} and a center-of-mass energy of 500 GeV.*

cuts	neutralinos									charginos		
	$\tilde{\chi}_1^0\tilde{\chi}_2^0 \to$ all			$\tilde{\chi}_1^0\tilde{\chi}_4^0 \to$ all			$\tilde{\chi}_2^0\tilde{\chi}_2^0 \to$ all			$\tilde{\chi}_1^+\tilde{\chi}_1^- \to$ all		
	$\mathcal{P}_1$	$\mathcal{P}_2$	$\mathcal{P}_3$	$\mathcal{P}_1$	$\mathcal{P}_2$	$\mathcal{P}_3$	$\mathcal{P}_1$	$\mathcal{P}_2$	$\mathcal{P}_3$	$\mathcal{P}_1$	$\mathcal{P}_2$	$\mathcal{P}_3$
(0.0)	31811.4	10836.1	10374.1	448.6	650.9	1018.0	30451.9	6106.8	2464.9	71585.9	14478.4	6009.0
(0.5)	23315.5	7954.2	7624.7	101.6	147.8	231.3	28521.2	5719.4	2308.3	46321.2	9366.9	3885.3
(1.1)	0.8	0.2	0.1	8.0	11.7	18.2	17397.0	3488.0	1406.7	48.0	9.6	3.9
(1.2)	0.8	0.2	0.1	7.6	10.9	17.1	17279.2	3464.4	1397.2	33.8	6.8	2.7
(1.3)	0.7	0.1	0.1	6.9	10.0	15.7	17248.4	3458.2	1394.7	2.9	0.6	0.2
(1.4)	~ 0.0	~ 0.0	~ 0.0	3.7	5.4	8.4	8044.6	1612.8	650.3	0.1	~ 0.0	~ 0.0
(1.5)	~ 0.0	~ 0.0	~ 0.0	0.6	0.8	1.3	116.7	23.4	9.4	~ 0.0	~ 0.0	~ 0.0
(2.1)	~ 0.0	~ 0.0	~ 0.0	0.6	0.8	1.3	111.1	22.3	9.0	~ 0.0	~ 0.0	~ 0.0
(2.2)	~ 0.0	~ 0.0	~ 0.0	0.4	0.6	0.9	4.0	0.8	0.3	~ 0.0	~ 0.0	~ 0.0
(2.3)	~ 0.0	~ 0.0	~ 0.0	0.3	0.5	0.7	1.4	0.3	0.1	~ 0.0	~ 0.0	~ 0.0
(2.4)	~ 0.0	~ 0.0	~ 0.0	0.3	0.5	0.7	1.4	0.3	0.1	~ 0.0	~ 0.0	~ 0.0
(2.5)	~ 0.0	~ 0.0	~ 0.0	0.1	0.1	0.1	0.2	~ 0.0	~ 0.0	~ 0.0	~ 0.0	~ 0.0

Table A.5: *Cut-flow table for the SUSY backgrounds of the analysis of $\tilde{\chi}_3^0 \to \tilde{\chi}_2^0 \mathrm{Z}^0$, corresponding to the pre-cuts and cuts mentioned in (1.1) to (1.5) and (2.1) to (2.5). The lines (0.0) and (0.5) contain the number of events before pre-selection during the simulation of events and after (see Tab. 4.9). The table shows the accumulated numbers for the three categories mentioned in the histograms (see Fig. 5.4 and 5.5 as well as 5.6 and 5.7. For the definition of the categories see Tab. 4.10 and 4.11). For each category the three polarisations $\mathcal{P}_i := (\mathrm{P}(\mathrm{e}^+)/\mathrm{P}(\mathrm{e}^-))$, $(i = 1, 2, 3)$ with $\mathcal{P}_1 = (0.0/0.0)$, $\mathcal{P}_2 = (0.0/0.8)$ and $\mathcal{P}_3 = (-0.6/0.8)$ are listed. All numbers are given for an integrated luminosity of 500 fb^{-1} and a center-of-mass energy of 500 GeV.*

cuts	selectrons $\tilde{e}_1^+\tilde{e}_1^-, \tilde{e}_{1/2}^+\tilde{e}_{2/1}^-, \tilde{e}_2^+\tilde{e}_2^- \to$ all			smuons $\tilde{\mu}_1^+\tilde{\mu}_1^-, \tilde{\mu}_2^+\tilde{\mu}_2^- \to$ all			staus $\tilde{\tau}_1^+\tilde{\tau}_1^-, \tilde{\tau}_{1/2}^+\tilde{\tau}_{2/1}^-, \tilde{\tau}_2^+\tilde{\tau}_2^- \to$ all			sneutrinos $\tilde{\nu}_e\tilde{\nu}_e, \tilde{\nu}_\mu\tilde{\nu}_\mu, \tilde{\nu}_\tau\tilde{\nu}_\tau \to$ all		
	$\mathcal{P}_1$	$\mathcal{P}_2$	$\mathcal{P}_3$	$\mathcal{P}_1$	$\mathcal{P}_2$	$\mathcal{P}_3$	$\mathcal{P}_1$	$\mathcal{P}_2$	$\mathcal{P}_3$	$\mathcal{P}_1$	$\mathcal{P}_2$	$\mathcal{P}_3$
(0.0)	242892.1	333611.5	442714.6	37819.2	47133.0	72271.7	39999.2	49565.8	75940.5	216147.0	375983.0	599611.5
(0.5)	190909.7	261355.2	346343.6	29617.4	36328.1	55577.5	27548.6	33749.4	51623.4	31666.6	55250.2	88137.7
(1.1)	11025.4	8535.9	4863.2	1355.2	355.4	256.0	1195.6	660.0	832.2	1350.4	2361.0	3767.2
(1.2)	10918.2	8462.8	4820.2	1335.1	349.7	251.5	1179.6	653.1	824.4	1339.9	2342.9	3738.2
(1.3)	10837.3	8428.2	4793.7	1311.4	343.5	247.0	1157.9	641.0	809.1	1330.7	2326.9	3712.8
(1.4)	10168.0	8162.0	4589.2	1084.0	284.1	204.4	417.2	227.4	285.2	1012.2	1776.0	2834.7
(1.5)	859.6	698.3	391.1	88.1	23.1	16.6	4.2	2.4	3.1	5.4	9.4	15.0
(2.1)	817.3	662.4	371.1	83.1	21.8	15.7	4.0	2.3	2.9	5.2	9.1	14.6
(2.2)	193.4	102.7	69.4	50.2	13.2	9.6	0.4	0.1	~ 0.0	~ 0.0	~ 0.0	~ 0.0
(2.3)	161.8	85.9	58.4	43.8	11.5	8.2	0.4	0.1	~ 0.0	~ 0.0	~ 0.0	~ 0.0
(2.4)	160.7	85.6	58.2	43.6	11.4	8.2	0.4	0.1	~ 0.0	~ 0.0	~ 0.0	~ 0.0
(2.5)	1.0	0.6	0.5	0.3	0.1	0.1	0.1	~ 0.0	~ 0.0	~ 0.0	~ 0.0	~ 0.0

Table A.6: *Cut-flow table for the SUSY backgrounds of the analysis of* $\tilde{\chi}_3^0 \to \tilde{\chi}_2^0 Z^0$*, corresponding to the pre-cuts and cuts mentioned in (1.1) to (1.5) and (2.1) to (2.5). The lines (0.0) and (0.5) contain the number of events before pre-selection during the simulation of events and after (see Tab. 4.9). The table shows the accumulated numbers for the three categories mentioned in the histograms (see Fig. 5.4 and 5.5 as well as 5.6 and 5.7. For the definition of the categories see Tab. 4.10 and 4.11). For each category the three polarisations* $\mathcal{P}_i := (P(e^+)/P(e^-))$*,* $(i = 1, 2, 3)$ *with* $\mathcal{P}_1 = (0.0/0.0)$*,* $\mathcal{P}_2 = (0.0/0.8)$ *and* $\mathcal{P}_3 = (-0.6/0.8)$ *are listed. All numbers are given for an integrated luminosity of 500* fb^{-1} *and a center-of-mass energy of 500 GeV.*

cuts	$\gamma\gamma$ background $\gamma\gamma \to$ ll,qq,WW			γZ,hZ background γZ $\to$ ll,qq and hZ $\to$ all			Zee background Zee $\to$ llee,$\nu\nu$ee,qqee			$\nu\nu$Z background $\nu\nu$Z $\to \nu\nu$ee,$\nu\nu\mu\mu$,$\nu\nu\tau\tau$		
	$\mathcal{P}_1$	$\mathcal{P}_2$	$\mathcal{P}_3$	$\mathcal{P}_1$	$\mathcal{P}_2$	$\mathcal{P}_3$	$\mathcal{P}_1$	$\mathcal{P}_2$	$\mathcal{P}_3$	$\mathcal{P}_1$	$\mathcal{P}_2$	$\mathcal{P}_3$
(0.0)	$\sim 10 \cdot 10^9$	$\sim 10 \cdot 10^9$	$\sim 10 \cdot 10^9$	$\sim 9 \cdot 10^6$	$\sim 9 \cdot 10^6$	$\sim 13 \cdot 10^6$	$\sim 11 \cdot 10^6$	$\sim 11 \cdot 10^6$	$\sim 17 \cdot 10^6$	13341.1	2668.2	1067.3
(0.5)	2875453.8	2875453.8	2875453.8	82316.8	82316.8	121828.9	249389.2	249389.2	369094.8	9922.1	1984.4	793.8
(1.1)	165471.9	165471.9	165471.9	7124.4	7124.4	10544.2	14444.3	14444.3	21377.6	0.2	~ 0.0	~ 0.0
(1.2)	117849.7	117849.7	117849.7	4359.1	4359.1	6451.4	8861.5	8861.5	13115.1	0.2	~ 0.0	~ 0.0
(1.3)	62349.4	62349.4	62349.4	1461.6	1461.6	2163.2	3573.5	3573.5	5288.8	0.2	~ 0.0	~ 0.0
(1.4)	210.8	210.8	210.8	152.6	152.6	225.8	1699.7	1699.7	2515.5	~ 0.0	~ 0.0	~ 0.0
(1.5)	1.0	1.0	1.0	105.4	105.4	156.0	660.2	660.2	977.1	~ 0.0	~ 0.0	~ 0.0
(2.1)	1.0	1.0	1.0	98.8	98.8	146.3	164.8	164.8	243.9	~ 0.0	~ 0.0	~ 0.0
(2.2)	1.0	1.0	1.0	4.8	4.8	7.0	29.6	29.6	43.8	~ 0.0	~ 0.0	~ 0.0
(2.3)	1.0	1.0	1.0	4.6	4.6	6.8	17.8	17.8	26.3	~ 0.0	~ 0.0	~ 0.0
(2.4)	1.0	1.0	1.0	3.4	3.4	5.0	2.0	2.0	2.9	~ 0.0	~ 0.0	~ 0.0
(2.5)	1.0	1.0	1.0	1.1	1.1	1.7	~ 0.0	~ 0.0	~ 0.0	~ 0.0	~ 0.0	~ 0.0

Table A.7: *Cut-flow table for the SM backgrounds of the analysis of* $\tilde{\chi}_3^0 \to \tilde{\chi}_2^0 \mathrm{Z}^0$*, corresponding to the pre-cuts and cuts mentioned in (1.1) to (1.5) and (2.1) to (2.5). The lines (0.0) and (0.5) contain the number of events before pre-selection during the simulation of events and after (see Tab. 4.9). The table shows the accumulated numbers for the three categories mentioned in the histograms (see Fig. 5.4 and 5.5 as well as 5.6 and 5.7. For the definition of the categories see Tab. 4.10 and 4.11). For each category the three polarisations* $\mathcal{P}_i := (\mathrm{P}(\mathrm{e}^+)/\mathrm{P}(\mathrm{e}^-))$*, (*$i = 1, 2, 3$*) with* $\mathcal{P}_1 = (0.0/0.0)$*,* $\mathcal{P}_2 = (0.0/0.8)$ *and* $\mathcal{P}_3 = (-0.6/0.8)$ *are listed. All numbers are given for an integrated luminosity of 500* fb^{-1} *and a center-of-mass energy of 500 GeV.*

cuts	Z-pair background ZZ → llll,ll$\nu\nu$,qqll,qqqq			W-pair background WW → lνlν,qqlν,qqqq,eeh			Weν background Weν → lνeν,qqeν		
	$\mathcal{P}_1$	$\mathcal{P}_2$	$\mathcal{P}_3$	$\mathcal{P}_1$	$\mathcal{P}_2$	$\mathcal{P}_3$	$\mathcal{P}_1$	$\mathcal{P}_2$	$\mathcal{P}_3$
(0.0)	327070.0	217574.8	292445.9	4888597.5	$\sim 1 \cdot 10^6$	446660.8	3157950.0	1894770.0	947385.0
(0.5)	16385.0	10899.7	14650.5	252467.2	52834.3	24293.9	68735.3	41241.2	20620.6
(1.1)	2723.9	1812.0	2435.6	10079.1	2051.8	869.2	7646.6	4587.9	2294.0
(1.2)	2573.0	1711.6	2300.6	6759.4	1378.1	586.6	5020.8	3012.5	1506.2
(1.3)	2260.6	1503.8	2021.3	164.5	32.9	13.2	246.3	147.8	73.9
(1.4)	2081.2	1384.5	1860.9	3.8	0.8	0.3	1.0	0.6	0.3
(1.5)	1044.0	694.5	933.5	~ 0.0	~ 0.0	~ 0.0	~ 0.0	~ 0.0	~ 0.0
(2.1)	609.2	405.2	544.7	~ 0.0	~ 0.0	~ 0.0	~ 0.0	~ 0.0	~ 0.0
(2.2)	68.6	45.6	61.3	~ 0.0	~ 0.0	~ 0.0	~ 0.0	~ 0.0	~ 0.0
(2.3)	49.4	32.9	44.2	~ 0.0	~ 0.0	~ 0.0	~ 0.0	~ 0.0	~ 0.0
(2.4)	14.4	9.6	12.9	~ 0.0	~ 0.0	~ 0.0	~ 0.0	~ 0.0	~ 0.0
(2.5)	4.1	2.7	3.7	~ 0.0	~ 0.0	~ 0.0	~ 0.0	~ 0.0	~ 0.0

Table A.8: *Cut-flow table for the SM backgrounds of the analysis of* $\tilde{\chi}_3^0 \to \tilde{\chi}_2^0 \mathrm{Z}^0$*, corresponding to the pre-cuts and cuts mentioned in (1.1) to (1.5) and (2.1) to (2.5). The lines (0.0) and (0.5) contain the number of events before pre-selection during the simulation of events and after (see Tab. 4.9). The table shows the accumulated numbers for the three categories mentioned in the histograms (see Fig. 5.4 and 5.5 as well as 5.6 and 5.7. For the definition of the categories see Tab. 4.10 and 4.11). For each category the three polarisations* $\mathcal{P}_i := (\mathrm{P}(\mathrm{e}^+)/\mathrm{P}(\mathrm{e}^-))$*,* $(i = 1, 2, 3)$ *with* $\mathcal{P}_1 = (0.0/0.0)$*,* $\mathcal{P}_2 = (0.0/0.8)$ *and* $\mathcal{P}_3 = (-0.6/0.8)$ *are listed. All numbers are given for an integrated luminosity of 500* fb^{-1} *and a center-of-mass energy of 500 GeV.*

Bibliography

[1] Gargamelle Neutrino Collaboration, F. J. Hasert *et al.*, *Observation of neutrino like interactions without muon or electron in the Gargamelle neutrino experiment*, Nucl. Phys. **B73**(1974) 1.

[2] M. E. Peskin and D. V. Schroeder, *An Introduction to Quantum Field Theory*, Westview Press (1995).

[3] P. Schmüser, *Feynman-Graphen und Eichtheorien fur Experimentalphysiker*, Springer, Hamburg (1995).

[4] J. F. Gunion, H. Haber, G. Kane, and S. Dawson, *The Higgs Hunter's Guide*, Addison-Wesley (1990).

[5] M. Drees, *An introduction to supersymmetry* (1996), `hep-ph/9611409`.

[6] D. I. Kazakov, *Beyond the standard model (in search of supersymmetry)* (2000), `hep-ph/0012288`.

[7] S. P. Martin, *A supersymmetry primer* (1997), `hep-ph/9709356`.

[8] Einführung Supersymmetrie, lecture notes, Katharina Müller, 2002, available from `http://www.physik.unizh.ch/~kmueller/`.

[9] J. Wess and B. Zumino, *Supergauge transformations in four-dimensions*, Nucl. Phys. **B70**(1974) 39.

[10] S. B. Giddings, *Gravity and strings* (2005), `hep-ph/0501080`.

[11] Particle Data Group Collaboration, S. Eidelman *et al.*, *Review of particle physics*, Phys. Lett. **B592**(2004) 1.

[12] H. Fritzsch, M. Gell-Mann, and H. Leutwyler, *Advantages of the color octet gluon picture*, Phys. Lett. **B47**(1973) 365.

[13] M. Gell-Mann, *A Schematic model of baryons and mesons*, Phys. Lett. **8**(1964) 214.

[14] G. Zweig, *An SU(3) Model for Strong Interaction Symmetry and its Breaking I* (1964), CERN-8182-TH-401.

[15] P. W. Higgs, *Broken symmetries, massless particles and gauge fields*, Phys. Lett. **12**(1964) 132.

P. W. Higgs, *Broken symmetries and the masses of gauge bosons*, Phys. Rev. Lett. **13**(1964) 508.

F. Englert and R. Brout, *Broken symmetry and the mass of gauge vector mesons*, Phys. Rev. Lett. **13**(1964) 321.

G. S. Guralnik, C. R. Hagen, and T. W. B. Kibble, *Global conservation laws and massless particles*, Phys. Rev. Lett. **13**(1964) 585.

[16] S. Hannestad, *Neutrino mass bounds from cosmology* (2004), `hep-ph/0412181`.

[17] M. F. Sohnius, *Introducing supersymmetry*, Phys. Rept. **128**(1985) 39.

[18] G. Moortgat-Pick, S. Hesselbach, F. Franke, and H. Fraas, *Distinguishing between MSSM and NMSSM by combined LHC and ILC analyses* (2005), `hep-ph/0502036`.

[19] S. Y. Choi, D. J. Miller, and P. M. Zerwas, *The neutralino sector of the next-to-minimal supersymmetric standard model* (2004), `hep-ph/0407209`.

[20] F. Zwirner, *Beyond the Standard Model* (1998), European School of High-Energy Physics, Menstrup, Denmark, 25 May - 7 Jun 1997: proceedings CERN. Geneva.

[21] CDF Collaboration, D. Bortoletto, *Searching for SUSY at the Tevatron* (2004), `hep-ex/0412013`.

[22] D0 Collaboration, A. Meyer, *Searches for supersymmetry at the Tevatron* (2004), `hep-ex/0411072`.

[23] B. C. Allanach *et al.*, *The Snowmass points and slopes: Benchmarks for SUSY searches*, Eur. Phys. J. **C25**(2002) 113, `hep-ph/0202233`.

[24] SPA home page, see "SPA draft report" `http://www-flc.desy.de/spa/`.

[25] G. Belanger, S. Kraml, and A. Pukhov, *Comparison of SUSY spectrum calculations and impact on the relic density constraints from WMAP* (2005), `hep-ph/0502079`.

[26] H. E. Haber and G. L. Kane, *The search for supersymmetry: Probing physics beyond the standard model*, Phys. Rept. **117**(1985) 75.

[27] PhD thesis of B. Sobloher (in preparation), for more information see `http://www-flc.desy.de/flc/`.

[28] N. Ghodbane and H.-U. Martyn, *Compilation of SUSY particle spectra from Snowmass 2001 benchmark models* (2002), `hep-ph/0201233`.

[29] SPheno, more information available from `http://www-theorie.physik.unizh.ch/~porod/SPheno.html`.

[30] W. Porod, *SPheno, a program for calculating supersymmetric spectra, SUSY particle decays and SUSY particle production at e+ e- colliders*, Comput. Phys. Commun. **153**(2003) 275, `hep-ph/0301101`.

[31] S. Y. Choi, J. Kalinowski, G. Moortgat-Pick, and P. M. Zerwas, *Analysis of the neutralino system in supersymmetric theories*, Eur. Phys. J. **C22**(2001) 563, `hep-ph/0108117`.

[32] B. C. Allanach *et al.*, *SUSY parameter analysis at TeV and Planck scales*, Nucl. Phys. Proc. Suppl. **135**(2004) 107, `hep-ph/0407067`.

[33] P. M. Zerwas *et al.*, *Reconstruction of fundamental SUSY parameters* (2002), hep-ph/0211076.

[34] B. C. Allanach *et al.*, *Reconstructing supersymmetric theories by coherent LHC / LC analyses* (2004), hep-ph/0403133.

[35] CDF Collaboration, F. Abe *et al.*, *Observation of top quark production in anti-p p collisions*, Phys. Rev. Lett. **74**(1995) 2626, hep-ex/9503002.

[36] D0 Collaboration, S. Abachi *et al.*, *Observation of the top quark*, Phys. Rev. Lett. **74**(1995) 2632, hep-ex/9503003.

[37] Fermilab home page, http://www.fnal.gov/.

[38] LHC home page at CERN, http://lhc-new-homepage.web.cern.ch/lhc-new-homepage/.

[39] Data base of experiments at CERN, home page http://greybook.cern.ch/.

[40] SLAC home page, http://www.slac.stanford.edu/.

[41] TESLA Technical Design Report, available from http://tesla.desy.de/new_pages/TDR_CD/start.html.

[42] ICFA, International Committee for Future Accelerators, home page http://www.fnal.gov/directorate/icfa/.

[43] The Megatables for a future ILC, available from http://www.slac.stanford.edu/xorg/ilc-trc/2002/2002/report/03rep.htm.

[44] The CALICE Project, CAlorimeter for the LInear Collider with Electrons, home page http://polywww.in2p3.fr/flc/calice.html.

[45] PYTHIA, more information available from http://www.thep.lu.se/∼torbjorn/Pythia.html.

[46] T. Sjostrand, L. Lonnblad, S. Mrenna, and P. Skands, *PYTHIA 6.3: Physics and manual* (2003), hep-ph/0308153.

[47] BRAHMS, A CVS based Simulation and Reconstruction code for the TESLA Detector, more information available from http://www-zeuthen.desy.de/lc_repository/detector_simulation/dev/BRAHMS/.

[48] GEANT - Detector Description and Simulation Tool, more information available from http://wwwasd.web.cern.ch/wwwasd/geant/.

[49] SIMDET - A Fast Simulation Tool for Linear Collider Detector Studies, more information available from http://www-zeuthen.desy.de/lc_repository/detector_simulation/dev/SIMDET/.

[50] M. Pohl and H. J. Schreiber, *SIMDET - Version 4: A parametric Monte Carlo for a TESLA detector* (2002), hep-ex/0206009.

[51] P. Skands *et al.*, *SUSY Les Houches accord: Interfacing SUSY spectrum calculators, decay packages, and event generators*, JHEP **07**(2004) 036, hep-ph/0311123.

[52] FeynHiggs, available from
`http://www.feynhiggs.de/`.

[53] M. Pohl and H. J. Schreiber, *SIMDET - Version 3: A parametric Monte Carlo for a TESLA detector* DESY-99-030.

[54] UA1 Collaboration, G. Arnison *et al.*, Phys. Lett. **B123**(1983) 115.

[55] J. Huth *et al.*, *Research Directions for the Decade*, Snowmass (1990) 134, ed. E.L. Berger (World Scientific, Singapore).

[56] CDF Collaboration, F. Abe *et al.*, *A Limit on the top quark mass from proton - anti-proton collisions at s**(1/2) = 1.8-TeV*, Phys. Rev. **D45**(1992) 3921.

[57] OPAL Collaboration, R. Akers *et al.*, *QCD studies using a cone based jet finding algorithm for e+ e- collisions at LEP*, Z. Phys. **C63**(1994) 197.

[58] Talk given by B. Sobloher at LCWS 2004, Paris, April 2004, more information available from
`http://polywww.in2p3.fr/actualites/congres/lcws2004/`.

[59] T. Ohl, *CIRCE version 1.0: Beam spectra for simulating linear collider physics*, Comput. Phys. Commun. **101**(1997) 269, `hep-ph/9607454`.

[60] H. Anlauf, *A Monte Carlo algorithm for multiphoton beamstrahlung in Monte Carlo event generators* (1996), `hep-ph/9602397`.

[61] The ntuple project, more information available from
`http://www-flc.desy.de/flc/science/analysis_ntuple/index.html`.

[62] ROOT - An Object-Oriented Data Analysis Framework, more information available from `http://root.cern.ch/`.

Danksagung

An dieser Stelle möhte ich denen Menschen danken, die mich während dieser Arbeit direkt und indirekt unterstützt haben.

Mein besonderer Dank gilt Prof. Dr. Rolf-Dieter Heuer, für die Möglichkeit, in seiner Forschungsgruppe zu arbeiten und Prof. Dr. Klaus Desch für die interessante Aufgabenstellung und gute Betreuung. Prof. Dr Peter Schleper möchte ich für die Übernahme des Zweitgutachtens danken.

Außerdem danke ich allen Mitgliedern der Gruppe FLC für hilfreichen Diskussionen. Mein besonderer Dank gilt darüberhinaus Dr. Thorsten Kuhl, Dr. Alexei Raspereza, Blanka Sobloher, Tania Robens, Dr. Steve Aplin und Jörgen Samson, sowie meinen netten Bürokollegen Tatsiana Klimkovich und Dr. Philip Bechtle.

Ein ganz besonderer Dank gilt auch meiner Familie, die mich immer unterstützt hat, und natürlich meiner Freundin, die jahrelang meine wenige Zeit und, oftmals zusätzlich, meine schlechte Laune zu ertragen hatte.

Hiermit versichere ich, diese Arbeit selbständig unter Verwendung der angegebenen Quellen und Hilfsmittel angefertigt zu haben.

Hamburg, den 28. Februar 2005

– Oliver Wendt –